



university of
 groningen

faculty of mathematics
 and natural sciences

kapteyn astronomical
 institute

Master Thesis

**Simulating the Systematic Variation of the Low-Mass
 Stellar Initial Mass Function in Early-Type Galaxies
 Using a Semi-Analytic Model**

Judith ter Horst

Groningen, August 24, 2015

Supervisors: Prof. dr. S.C. Trager
 Gergö Popping

Second Reader: Prof. Dr. M. C. Spaans

Abstract

Simulating the Systematic Variation of the Low-Mass Stellar Initial Mass Function in Early-Type Galaxies Using a Semi-Analytic Model

Recent studies combining spectroscopy, lensing or dynamics with stellar population models indicate the low-mass stellar initial mass function (IMF) varies with high velocity dispersion in early-type galaxies (ETG) in the local Universe. The physical origin for this bottom-heavy IMF is still unclear, although turbulence in star-forming clouds appears to drive fragmentation to smaller mass scales.

We used the statistical capability of semi-analytic models (SAM) to qualitatively investigate the low-mass IMF slope as a function of typical galaxy properties to probe what underlying processes could drive the IMF variation. We test four different models that re-assign an IMF to stars formed under specific conditions in the SAM and compare the resulting present day mass function slope with the observed IMF slope: The first two models tie the slope of the low-mass IMF to the star formation mode, either quiescently (bottom-light IMF) or burst (bottom-heavy IMF), or to the present-day location of the stars, either in the disc (bottom-light IMF) or in the bulge (bottom-heavy IMF). This indicates that most of the stars in today's most massive ETGs did not form in turbulent star burst but turbulent gas in discs at high redshift following a bottom-heavy IMF and moved to the bulge afterwards. We therefore test two models where the power-law slope of the low-mass IMF varies with the cosmic epoch and velocity dispersion of the galaxy at the moment the stars formed following the observed IMF slope relation with velocity dispersion. We find that by assigning an IMF slope relation to stars formed in a galaxy with a certain velocity dispersion that is slightly higher and steeper than the relation observed in the Local Universe, we are able to reproduce the observed low-mass IMF variation with galaxy velocity dispersion.

Contents

Abstract	i
1 Introduction	1
1.1 The Stellar Initial Mass Function	1
1.1.1 The IMF in the Milky Way and Local Group	1
1.1.2 Observations of a Varying IMF in massive ETGs	3
1.1.3 Theories of a varying CMF and IMF	4
1.1.3.1 Core Formation from MHD Shocks in a Turbulent Magnetised Medium	5
1.1.3.2 Core Formation from the Press-Schechter Formalism for a Tur- bulent Medium	5
1.1.3.3 Core Formation from the EPS Formalism for a Turbulent Medium	6
1.2 Semi-Analytic Modeling of Galaxy Formation and Evolution	9
1.2.1 The Λ CDM Model of Galaxy Formation	9
1.2.1.1 Modeling the Λ CDM Framework	9
1.2.2 Dark Matter Merger Trees	10
1.2.2.1 The (Extended) Press-Schechter Formalism	10
1.2.2.2 (EPS-Based) DM Merger Trees and SAMs	10
1.2.3 The Baryonic Model	12
1.2.3.1 DM Haloes, Merger Trees and Substructures	12
1.2.3.2 Cooling	14
1.2.3.3 Disc Formation	14
1.2.3.4 Quiescent and Burst-Mode Starformation	14
1.2.3.5 Chemical Enrichment and Supernova Feedback	15
1.2.3.6 Spheroid Formation	15
1.2.3.6.1 Disk Instabilities and Spheroid Formation	15
1.2.3.6.2 Modeling of Spheroidal Structural Parameters	16
1.2.3.7 Black Hole Growth and Feedback	16
1.2.4 Comparison of SAM Results with Observations	17
1.3 This Project	17
2 General Method: Creating and fitting the IMF bins	19
2.1 Introduction	19
2.2 Creating the IMF bins	20
2.2.1 The Initial Mass Function	20

2.2.1.1	Salpeter IMF	21
2.2.1.2	Chabrier IMF	21
2.2.2	Normalisation Constants	21
2.2.2.1	Normalising the Salpeter IMF	22
2.2.2.2	Normalising the Chabrier IMF	22
2.2.3	Mass Bins	23
2.2.4	Integrating the Mass Function	23
2.2.5	Populating the PDMF	24
2.2.6	Re-assignment of IMF	24
2.2.7	Comparing the model PDMF with the theoretical mass function	25
2.3	Fitting the PDMF	26
2.4	Summary of the PDMF and fitting algorithm	27
3	Models I and II: Star Formation Mode and Morphology Linked to IMF	29
3.1	Introduction	29
3.2	PST14: Method & Results	30
3.2.1	Specifications	30
3.2.2	SF-IMF Model	30
3.2.2.1	Selection Criteria Galaxies	30
3.2.2.2	Results	31
3.2.3	Morph-IMF Model	39
3.2.3.1	Results	39
3.3	Porter+14: Method & Results	41
3.3.1	Specifications	41
3.3.2	SF-IMF Model & Morph-IMF Model for 4 Merger Trees	41
3.3.2.1	Updated Selection Criteria Galaxies: Observed ETGs	44
3.3.3	SF-IMF Model & Morph-IMF Model for 21 Merger Trees	46
3.3.3.1	SF-IMF Model & Morph-IMF Model for Power-Law Slope $x = 1.85$	50
3.3.3.2	Selecting Spheroid-Dominated Early Type Galaxies	53
3.4	Conclusion and Discussion	58
4	Model III: σ linked to IMF in post-processing and in SAM	60
4.1	σ - $\langle t \rangle$ -IMF Model	60
4.1.1	Method	60
4.1.2	Results	63
4.2	σ -IMF Model in SAM	66
4.2.1	Method	67
4.2.2	Results	69
4.2.2.1	Spiniello Relation as Input σ - x Relation	69
4.2.2.2	Spiniello + 0.15 Relation as Input σ - x Relation	74
4.2.2.3	The σ - x Relation at $z = 1$ and $z = 0$	75
4.3	Conclusion and Discussion	79
5	Conclusion	83
5.0.1	Future Prospects	85

Les gens ont des étoiles qui ne sont pas les mêmes. Pour les uns, qui voyagent, les étoiles sont des guides. Pour d'autres elles ne sont rien que de petites lumières. Pour d'autres qui sont savants elles sont des problèmes. [...] Mais toutes ces étoiles-là elles se taisent.

-Antoine de Saint-Exupéry, *Le Petit Prince*

Introduction

1.1 The Stellar Initial Mass Function

The stellar initial mass function (IMF) describes the mass distribution of stars formed in a single star-formation event. In other words, it describes the ratio of high to low-mass stars formed in a single stellar population. The IMF is important in our understanding of observational properties and evolution of stars itself as stellar evolution and the resulting observable properties such as color and luminosity are mostly determined by stellar mass. Moreover, the ratio of low and high-mass stars is important in understanding observational properties and evolution of large populations of stars such as galaxies as high-mass stars are responsible for most of the chemical enrichment and stellar feedback and will dominate the light of a galaxy whereas the low-mass stars dominate the galaxy's total stellar mass. The IMF is used in converting observed properties of distant galaxies such as colour and luminosity into stellar masses for galaxies too far away to resolve individual stars by relating the IMF of resolved nearby stars to the integrated light of distant unresolved stellar populations. Stellar population synthesis models (SSP) are used as tools in interpreting the integrated light we receive from these galaxies. These models backtrack the possible star formation histories (SFH) and metallicity history that could give the observed properties of a galaxies such as colors, line-indices and luminosities by using stellar evolution prescriptions and stellar spectra libraries given an, assumed, input IMF. It is thus important to have a good understanding of the IMF and its behavior with cosmic time and environment. The IMF is an observationally derived relation and its theoretical underpinning and physical driving factors still remain an open question although advances in observations of the IMF in varying environments and theoretical and computational derivations of the origin of the IMF have been made over the last several years which will be relayed below.

1.1.1 The IMF in the Milky Way and Local Group

The IMF is an observationally derived relation, or rather a parametrization of the number of stars formed per unit mass as derived as derived from observations. However, we do not observe the IMF directly. We convert the individual or integrated luminosity of objects into a mass function using theories or relations of stellar luminosity, mass and ages. In most cases we

also not observe the IMF but the present day mass function (PDMF). Massive stars above a certain “turn-off” mass will have moved off the main sequence after a certain age such that the observed present-day light and the derived masses will differ from the one initially created. The observations of this PDMF is converted into an IMF by accounting for the loss of high mass stars using theories of star formation rates and histories which assume that the IMF is invariant over time. Only in young stars clusters where none of the stars have yet moved off the MS or had considerable mass loss are we able to observe the luminosity function corresponding to the IMF directly.

Most observational studies of the IMF have been performed on stellar populations in the Milky Way. In our galaxy, stars with masses $1 M_{\odot}$ are found to follow a power-law distribution with power-law coefficient $\alpha = 2.35$ from fits to observational data as first described by Salpeter (1955). For stars below $1 M_{\odot}$ this function breaks or turns over and goes to 0 in the sub-stellar regime, i.e. below $0.08 M_{\odot}$ (Offner et al. 2014). The Galactic IMF over the entire mass range is described in several ways, either as a series of three broken power-law (Kroupa and Gilmore 1993), (Kroupa 2002) or as a log-normal distribution in the low-mass end with a power-law tail above $1 M_{\odot}$ (Chabrier 2003). The break or turn over point varies in these methods but lies between 0.08 and $1 M_{\odot}$. The difference in representation can be seen as a difference in ideas on whether stars formation is a continuous process across all mass ranges (Chabrier) or whether different physical processes drive SF in each regime (Kroupa) (Offner et al. 2014). The high-mass end of IMF appears to hold in star-forming regions in the Local Universe (Bastian and Meyer 2010; Offner et al. 2014).

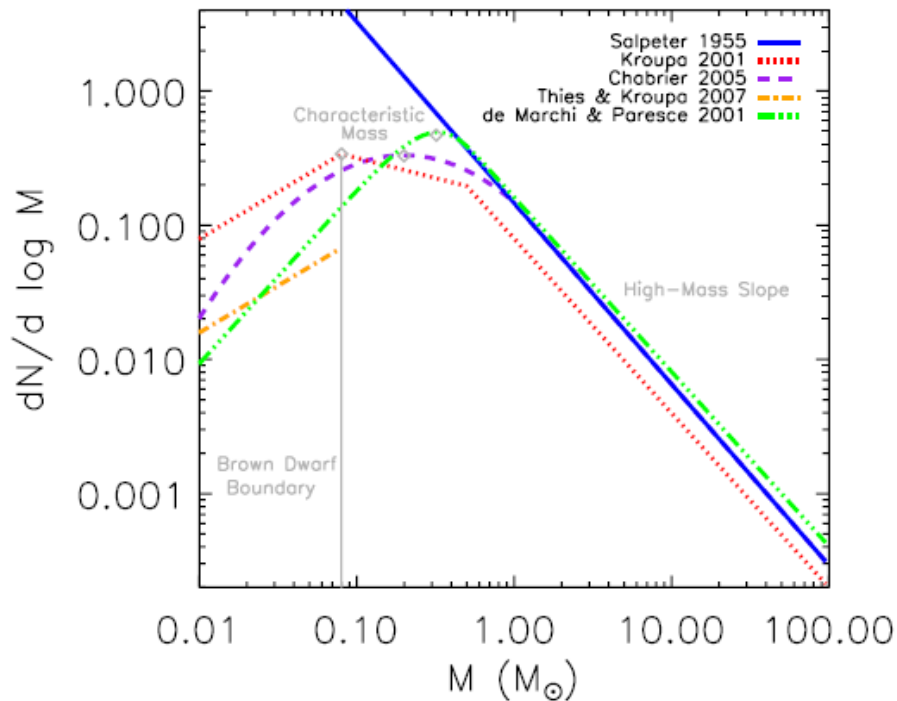


FIGURE 1.1: The functional forms for (among others) the Salpeter (solid blue), Kroupa (dotted red) and Chabrier (dashed purple) IMF; three functional forms that have been proposed to fit Galactic observations of stellar mass distribution. Each of these curves is normalised such that the integral over the mass is unity. Figure from Offner et al. (2014).

1.1.2 Observations of a Varying IMF in massive ETGs

It is impossible to directly observe the low-mass IMF in extragalactic environments so the Galactic IMF has been assumed to be invariant over the Universe. However, several recent extragalactic IMF studies have found that the low-mass IMF of early type galaxies (ETGs) steepens, so becomes more dwarf-rich with increasing galaxy velocity dispersion (Auger et al. 2010; Conroy and van Dokkum 2012a,b; Ferreras et al. 2013; LaBarbera et al. 2013; Spiniello et al. 2014, 2012; Treu et al. 2010; van Dokkum and Conroy 2010). These studies determine the low-mass IMF of the unresolved stellar populations of ETGs with the following different techniques or combinations thereof:

- Using surface gravity sensitive spectral line strengths indicative of low mass ($\leq 0.3 M_{\odot}$) stars and comparing the observed spectra with synthetic ones from SSP models to find the best IMF fit. van Dokkum and Conroy (2010) observed two of these lines which are thought to be strong in low-mass stars, the NAI doublet and Wing-Ford molecular band, and later NAD Conroy and van Dokkum (2012a,b), in ETGs in the Coma and Virgo cluster. They fit of synthetic indices for these lines from the SSP models to the observed lines gives a best fit for a logarithmic IMF slope of $x \approx -3$ which is much steeper than the Salpeter coefficient of 2.35. Other studies found that the NAI and NAD lines can in some cases be influenced interstellar absorption (Spiniello et al. 2012). However, Spiniello et al. (2014, 2012) find a similar relation based on TiO2 line strengths which are sensitive to cool dwarf stars and less contaminated by age or metallicity. They compare this line index in stacked Sloan Digital Sky Survey (SDSS) of ETGs with velocity dispersion varying from $150\text{--}310 \text{ km s}^{-1}$ to stellar population models and find they the IMF slope x steepens for increasing σ , over the center of these bins from $1.85 - 2.62$ following :

$$x = 2.3(\pm 0.1) \log(\sigma_{200}) + 2.13(\pm 0.15) \quad (1.1)$$

Ferreras et al. (2013) and LaBarbera et al. (2013) have found similar, though slightly steeper x - σ relations using the same spectral line.

- Using dynamical analysis of stellar kinematics and comparing the derived M/L -ratios with those from SSP models. Cappellari et al. (2012) used stellar kinematics for 260 ETGs from the ATLAS3D project. They constructed several different dynamical models, with an axisymmetric stellar component and a dark halo whose shape is a free parameter, and fit these models to th the projected stellar distribution and the 2D stellar kinematics to get $(M/L)_{star}$. The dynamically derived M/L only constrains the overall mass normalisation of the IMF. These are compared to $(M/L)_{pop}$ derived by fitting SSP synthetic spectra for different input IMFs to the observed spectra. The dynamically derived M/L is found to vary with increasing M/L_{star} , where the lowest M/L_{star} ratios are described by a Kroupa or Chabrier normalisation and going to a Salpeter or an even more bottom heavy IMF normalisation for the galaxies with the largest M/L ratios.
- Using gravitational lensing and stellar kinematics to distinguish the dark and luminous mass of lensed ETGs and comparing these with stellar mass estimates from SSP models using the multicolour photometric data of these galaxies. Treu et al. (2010) determine the total mass within the Einstein radius of lensed ETGs form the Sloan Lens ACS Survey (SLACS) by fitting gravitational lens models. They then model the stellar mass within the Einstein radius based on SDSS velocity dispersion data by using this total mass within the Einstein radius from lensing and by assuming a fixed profile for the dark matter halo and the anisotropy of the stellar component. This is then compared to the stellar mass inside

the Einstein radius independently derived from SSP models. This SSP model determines the stellar mass based on the multicolour Hubble Space Telescope (HST) photometric data of these lensed galaxies, assuming either a Salpeter or a Chabrier IMF. They find that SSP stellar masses based on a Salpeter IMF agree with those from lensing and dynamical models whereas the SSP masses based on a Chabrier IMF underestimates them. They also find an increasing power-law slope with increasing velocity dispersions. This observed trend could also be due to a non-universal dark matter halo profile, a degeneracy which cannot be resolved within this model based on a combination lensing and dynamical data. However, as the above described studies based on spectral lines and solely dynamical data also find a similar trend of IMF slope with velocity dispersion, it is most likely the IMF which is non-universal.

All three methods thus find a steepening of the low-mass IMF slope with increasing galaxy mass or velocity dispersion, by comparing observationally derived stellar masses, either through stellar dynamics, spectroscopy or lensing, with those derived from SPP models using stellar spectral libraries and stellar evolutionary theories. Spiniello et al. (2012) compare all three different methods described and find that they provide similar trends going from a Salpeter IMF slope of $x = 2.35$ at $\sigma \approx 200 \text{ km s}^{-1}$ to an upper limit of $x = 3.0$ for the most massive ETGs with $\sigma \approx 335 \text{ km s}^{-1}$. Smith (2014) compares the IMF of ETGs derived from dynamics and spectroscopic data and also finds that both methods on average give a steeper IMF slope than observed in the Milky way though he does not find any correlation between slope on a galaxy-by-galaxy basis between these two methods.

These recent observations of ETGs thus provide strong indications for a non-universal IMF, with the low-mass IMF varying with galaxy velocity dispersion in elliptical galaxies. This would have implications on galaxy evolutionary models and observational results using stellar mass and metallicity derivations based on the IMF as observed in the Milky Way and the Local Group.

1.1.3 Theories of a varying CMF and IMF

Despite the implications of a non-universal IMF for many areas in astronomy, we do not yet have a conclusive theory of the origin of the IMF. However, several theoretical and computational models have been put forward in which molecular cloud fragmentation into gravitationally bound, pre-stellar, cores is driven by turbulence and resulting density fluctuations in these clouds (Hennebelle and Chabrier 2008, 2009; Hopkins 2012a,b, 2013; Padoan and Jones 1997; Padoan and Nordlund 2002). These theories of variation in the fragmentation of molecular clouds on low-mass scales induced by increasing turbulence provide a promising way to connect the observed IMF variations in ETGs to variations in galactic environments in which stars form.

These theories of star formation and stellar mass distribution rely on a relation between IMF and the the mass function of pre-stellar cores (CMF), which describes the distribution of clumps of gas that will go on collapse and form one to a few stars. These functions are observed to be similar (McKee and Ostriker 2007), although the CMF appears to be shifted to larger masses (e.g. Alves et al. (2007)). Following this similarity, theories of star formation thus relate stellar masses to core masses as these clumps in molecular clouds are thought to serve as gas reservoirs of material for the forming stars. The local conditions in molecular clouds that determine the fragmentation of gas into cores leading to a CMF will as a consequence also

determine the IMF. The main factor contributing to this fragmentation in all of these theories is turbulence, which can both provide support against gravity in the ISM and at the same time it will create compressions and rarifications leading to local density fluctuations which if dense enough can collapse to form stars (Offner et al. 2014).

1.1.3.1 Core Formation from MHD Shocks in a Turbulent Magnetised Medium

Padoan and Jones (1997); Padoan and Nordlund (2002) were among the first to propose a theory based on a combination of turbulence and gravity. Magneto-hydrodynamic (MHD) shocks due to supersonic isothermal turbulence in a magnetised medium forms both under dense regions and sheets and filaments in molecular clouds which can turn into cores. When locally gravity exceeds the thermal and magnetic energy as given by the thermal Jeans mass, these overdensities or cores can collapse to form protostars. The effects of interacting shocks in the turbulent flow are multiplicative which following the central limit theorem naturally leads to a log-normal density distribution. Most dense cores will be able to collapse, but following this log-normal density distribution even some small cores have a chance to be dense enough to undergo collapse.

The derivation of the mass distribution of dense cores relies upon the assumption that the power-law shaped power spectrum of the velocity field of the pre-shocked gas and the post-shock velocity field are self-similar. Moreover, the typical mass of cores scales with the thickness of the post-shock gas out of which they formed, so that the number of cores per scale L scales as L^{-3} . These elements connect the Alfvénic Mach number to the scale L of the initial turbulent fluctuation and thus to the number of cores formed for a certain scale length of the shocked gas. When combined with the distribution of Jeans masses, the mass distribution of collapsing cores is then given by a power-law close to a Salpeter slope for masses above $1 M_{\odot}$ because of the, assumed, power-spectrum for turbulence and flattens and turns over decreasing with mass for sub-solar masses as observed. The number of cores below $1 M_{\odot}$ able to collapse increases with increasing Mach number of the pre-shock gas as a larger Mach number increases density contrasts following the MHD shock conditions.

1.1.3.2 Core Formation from the Press-Schechter Formalism for a Turbulent Medium

Hennebelle and Chabrier (2008, 2009) have pointed out that some of the assumptions made in this theory are not justified; for instance the magnetic field is not observed to be proportional to density in simulations or observations (Hennebelle et al. 2008; Padoan and Nordlund 1999; Troland and Heiles 1986). Also, turbulence does not always promote star formation in every over dense region as is assumed but is also found to quench overall star formation efficiency (Hennebelle and Chabrier 2008).

Hennebelle and Chabrier (2008, 2009) propose an analytic theory of the CMF and IMF based on the cosmological Press-Schechter (PS) theorem which describes the mass distribution of dark matter haloes in cosmology forming from overdensities in a Gaussian field of initial density fluctuations (Press and Schechter 1974). In the PS theory densities that lie above a certain mass threshold at a particular epoch and will undergo gravitational collapse to evolve into a bound object, a dark matter halo. Rather than the cosmological Gaussian density distribution, Hennebelle and Chabrier (2008) use a log-normal density distribution for density fluctuations in molecular clouds due to supersonic isothermal turbulence. They determine the mass spectrum of bound self-gravitating objects in a solely quiescent or turbulent medium and a combination of

both on all scales. The density threshold above which overdensities can be considered to collapse and form a gravitationally bound prestellar core is scale-dependent for supersonic turbulence, in contrast to the scale-free density threshold in the cosmological case. This threshold can be calculated from the Virial theorem by determining when thermal, turbulent and magnetic support are dominated by gravity.

The resulting mass distribution is described by a power-law at large scales and a log-normal form which is centered around the characteristic mass for gravitational collapse and rapidly declines for lower masses following an exponential cut off. The mass distribution is dependent on the global Mach number M , the ratio of the non-thermal velocity over the sound speed at the scale of the whole cloud and on the effective Mach number M_* , the same quantity at the scale of the mean Jeans length, which describes the ratio of turbulent versus thermal support at the Jeans length scale. Increasing the global Mach number enhances the collapse of small scale structures as it heightens and decreases the peak of the turnover mass. This increases the amount of brown dwarfs formed but does not affect the high-mass power law tail significantly. An increase in effective Mach number at fixed global Mach number, so increasing the influence of turbulent support at the Jeans length scale, does significantly affect the location of the turn over mass but it decreases the peak slightly. Fewer intermediate-mass stars are formed as the extra turbulent support suppresses the gravitational collapse of large structures into smaller ones. At the high-mass end increasing the global turbulence extends the maximum core or stellar mass. Increasing turbulence in this model thus increases the formation of low-mass and high mass stars but also suppresses the formation of intermediate mass stars.

When comparing this model to observations, the Salpeter power-law tail is recovered at the high-mass end for the velocity power spectrum of isothermal supersonic turbulence as given by numerical simulations (Kritsuk et al. 2007) whereas pure thermal collapse produces a power-law tail steeper than Salpeter. In the low-mass end, however, the number of brown dwarfs are underestimated by the turbulent model when comparing with observations, although this effect lessens with increasing global Mach number.

1.1.3.3 Core Formation from the EPS Formalism for a Turbulent Medium

Hopkins (2012a,b, 2013) extended this approach of deriving the IMF via the PS formalism to larger, galactic, scales that dominate velocity and density fluctuations and find that they derive the resulting properties with fewer assumptions. Moreover, he invoked a method that solves the cloud-in-cloud problem of PS theory more naturally than in the Hennebelle and Chabrier (2008, 2009) models. This problem is the miscounting of the number of low-mass structures in the PS formalism, as it does not take into account that small structures can end up in larger ones at later times. Bond et al. (1991) first identified this problem and proposed the excursion set theorem, which executes a random walk for a density fluctuation and determines when it first crosses the largest scale for which it is considered to be bound, the first-crossing scale. By determining how often the fluctuation crosses this threshold, this theorem can count the mass enclosed within a halo at the scale. The probability of smaller substructures within a region are taken into account via this method.

Hopkins (2012a) uses the PS theory extended by the excursion set theorem, extended Press-Schechter (EPS), but derives the results for the log-normal density distribution of supersonic turbulent gas with an assumed power-law spectrum instead of for a Gaussian cosmological density spectrum. The EPS formalism is derived for turbulent gas in a galactic disc over scales from that of the entire disc to below the sonic length.

The method goes as follows: the density field is smoothed at some scale and the mean density in a window with increasing radius will be compared to a threshold above which the self-gravitating collapse of the density fluctuations is possible. This threshold is determined taking into account thermal, turbulent, magnetic and rotational support, all of which contribute differently on different size scales. Therefore there is both a maximum and a minimum scale for which the smoothed field crosses this threshold and for which structure is self-gravitating, the first-crossing and the last-crossing distribution respectively. In between these extremes the field can cross the threshold multiple times. As the dynamic range of the scales taken into account is large, this crossing allows for formation of self-gravitating substructures within large structures over all these scales.

The density variance as a function of scale, and its dependence upon Mach number, naturally follows from the EPS theorem as the effect of turbulence on disc scales to the smallest scales is taken into account. This is in contrast to the Hennebelle and Chabrier (2008, 2009) model, where this relation was an assumption based on numerical simulations. The relation between Mach number and density variance determines the broadness of the mass distribution in both models. The collapse conditions derived from this method on smaller scales are found to be the same as in the Hennebelle and Chabrier (2008, 2009) model.

The first-crossing distribution for turbulent gas in a disc is found to reproduce observations of the mass function of giant molecular clouds (Hopkins 2013). The last-crossing distribution is found to correspond to the CMF and by extension to the IMF. At the high-mass end where the scale radius is in the turbulent regime, this reproduces a near Salpeter power-law slope whose value is set by the critical density from the local Jeans criterion. This power-law turns over at the sonic radius, where the contributions from thermal and turbulent support are equal. The turnover mass is dependent on the sonic radius which can be related to the global disc gas surface density. When the scale radius is below the sonic radius, thermal support increases and the low-mass slope flattens with increasing Mach number. The model in Hopkins (2013) does not predict a varying high mass slope for variations in star forming core temperatures, galaxy velocity dispersion and galaxy surface density typical of the Milky Way and the Local Group. The low-mass CMF turn-over occurs at lower mass for higher global Mach number, creating some variation in the low-mass slope but still within the observed differences in the low-mass slope. However, for more extreme global parameters, i.e. a higher temperature, gas surface density and Mach number, as observed in ultra-luminous infra-red galaxies and starburst regions such as merging galaxy nuclei, the turnover between high and low mass slopes occurs more slowly and at a lower mass than in the Milky Way. This creates a bottom-heavy IMF in these environments, as the mass boundary where thermal support dominates over turbulent support decreases with increasing Mach number. The high mass slope in these extreme cases is similar to Milky Way like conditions. However, as the turnover mass decreases in the case of extreme global parameters, there are more intermediate mass stars formed and more importantly the low-mass slope becomes bottom-heavy.

These three models to derive the CMF and by extension the IMF from turbulence in molecular clouds thus all predict a Salpeter-like powerlaw slope at high core masses and a log-normal turnover as can be seen in Figure 1.2. The location of this turnover depends on the scale below which thermal and/or magnetic support becomes greater than that of turbulence. A larger Mach number thus allows for fragmentation to smaller scales. However, these theories of the CMF/IMF formation and variation in itself do not yet provide an explanation of the difference in conditions in galaxies that appears to lead to a more bottom-heavy IMF in ETGs than in our own Milky Way. Merger-induced star formation and starburstst could provide such turbulent conditions out of which a bottom-heavy IMF can form as these lead to high

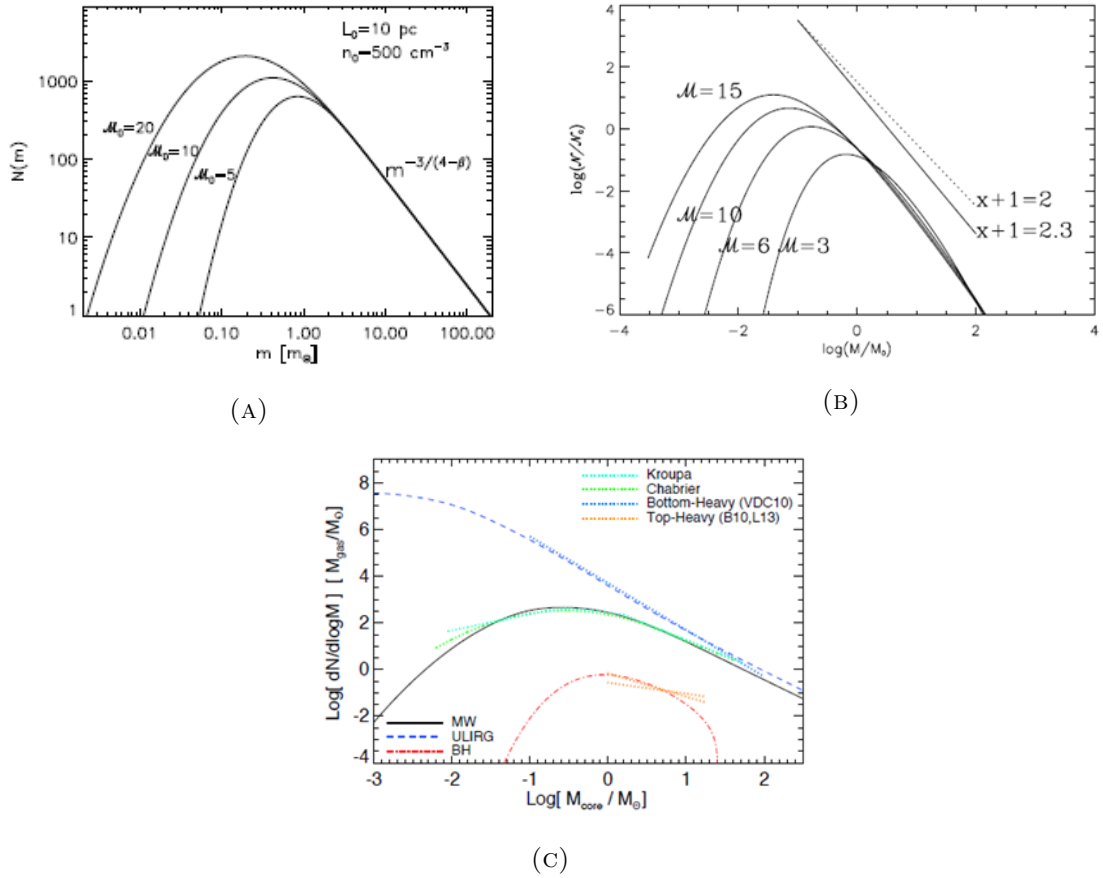


FIGURE 1.2: The mass distribution of bound, prestellar, cores for varying values of Mach number of the flow from Padoan and Nordlund (2002) (left), Mach number at the scale of the whole cloud from Hennebelle and Chabrier (2008) (right) and Mach number at the disc scale Hopkins (2013) (bottom), as for the latter the Mach number on disc scales in ULIRGs is higher than in the MW. All three theories for turbulence induced fragmentation in molecular clouds predict a Salpeter-like powerlaw slope at high core masses and a log-normal turnover. The location and height of this turnover depends on the scale below which thermal and/or magnetic support becomes greater than that of turbulence where a larger Mach number allows for fragmentation to smaller scales and relatively more mass in low-mass stars.

local temperatures, densities and velocity dispersion. There are indications that massive ETGs formed more of their stars in star burst and at higher redshift, when the ISM was more dense and the average temperature was higher, than spiral galaxies (Brennan et al. 2015; Cappellari et al. 2012). Such a dependence on star formation history and environment could link the theories on the origin of a bottom-heavy IMF to the observations of the bottom-heavy IMF in ETGs. We will therefore investigate the variation of the low-mass IMF with global galaxy properties, such as fraction of starburst, total stellar mass, and morphology, that could possibly influence the mass distribution of stars using semi-analytic models (SAMs) of galaxy formation and evolution. These models can provide global properties of galaxies for a large number of galaxies in a computer-time efficient manner and are therefore ideal to study variations of the IMF with galaxy and star formation environment.

1.2 Semi-Analytic Modeling of Galaxy Formation and Evolution

One method to model and study the formation and evolution of galaxies is through semi-analytic models (SAMs). SAMs tie physically motivated recipes for the baryonic processes that govern galaxy formation and evolution to dark matter (DM) halo merger trees as formed within the hierarchical Λ CDM model of structure formation.

1.2.1 The Λ CDM Model of Galaxy Formation

The Λ CDM model is the current standard cosmological model of a cold dark matter (CDM) universe with a cosmological constant (Λ). Within this model structure forms through the collapse of small-amplitude primordial density fluctuations in the cold dark matter component of the Universe (Blumenthal et al. 1984). The initial DM fluctuations are assumed to follow a Gaussian random distribution creating a nearly uniform density field in the early Universe. Inflation, the exponential expansion of space-time in the early Universe, enlarged the initial minute quantum fluctuations to over- and under-densities of matter on larger scales. DM only interacts through gravity, and is not affected by opposing pressure, resulting in the growth of the over-densities through gravitational collapse. In the Λ CDM picture, the amplitude of the dark matter fluctuations decreases with increasing scale, such that smaller objects collapse first and then merge with one another to form larger and larger structures in a hierarchical manner. Once these densities become equal to or larger than the mean background density of the Universe they cannot be described by linear clustering theory. They enter the non-linear regime in which these clumps of DM will be affected by both the gravitational pull of neighbouring structures but also start to have an impact on matter flows resulting in a much more complicated (description of their) evolution. The non-linear evolution of these DM density perturbations will eventually lead to a virialised DM halo, a bound, self-gravitating system. Baryonic gas that falls into the potential well of these DM haloes and then cools and fragments to form stars will eventually produce luminous galaxies (White and Rees 1978). In the hierarchical clustering model, galaxies will grow and evolve due to the continuing merging of these dark haloes and the baryonic components within them (Cole et al. 1994). These baryonic components are coupled gravitationally to the DM and can be influenced by shocks, cooling and heating processes. Next to processes like star formation and evolution, galaxy tidal interaction and mergers will thus influence the galaxy properties. (Cole et al. 1994)

1.2.1.1 Modeling the Λ CDM Framework

As the process of hierarchical structure formation has an influence on the formation and evolution of different types of galaxies and thus to both the similarities and differences in their observed properties, it is important to model this process in more detail. This can be done using large N-body simulations of DM structure formation and distribution coupled with hydrodynamics. However, to obtain realistic galaxies in the Λ CDM framework and reproduce observed galaxy properties in detail, additional baryonic physics such as cooling, star formation and supernova (SN) and active galactic nuclei (AGN) feedback which together form a complicated feedback loop needs to be included in these DM N-body simulations (Cole 1991; Kauffman et al. 1993; Somerville and Primack 1999; White and Frenk 1991; White and Rees 1978). Due to time and memory limitations it is not computationally feasible to include realistic gas physics over

the required dynamic range in N-body simulations of a significant volume. Moreover, as we do not understand the full details of the interplay of these baryonic processes and feedback loops, we would like to study the effects of varying the uncertain parameters associated with these processes on the modeled galaxies. As N-body simulations are computationally expensive, it is difficult or impossible to study a wide range of models varying the uncertain parameters or to study different realisations of the same model (Somerville and Primack 1999). Semi-analytic models (SAMs) do provide a computationally efficient and easier way to study bulk galaxy properties for a very large number of galaxies and to reproduce many observed properties (Somerville et al. 2012). SAMs apply simple but physically motivated recipes for the physical processes that shape galaxies to DM merger trees that are formed either via N-body simulations or via the analytic extended Press-Schechter (EPS) theory within the framework of structure formation predicted by Λ CDM.

1.2.2 Dark Matter Merger Trees

1.2.2.1 The (Extended) Press-Schechter Formalism

The Press-Schechter formalism is based upon the idea that we can make predictions on the outcome of nonlinear collapse on the basis of the initial linear DM density fluctuations (Press and Schechter 1974). This means that we can relate non-linear properties such as the mass distribution and merging probabilities to the initial spectrum of linear Gaussian density fluctuations from which they originated and grew (Longair 2008). The PS formalism produces a halo mass distribution at a given redshift based on overdensity which lie above a certain threshold at that particular epoch and thus have undergone gravitational collapse to evolve into a bound object by that epoch. However, this analysis is based on the linear theory of growth of perturbations. It only considers positive density fluctuations collapsing into bound objects, whereas a Gaussian density field contains both over- and underdensities. Once perturbations grow to larger amplitudes, mass is accreted from the vicinity of the perturbations so also from underdensities in the original field (Longair 2008). This miscounts the the number of low-mass DM fluctuations, many of which would have been subsumed into larger objects (Bond et al. 1991). This is the so called “cloud-in cloud” or “peak-in peak” problem. This problem can be solved by letting the value of the overdensity execute a Markovian random walk for different smoothing mass scales or thresholds ensuring that each element is in a halo of some, possibly very low, mass scale. This excursion set formalism or EPS formalism which can relate the fraction of trajectories of the random walk in haloes with a certain mass at one epoch to a halo with a larger mass at a larger mass can thus create a halo merging tree (Bond et al. 1991).

1.2.2.2 (EPS-Based) DM Merger Trees and SAMs

EPS can thus predict the masses of the progenitor haloes and the redshifts at which these smaller haloes merge to form larger haloes, the parent halo (Cole et al. 1994; Kauffman et al. 1993; Somerville and Kolatt 1999; White and Frenk 1991). The redshifts of branching events and the masses of the progenitor haloes at each stage are chosen randomly using Monte Carlo techniques such that the overall distributional satisfies the average predicted by the EPS theory (Somerville and Primack 1999). A particular Monte Carlo trajectory of the halo merging history is referred to as a realisation (Somerville and Primack 1999). SAMs represent structure formation by describing these merging histories of virialised dark mater haloes and coupling the universal baryon fraction gravitationally to the virial mass of the halo (Somerville et al. 2008).

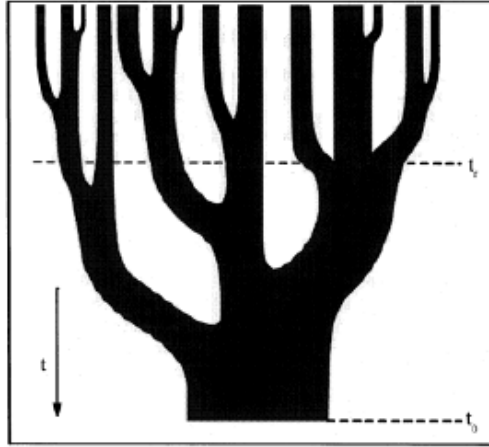


FIGURE 1.3: A schematic depiction of a binary merger tree to provide a visual of the concept. A horizontal slice through the tree gives the distribution of masses in the parent haloes at a given time t (Lacey and Cole 1993). The model by Somerville et al. has set no limit on the amount of branches allowed.

This baryonic component is accreted as hot gas and will cool to form a galaxy. Initially galaxies form in their own halo and are followed in the simulation as their haloes are incorporated into larger haloes, as given by the DM merger tree. During these halo mergers, galaxies from different initial haloes can eventually merge, cause tidal disruptions, or become a satellite galaxy depending on the ratio of masses of galaxies in the different DM haloes. A parent halo of a given mass can have a variety of merging histories and the properties of the galaxies that form within this halo is thought to depend to some extent on that history (Somerville and Kolatt 1999). The Monte Carlo approach of random sampling facilitates the study individual objects or global quantities in the SAM. As the Monte Carlo method allows tracing of individual galaxies, it is possible to look at the scatter in galaxies properties caused by different merging histories (Kauffman et al. 1993). Many realisations of the merger tree can be run in a moderate amount of time on a work station. SAMs are therefore an efficient and feasible way of exploring the effect of varying the uncertainties associated with merger histories and baryonic processes on galaxy properties providing a way to qualitatively understand many features of galaxy formation and evolution (Somerville and Primack 1999).

Somerville et al. construct the merging history of a dark matter halo by sampling the paths of individual particle trajectories using the excursion set formalism (Somerville and Primack 1999). This sampling of the trajectories starts at a halo mass M_0 and goes back in time using very small time steps. For each trajectory in M_0 at z_0 , the mass of the progenitor halo it was located in at an earlier redshift z_1 is chosen randomly using Monte Carlo techniques such that it follows the probability that a halo of mass M_0 at redshift z_0 had a progenitor in the mass range $(M_1, M_1 + dM_1)$. A branch occurs when at least two trajectories are found in haloes with masses greater than a pre-set minimum resolution mass M_l to make the tree finite (Somerville et al. 2008). Only haloes the history of haloes larger than this mass will be followed. In the model by Somerville, contributions from trajectories in haloes smaller than M_l are included as accretion of a diffuse component.

1.2.3 The Baryonic Model

SAMs model the formation history and evolution of galaxies by tying simple but physically motivated recipes for the baryonic physics that shapes galaxies to the DM merger trees. These physical recipes are mostly dependent on feedback between cold gas, warm gas and the stellar component and/or black holes such as simplified hydrodynamics, star formation, supernova (SN) and active galactic nucleus (AGN) feedback, galaxy-galaxy mergers, and stellar population synthesis (Somerville and Kolatt 1999; Somerville and Primack 1999; Somerville et al. 2008). Underlying theory and observations are used to set parameters that model these processes. A schematic depiction of the interplay of all these processes in SAMs in general can be found in figure 1.4, though this description is more extensive than the 'Santa Cruz' version of the SAM used in this project.

The particular SAM used in this project/thesis is based on the ones described in Somerville and Primack (1999); Somerville et al. (2008, 2012), the 'Santa Cruz' SAM. The version was extended in 2014 by Popping et al. (2014) (PTS14) to include multiphase gas partitioning and to compute the star formation rate (SFR) based on the molecular gas content (Popping et al. 2014). Besides the PST14 model another version of the SAM as updated by Porter et al. (2014a) (Porter+14) was used in this project as well. This version of the SAM provides a method to model spheroid growth through both major and minor mergers and disc instabilities which moves stars from the disc to the spheroid. This method also allows the modeling of the effective radius and velocity dispersion of galaxies taking into account both the effect of mergers and dissipation on these parameters. Through this addition to the SAM it will be possible to compare the results of the SAM with the observations of the IMF slope- σ relation in 1.1.2. The Porter+14 SAM version does not include the molecular-based SF module from PST14. Moreover, this Porter+14 version of the SAM is not based upon the analytic EPS merger trees but on merger trees from the Bolshoi N-body DM simulation (Klypin et al. 2011; Trujillo-Gomez et al. 2011) which were generated via the ROCKSTAR method as developed by (Behroozi et al. 2014). However, implementing the model with either EPS and Bolshoi, or other N-body, DM trees gives similar results (Porter et al. 2014a; Somerville et al. 2008).

The description of the physical recipes in the SAM below is mostly based on the description of Somerville et al. (2008) and Somerville et al. (2012) this forms the basis for both of the models used, for a more detailed description please take a look at these papers (Somerville et al. 2008, 2012). The most important changes within the PS14 and Porter+14 that are of influence to our research are discussed as well.

1.2.3.1 DM Haloes, Merger Trees and Substructures

In the SAM, the universal baryon fraction corresponding to the DM halo mass is assumed to be accreted as hot gas (Somerville et al. 2000). Every DM halo in each merger tree is given a dimensionless angular momentum, or spin, parameter and a concentration parameter based on redshift and halo mass. This concentration parameter describes the matter density profile of each halo as given by the Navarro-Frenk-White profile (Somerville et al. 2008). When DM haloes merge the central galaxy of the largest progenitor becomes the new central galaxy and all others become satellites. These can lose angular momentum due to dynamical friction as they orbit and in some cases may eventually merge with the central galaxy (Somerville et al. 2012). During this merger process, satellites are tidally stripped. Satellites with long merger timescales can become tidally striped and destroyed before they fully merge with the central

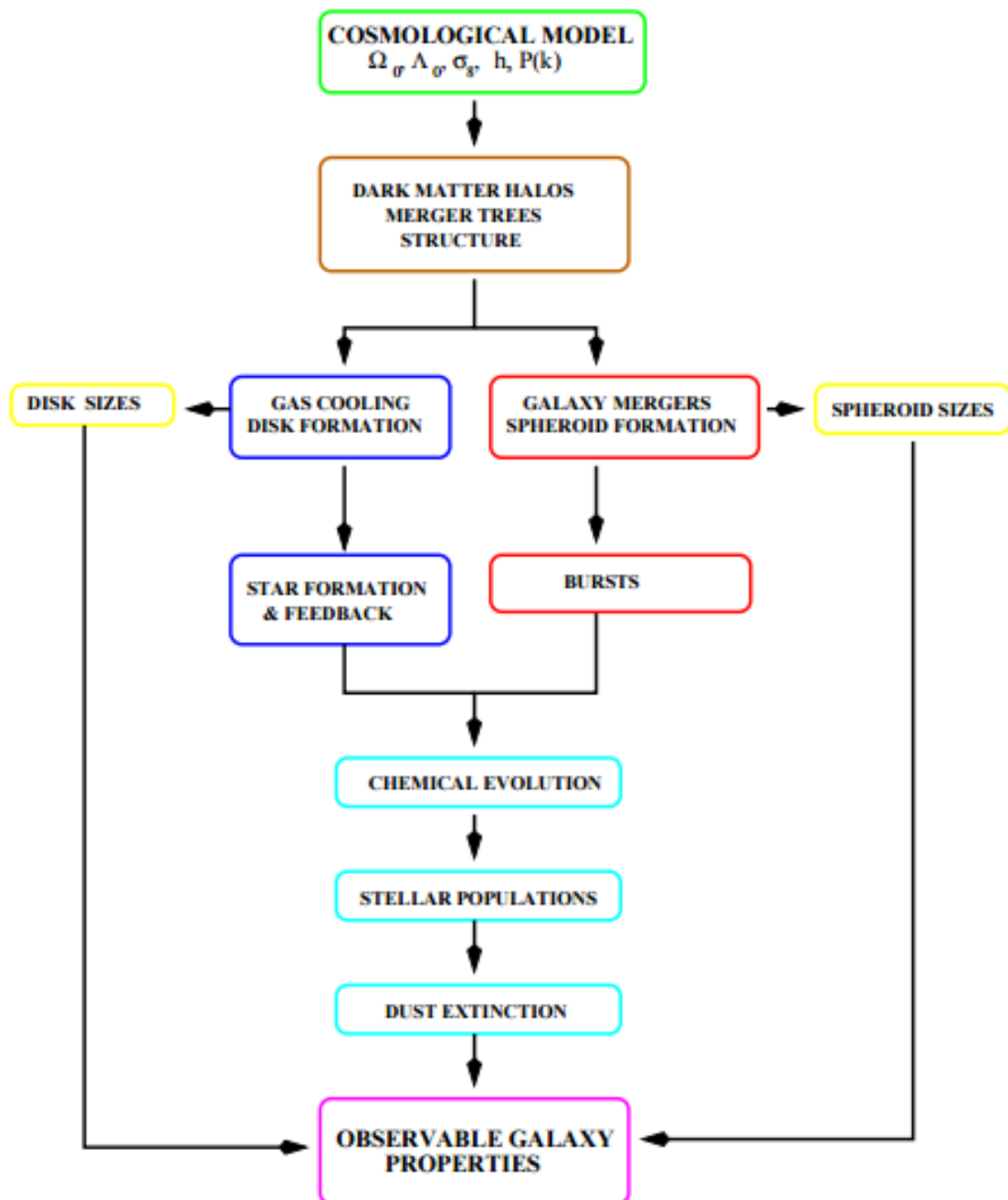


FIGURE 1.4: A schematic description of the interplay between the physical processes in a SAM that will lead to the observable properties of galaxies, as adapted from (Cole et al. 2000) in (Baugh 2006).

galaxy. If this occurs, stars from the satellite are added to a diffuse stellar halo (Somerville et al. 2008). Satellite galaxies are not allowed to merge with other satellites in the model.

1.2.3.2 Cooling

Before reionisation each halo contains a mass of hot gas equal to the universal baryon fraction times the virial mass of the halo. However, after reionisation, the photoionising background suppresses the collapse of gas into low-mass haloes (Gnedin 2000). When a dark matter halo collapses or undergoes a merger that at least doubles the mass of the largest progenitor, the hot gas is shock heated to the virial temperature of the new halo. This gas then cools radiatively and collapses. The cooling radius is the radius in which all of the gas can cool in a cooling time. This cooling time is dependent on the metallicity, density and temperature of the hot gas (Sutherland and Dopita 1993). The cooling time is assumed to be equal to the halo’s dynamical time (Croton et al. 2006; Springel et al. 2001). When the cooling radius is larger than the virial radius the cooling rate is limited by the infall rate, which is determined by the mass accretion history. This regime is associated with “cold flows” in which gas streams into the halo along dense filaments without getting heated. If the cooling radius is smaller than the virial radius, the cooling regime is associated with “hot flows” in which the gas is first shock heated to close to the virial temperature of the halo, forming a quasi-hydrostatic halo, and then cools in a manner similar to a classical cooling flow. This distinction is of importance when modeling heating by AGN-driven radio jets.

1.2.3.3 Disc Formation

The cold gas is assumed to only be accreted by the central galaxy of the halo even though in reality satellite galaxies are thought to accrete some of the cold gas as well. The newly cooling gas is assumed to collapse into a rotationally-supported exponential disc. This gas has acquired angular momentum before it collapses through tidal torques (Peebles 1969). The scale radius of this disc is computed using conservation of angular momentum given the halo’s NFW concentration and spin parameters and the fraction of baryons in the disc following Mo and White (1998). This fraction of baryons is needed as the self-gravity of the collapsing baryons causes the adiabatic contraction of the inner part of the halo. The scale length of the gas can be converted to the scale length of the stars in the disc via a conversion parameter, χ_{gas} , as observations of nearby spiral galaxies suggest that HI discs are more extended than stellar discs (Leroy et al. 2008).

1.2.3.4 Quiescent and Burst-Mode Starformation

Star formation in the model occurs both in a quiescent mode and in a merger-driven star burst mode. In this first mode, the star formation is modeled using the empirical Schmidt-Kennicutt relation, assuming that only cold gas above a fixed critical surface density forms stars (Kennicutt 1998). In the PST14 model, quiescent star formation is modeled based on the surface density of molecular gas. This SF recipe follows a two fold scaling law as in higher H_2 density environments the slope of the SFR density steepens Popping et al. (2014). In the merger driven mode the efficiency and timescales of the bursts are dependent on the merger mass ratio and the gas fraction of the progenitors following hydrodynamical simulations. In Porter+14 burst mode star formation can also be induced via a disc instability as cold gas in the bulge can be used to fuel star formation besides the gas gained through mergers (Porter et al. 2014a).

1.2.3.5 Chemical Enrichment and Supernova Feedback

Within the SAM, stars are formed following a Chabrier IMF (Chabrier 2003). This will have an effect on the amount of feedback from stellar winds and SN of massive stars and on the metallicity enrichment and gas loss due to the stellar evolution. Mass-loss from stars is modeled using the instantaneous recycling approximation which returns a fraction of the mass that was turned into stars to the cold gas reservoir. The metals and mass loss are modeled instantaneously after the formation of stars in the SAM such that the model does not have to keep track of stellar lifetimes and resulting SN and stellar winds and injected metals, which simplifies the computational processes needed in the SAM. The recycled fraction of gas $R = 0.43$ is a good approximation for the mass loss of massive stars in a Chabrier IMF (Bruzual and Charlot 2003).

Chemical enrichment is also modeled by this instantaneous recycling approximation. Every time a set of new stars, dm_* , are formed, a fraction of the mass turned into stars is assumed to instantaneously mix with the cold gas in the disc as mass in metals. This fraction is set by the yield parameter. A newly formed set of stars is assumed to have the same metallicity as the mean metallicity of the cold gas of the ISM at that time step. When gas is removed from the disc through SN driven winds, a corresponding portion of metals is moved to the hot gas or outside the halo. A change in the IMF assigned to a set of stars formed in this project, will not alter any of these IMF-dependent properties in the SAM described here.

A fraction of the energy from SN and stellar winds is deposited into the ISM. This drives large scale outflows of cold gas from the galaxy. The mass outflow rate is linked to the star formation rate and inversely proportional to the escape velocity of the galaxy. A fraction of this ejected gas escapes out of the potential of the DM halo while the rest is deposited in the hot gas reservoir within the halo where it can cool again. This ratio between these two fractions depends on the halo’s circular velocity.

1.2.3.6 Spheroid Formation

Mergers are thought to remove angular momentum from the disc stars and build up a spheroid. The efficiency of this spheroid growth is based on the progenitor’s gas fraction and merger mass ratios. Hydrodynamic simulations indicate that major mergers, so once where the mass ratio is close to equal, and gas-poor mergers are more efficient in removing angular momentum, destroying discs and building a spheroidal component (Hopkins et al. 2009a,b).

1.2.3.6.1 Disk Instabilities and Spheroid Formation

In Porter+14, spheroid formation is also influenced by disc instabilities. N-body simulations have shown that gravitational instabilities that occur when the mass of stars in the disc exceeds a critical value relative to the DM mass, can result in the formation of a bar (Efstathiou et al. 1982; Ostriker and Peebles 1973). Bars can destabilise the disc and transfer mass into a spheroidal component (Debattista et al. 2004). Moreover, cosmological hydrodynamical simulations indicate that “violent disc instabilities” (VDI) lead to fragmentation in gas-rich discs. In this case, clumps of gas that formed through gravitational instabilities can migrate to the center of galaxy, contributing to bulge growth (Bournaud et al. 2011; Dekel et al. 2009, 2013). The version of the SAM used treats both star+gas disc instabilities (DI). The radius of the gas disc and the mass of stars *and* cold gas in the disc are used to determine the onset of instability

following (Efstathiou et al. 1982; Toomre 1964). Each time step the disc is found unstable, stars and gas from the disc are moved to the spheroid component to reach marginal stability. The cold gas moved to the disc is assumed to be used in a starburst. The efficiency and timescale of this burst is the same as in merger triggered starbursts.

1.2.3.6.2 Modeling of Spheroidal Structural Parameters

In the Porter+14 model, the structural parameters of these spheroids formed in mergers can now be computed. The effective radius in gas-rich mergers with dissipation can be determined by augmenting conservation of energy arguments with a term that incorporates radiative losses (Covington et al. 2008, 2011; Porter et al. 2014a). In Porter+14 the constants that account for these radiative losses depend on the mass ratio of the merger and the morphology and gas content of the progenitors (Porter et al. 2014b). The constants are calibrated using results of hydrodynamical simulations of both major and minor mergers of gas-rich disc-dominated progenitors, of mixed-morphology and of spheroid-spheroid mergers (Hopkins et al. 2009c; Johansson et al. 2009). The value is highest for major mergers of two disc-dominated galaxies, lower for minor mergers between two disc-dominated galaxies and mergers where one or both of the galaxies are spheroid dominated are found to be essentially dissipationless (Porter et al. 2014b). The line-of-sight velocity dispersion of the spheroid is computed using the virial theorem where a dimensionless constant accounts for the conversion between the three-dimensional effective radius and the line-of-sight projection of the velocity dispersion. These calculations of the structural parameters are used in the SAM whenever galaxies with a mass ratio greater than 1:10 merge; in mergers below this ratio the satellite material is added to the disc.

1.2.3.7 Black Hole Growth and Feedback

Mergers also drive gas into galactic nuclei, fueling black hole growth. In the SAM each galaxy is born with a small seed black hole of $\approx 10^4 - 10^5 M_\odot$, for PTS14 and Porter+2014 respectively.

After a halo merger, pre-existing black holes in the galaxies will also merge. The black hole (BH) will grow at the Eddington rate until the energy deposited into the interstellar medium (ISM) in the central region of the galaxy becomes enough to reach a pressure driven outflow that stops accretion. This mode of BH growth is called “bright mode” or “quasar mode”, resulting in self-regulated accretion. In Porter+14 BH also grow following a disc instability. In this case it accretes the fuel following a DI event at a fraction of the Eddington limit chosen to reproduce the AGN luminosity function and the BH-bulge mass relation (Hirschmann et al. 2012).

A second mode of black hole growth, the “radio mode”, is associated with powerful jets observed at radio frequencies. The BH is fueled by hot gas accretion according to the Bondi Hoyle approximation instead of the merger-driven BH growth of the “bright mode” (Bondi 1952). This leads to low accretion rates so most of the BH mass is gained in the “bright mode”. However, the radio jets from this “radio mode” are very efficient in coupling with the hot halo gas. This heating term can partially or completely offset cooling in the hot flow mode in the quasi-hydrostatic halo, suppressing star formation through “radio mode feedback”.

1.2.4 Comparison of SAM Results with Observations

Different SAMs have been able to reproduce, at least qualitatively, many fundamental observation such as the morphology-density relation and the Tully-Fisher relation (amongst others (Cole et al. 1994; Kauffman et al. 1993; Somerville and Primack 1999)). Another key result of SAMs is that they can provide a physical explanation of the characteristic shape of the galaxy stellar mass or luminosity function as described by Somerville et al. (2008), after they incorporated AGN feedback into their model (Bower et al. 2006; Croton et al. 2006; Somerville et al. 2008). The Porter+14 showed that the SAM including VDI and dissipation reproduces the observed size-mass relation for ETGs and fundamental-plane scaling relations of spheroid-dominated galaxies in the local universe. It also predicts sufficient intermediate mass ETG in the local universe, which it does not do without including the DI (Porter et al. 2014a).

Though the SAMs are able to reproduce many observational relations such as gas fractions, stellar and gas mass functions in the local universe, SF history, with success, there are still some model result that do not correspond to our current understanding of galaxy evolution. Most notably, there are large discrepancies between the observed number density of low mass galaxies, i.e. with $M_* \approx 10^{9-10.5} M_\odot$, and those predicted by SAMs (Weinmann et al. 2012). Additionally these low mass galaxies are too passive at $z = 0$ (Fontanot et al. 2009; Guo et al. 2010). However, a similar discrepancies are found in hydrodynamical simulations suggesting that this is not necessarily a modeling problem within the SAM but within our modeling of galaxy formation and evolution in general (Weinmann et al. 2012). To solve this problem Weinmann et al. (2012) postulate that the growth of low mass galaxies which grow at late times needs to be decoupled from the growth of the high mass ones at earlier times, which would require a better understanding of processes such as stellar feedback which mostly affect this low mass galaxy end (Weinmann et al. 2012). However, recent work by Henriques et al. (2013) and White and Ferguson (2015) have demonstrated that changing the re-accretion time-scale of ejected gas might be a potential solution to these problems.

1.3 This Project

Recent studies using a combination of lensing, stellar dynamics, spectral features and SSP, indicate that the low-mass IMF varies with galaxy properties such as velocity dispersion. ETGs with high velocity dispersion in the local Universe appear to have relatively more low-mass stars than predicted by a universal IMF. The physical origin for this bottom-heavy IMF is unclear but theories base on increased low-mass fragmentation due to turbulence provide promising results. Merger-induced star formation and starbursts could create local conditions, such as density, temperature, turbulence, for the fragmentation of the star forming cloud that would lead to a bottom-heavy IMF.

We will use the statistical capability of semi-analytical models to qualitatively investigate the low-mass end slope of the IMF as a function of typical galaxy properties such as total stellar mass and fraction of stellar mass formed in bursts. The SAM allows us to track for instance stars formed in turbulent bursts and stars formed in quiescent environments. By re-assign either a bottom-heavy Salpeter or a bottom-light Chabrier IMF to these star formation situations respectively, we can determine the PDMF based on star formation history. The statistical properties and computer-time efficiency of the SAM allow us to study the variation of this PDMF with typical global galaxy properties for a large sample of ETGs. This will give insight into which physical mechanisms in galaxies could be responsible for bottom- heavy star

formation. In Chapter 2 we will explain the general method used for creating bottom-heavy and bottom-light IMF bins and populating these bins with stars formed under different conditions and how we determine the resulting PDMF slope from this. In Chapter 3 and Chapter 4 the results of re-assigning an IMF to stars formed under different conditions and comparison with the observed σ -IMF slope relation will be presented and discussed. In Chapter 5 we will summarise the results of all different models and compare them with theories of IMF variation.

General Method: Creating and fitting the IMF bins

2.1 Introduction

As mentioned in the introduction, the aim of this thesis is to gain insight into the underlying physical reasons of the observed variation in the low-mass end of the IMF. This is done by four different recipes of re-ascribing a bottom-heavy IMF to stars formed under certain conditions in the SAM and to compare the resulting PDMF slope with the observed IMF-slope. In the coming chapters, the following four main models will be considered:

- I The **SF-IMF model**: a physically-motivated model that ties the slope of the low-mass IMF to the type of star formation, either quiescent (bottom-light) or burst (bottom-heavy) in Chapter 3
- II The **Morph-IMF model**: a heuristic model that ties the slope of the low-mass IMF to the present-day location of the stars, either in the disc (bottom-light) or in the spheroid (bottom-heavy), in Chapter 3.
- III The **$\langle t \rangle$ -IMF model**: an observationally motivated model that ties a power-law IMF slope to a set of stars formed that varies with the time at which they formed in post-processing. This power-law slope varies with $\langle t \rangle$ following the σ - $\langle t \rangle$ relation which can be determined from the SAM and the observed σ -IMF slope in ETGs, in Chapter 4.1.
- IV The **σ -IMF model**: an observationally motivated model that ties an IMF slope- σ relation to the stars formed based on the σ of their “host” galaxy at the time of star formation which is implemented within the Porter+14 SAM (although not self-consistently), in Chapter 4.2.

However, the basic method for creating bottom-heavy and bottom-light IMF bins and populating these bins with the stars formed is the same for all three methods; the only real difference is the criteria for the assignment of stars to a particular IMF-slope. Moreover, the manner in which the slope of the resulting bins is fitted, to be compared to the observed IMF

slope, is also the same for each model. Therefore, before the details and results of the three separate models are discussed, first the processes for generating and fitting the PDMF bins is outlined in this chapter.

2.2 Creating the IMF bins

2.2.1 The Initial Mass Function

To understand how IMF bins are created, first the definition and usage of the stellar mass function and initial mass function needs to be explained. The mass function of a stellar population gives the number of stars per unit mass (Salpeter 1955). The mass function $\Phi(M)$ is defined such that $\Phi(M) dM$ is the number of stars with masses between M and $M + dM$. The total number of stars with masses between M_1 and M_2 is then given by

$$N(M_1, M_2) = \int_{M_1}^{M_2} \Phi(M) dM \quad (2.1)$$

or equivalently

$$\Phi = \frac{dN}{dM} \quad (2.2)$$

In order to get the mass of stars within some mass interval, rather than the total number of stars within that interval, we can integrate Φ times the mass per star

$$M_*(M_1, M_2) = \int_{M_1}^{M_2} M \Phi(M) dM \quad (2.3)$$

or

$$\xi(M) \equiv M \Phi(M) = \frac{dM_*}{dM} \quad (2.4)$$

Throughout this thesis this form of the mass function has been used. To better understand how to interpret $\xi(M)$ we can rewrite the relations above such that

$$\xi(M) = M \Phi(M) = M \frac{dN}{dM} = M \frac{d \ln N}{d \ln M} = M \frac{1}{M} \frac{dN}{d \ln M} = \frac{dN}{d \ln M} \quad (2.5)$$

Thus $\xi(M)$ gives the number of stars per logarithm in mass. As star formation takes place over a large mass range, this logarithmic definition is helpful in giving a clear representation of the mass distribution in a galaxy.

We are interested in the distribution of stellar masses rather than the total mass in stars. To compare this distribution between different galaxies, we will have to normalise ξ such that the integral is equal to one:

$$\int_0^{\infty} \xi(M) dM = 1 \quad (2.6)$$

If the function is normalised, $\xi(M) dM$ will give the fraction of stars by mass with masses between M and $M + dM$. Equivalently, if $\Phi(M)$ would be normalised this way, it would give the fraction of stars by number for masses between M and $M + dM$.

A mass function can be constructed for any type of population but the one we are interested in is the initial mass function. This is the mass function for stars that have just formed. The IMF will differ from the present day mass function (PDMF) as stars lose mass throughout their lifetime and more-massive stars will have moved off the main sequence (MS) at a certain age, in a manner dependent on their initial MS mass (Chabrier 2003). However, for stellar masses below $\sim 0.9M_{\odot}$ the MS lifetime is longer than the age of the universe so these stars will not have moved off the MS. Below this mass limit we thus expect the IMF and the PDMF of the stellar population to be the same. This mass limit of stars still on the MS can be derived by combining the expressions for the luminosity of a MS star, the energy produced by hydrogen burning, and the mass-luminosity relation. For a mass-luminosity relation of $L \sim M^{-3.5}$ the resulting expression in terms of solar units becomes

$$\frac{M}{M_{\odot}} \sim \frac{t_{MS,\odot}^{1/2.5}}{t_{MS}} \quad (2.7)$$

For $t_{MS,\odot} = 10^{10} \text{Gyr}$ and the upper limit $t_{MS} \approx 13.8 \text{Gyr}$, $M \approx 0.88M_{\odot}$ is the mass limit for stars that have not evolved off the MS. Recent isochrone models suggest that for solar-metallicity stars under $1 M_{\odot}$ have not moved off the MS in 10Gyr (\cdot).

2.2.1.1 Salpeter IMF

Throughout this thesis, for a bottom-heavy IMF a power-law (i.e. Salpeter-like) IMF is used. This is a power law type IMF as first proposed by Salpeter in 1955 (Salpeter 1955):

$$\xi(m) = C m^{-x} \quad (2.8)$$

where C is the normalisation constant and $x = 1.35$ is the Salpeter exponent. Note that if the form $\Phi(m)$ had been used, this exponent would have been $\alpha = x + 1 = 2.35$. Due to the negative exponent the number of stars or mass in stars decreases strongly with increasing mass, which is why this form of the IMF is ideal to represent a bottom-heavy IMF.

2.2.1.2 Chabrier IMF

A Chabrier (2003) IMF is used for a bottom-light IMF (Chabrier 2003). This IMF can be parameterised in the mass regimes above and below $1 M_{\odot}$ as follows:

$$\xi(m) = \begin{cases} A e^{-(\log m - \log m_c)^2 / 2 \sigma^2} & \text{if } m < 1M_{\odot} \\ B m^{-y} & \text{if } m > 1M_{\odot} \end{cases} \quad (2.9)$$

where $y = 1.3$, $\sigma = 0.69$, and $m_c = 0.079 M_{\odot}$. A and B are the normalisation constants. In the low mass regime, this IMF takes a lognormal form.

2.2.2 Normalisation Constants

The values for the normalisation constants are found by requiring that :

$$\int_{M_l}^{M_u} \xi(m) dm = 1 \quad (2.10)$$

where $M_u = 120 M_\odot$ and $M_l = 0.1 M_\odot$ are the upper and lower mass limits for the normalisation.

2.2.2.1 Normalising the Salpeter IMF

For the Salpeter IMF, we can find the normalisation constant C by requiring

$$1 = \int_{M_l}^{M_u} C m^{-x} dm = C \left[\frac{m^{1-x}}{1-x} \right]_{M_l}^{M_u} = C \frac{M_u^{1-x} - M_l^{1-x}}{1-x} \quad (2.11)$$

so that

$$C = \frac{1-x}{M_l^{1-x} - M_u^{1-x}} \quad (2.12)$$

This constant is written in terms of the Salpeter exponent x and the upper and lower normalisation mass limit, M_u and M_l so that these parameters could be changed if required. For $M_u = 120 M_\odot$, $M_l = 0.1 M_\odot$ and $x = 1.35$, we find that $C = 0.1706$.

2.2.2.2 Normalising the Chabrier IMF

In order to normalise the Chabrier IMF over the entire stellar mass range, the following equations must hold:

$$1 = \int_{M_l}^{1M_\odot} A e^{-(\log_{10} m - \log_{10} m_c)^2 / 2 \sigma^2} dm + \int_{1M_\odot}^{M_u} B m^{-y} dm \quad (2.13)$$

which gives, rewriting the equation using $\log_{10}(x) = \frac{\ln(x)}{\ln(10)}$ such that $c = \ln(10) * b$:

$$1 = A \left[a \sqrt{\pi/2} a \cdot c \cdot e^{c^2/2} \operatorname{Erf} \left(\frac{-\ln a - c^2 + \ln m}{\sqrt{2} c} \right) \right]_{M_l}^{1M_\odot} + B \left[\frac{m^{1-y}}{1-y} \right]_{1M_\odot}^{M_u} \quad (2.14)$$

using the values for a , b and m_c , and putting in this mass limits, this leads to:

$$1 = A \left(0.004 - 0.556 \operatorname{Erf}(0.006 + 0.445 \ln M_l) \right) + B \left(\frac{M_u^{1-y} - 1}{1-y} \right) \quad (2.15)$$

By requiring continuity between the two parametrisations of the mass function at $1 M_\odot$ we can express the constant B in terms of A :

$$B = A \frac{e^{-(\log_{10} 1 - \log_{10} m_c)^2 / (2 \sigma^2)}}{1-y} \quad (2.16)$$

By combining equations (2.15) and (2.16) we can then find the normalisation constants A and B . For $M_u = 120 M_\odot$, $M_l = 0.1 M_\odot$ and $y = 1.3$, we find $A = 0.8435$ and $B = 0.2354$.

2.2.3 Mass Bins

Next the stellar mass bins need to be initialised. These bins will later be used in creating fractional arrays for the IMF and to populate the PDMF. The mass range for these bins is $bin_{low} = 0.1M_{\odot}$ and $bin_{up} = 0.8M_{\odot}$. The upper limit of $0.8 M_{\odot}$ lies slightly below the initial mass for which stars have not moved off the main sequence within the current Hubble time as explained in the Section 2.2.1. The bins are equally spaced in logarithms. For N mass bins, $N + 1$ left and right edges of the bins are needed. These edges are saved in the array $bins[N + 1]$ following :

$$bins[n] = 10^{\log_{10}(bin_{up}) - n * stepsize} \quad (2.17)$$

for n from 0 up to and including N , where $stepsize = \log_{10}(bin_{up}/bin_{low})/N$. In this project $N = 24$, so 24 mass bins have been used, as will be explained in Section 2.2.7.

Recent models indicate that solar-metallicity stars below $1 M_{\odot}$ have not yet moved off the MS as explained in 2.2.1. Increasing the low-mass bin upper limit from $0.8 M_{\odot}$ to $1.0 M_{\odot}$, only changed the resulting PDMF slope by a couple of hundreds at most. We have therefore decided to only extend the upper limit of the mass bin in the σ -IMF model of Section 4.2.

2.2.4 Integrating the Mass Function

The fraction of mass in stars in each stellar mass bin needs to be determined for both the Salpeter and Chabrier IMF, using the respective normalization constants as found from Equation (2.25). For each bin with lower mass edge m_i and right mass edge m_{i+1} , for i from 0 to $N - 1$, the fraction of mass in stars for either the Chabrier or Salpeter IMF $\xi(m)$ is found by

$$f_{imf} = \int_{m_i}^{m_{i+1}} \xi(m) dm < 1 \quad (2.18)$$

resulting in $f_{imf}[N] = [f_0, f_1, \dots, f_{N-1}]$. Solving the integral for the specific types of IMF, including the respective normalisation constant, the resulting expression for f_{imf} will look as follows for the Salpeter case:

$$f_{salp}[i] = \frac{C}{1-x} (bins[i]^{1-x} - bins[i+1]^{1-x}) \quad (2.19)$$

And for the Chabrier IMF case:

$$f_{chab}[i] = A * \left(-0.556 \operatorname{Erf}[0.445 \log(bins[i]) + 0.006] + 0.556 \operatorname{Erf}[0.445 \log(bins[i+1]) + 0.006] \right) \quad (2.20)$$

This expression for the Chabrier fractional mass array will only hold as long as $bin_{up} \leq 1M_{\odot}$. Otherwise the full parametrisation of the Chabrier IMF as in Equation (2.23) will need to be taken into account.

2.2.5 Populating the PDMF

We now have two arrays with the normalised fractions of mass in stars in the mass range $0.1 - 0.8M_{\odot}$, f_{chab} and f_{salp} , one for the Chabrier IMF and one for the Salpeter IMF. With these we can populate the PDMF array: this will be an array with the same N mass bins over the same mass range as f_{salp} and f_{chab} . In the SAM, inherently, stars are formed assuming a Chabrier IMF. However, we reassign these newly formed stars a different IMF, either in post-processing or immediately after the original star formation, and populate the PDMF following this method. Depending on the model, each time stars have been formed in a galaxy in the SAM under a specific condition or in a specific location, cond_1 or cond_2 , they will be assigned to the PDMF of that galaxy following either a Chabrier or Salpeter IMF. Each time stars are formed they are thus reassigned an IMF and are then added to the PDMF, which at $z = 0$ will give the PDMF of that specific galaxy:

$$PDMF_1[N]_{+} = dm_{*}(\text{cond1}) f_{\text{salp}}[N] + dm_{*}(\text{cond2}) f_{\text{chab}}[N] \quad (2.21)$$

This PDMF gives us the fraction of stars in mass in each bin, with masses between M and $M + dM$, i.e. the edges of each bin. This is equivalent to $\xi(M) dM$ as described in Section 2.2.1. To get $\xi(m)$, this PDMF needs to be divided by the dm of each mass bin, $dm_{*}\text{-bins}[N]$. Moreover, in order to normalise the PDMF, it should be divided by the total mass in stars formed over the entire normalisation range (i.e from $0.1\text{-}120 M_{\odot}$). However, this last point will not affect the slope of the resulting PDMF, only the offset. The final expression for the PDMF is then:

$$PDMF[N] = \frac{PDMF_1[N]}{m_{*,\text{tot}} * dm_{*}\text{-bins}[N]} \quad (2.22)$$

2.2.6 Re-assignment of IMF

Note that in all three models the IMF is not implemented self-consistently as we determine the PDMF by re-assign the IMF either in post-processing (models 1 and 2) or in the SAM (model 3) but only after stars have already formed. Stars within the SAM are formed following a Chabrier IMF which translates into on the amount of feedback from stellar winds and SN of massive stars and on the metallicity enrichment and gas loss due to the stellar evolution as further described in Section 1.2.3.5. However, we only alter the low-mass end ($< 1M_{\odot}$) IMF in post-processing which will not affect the feedback mechanisms from higher mass stars. Therefore we except the current implementation of re-assigning the IMF in post-processing to be a reasonable first approximation which will have little effect on the global properties of the galaxies in the SAM. In Fontanot (2014) assigning a bottom-heavy IMF rather than a top-heavy IMF only strongly affect the (evolution of the) metallicities of the hot gas though not the stellar mass function and SFR. A change in metallicity may affect the cooling rate of hot gas which will have an impact on the cold gas and metallicity thereof that is available for star formation at any given time. In them future, the exact effect of varying the low-mass end of the IMF self-consistently within the 'Santa-Cruz' SAM should be tested.

2.2.7 Comparing the model PDMF with the theoretical mass function

To check whether the algorithm to get to the PDMF works well, a pure Chabrier or pure Salpeter PDMF is compared with the respective theoretical input IMF $\xi(m)$. For either a sole Salpeter or a sole Chabrier PDMF, i.e. stellar mass bins populated via either 100 % cond1 or via 100 % cond2, the resulting PDMF is presented in Figure 2.1. The output PDMF of the model is compared with the theoretical input $\xi(m)$ for a Salpeter IMF as given in Equation (2.8) and $\xi(m)$ for a Chabrier IMF as in Equation (2.23). In both cases the output PDMF is the same as the input IMF as it should be.

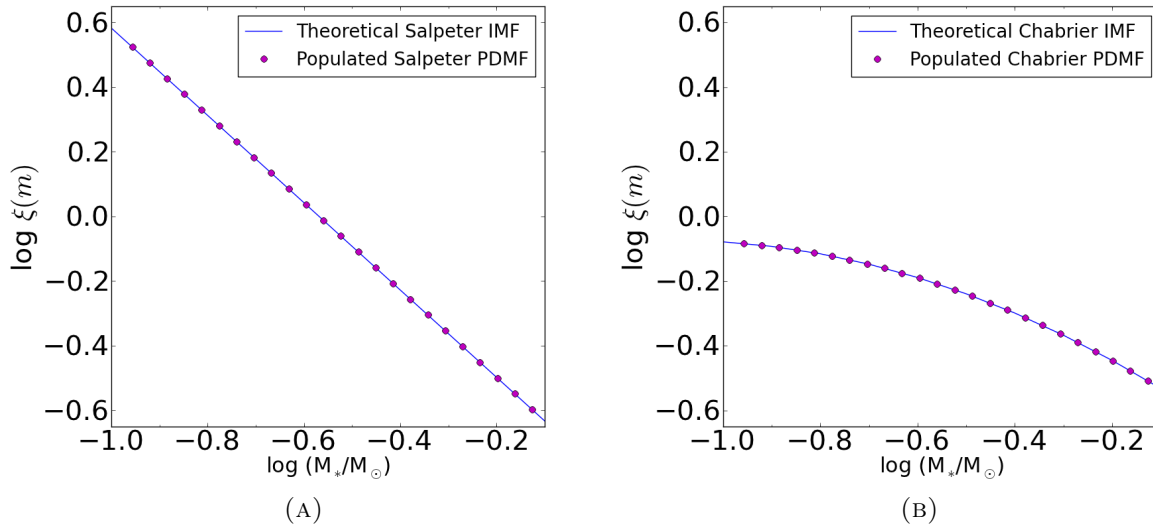


FIGURE 2.1: Comparing the PDMF that follows from the model (red dots) with the theoretical input $\xi(m)$ (blue line), for a pure Salpeter case on the right and a pure Chabrier case on the left. In both cases the output PDMF is the same as the input IMF.

To determine the number of mass bins needed to be sensitive to a change in slope but not to use unnecessary memory or computing power, several N values for the amount of mass bins were tested. In Figure 2.2 the PDMF is shown for 50 % of stellar mass populated following f_{salp} and 50 % following f_{chab} , for respectively 10, 24, and 50 mass bins. The vertical axis shows the $\text{PDMF} \cdot dm_*$, rather than just the PDMF, as this form depicts the change in slope best. As can be seen from Figure 2.2, 24 mass bins represents the change in slope more smoothly than 10 bins but, for our purposes, just as well as 50 bins. So throughout this project $N = 24$ mass bins have been used.

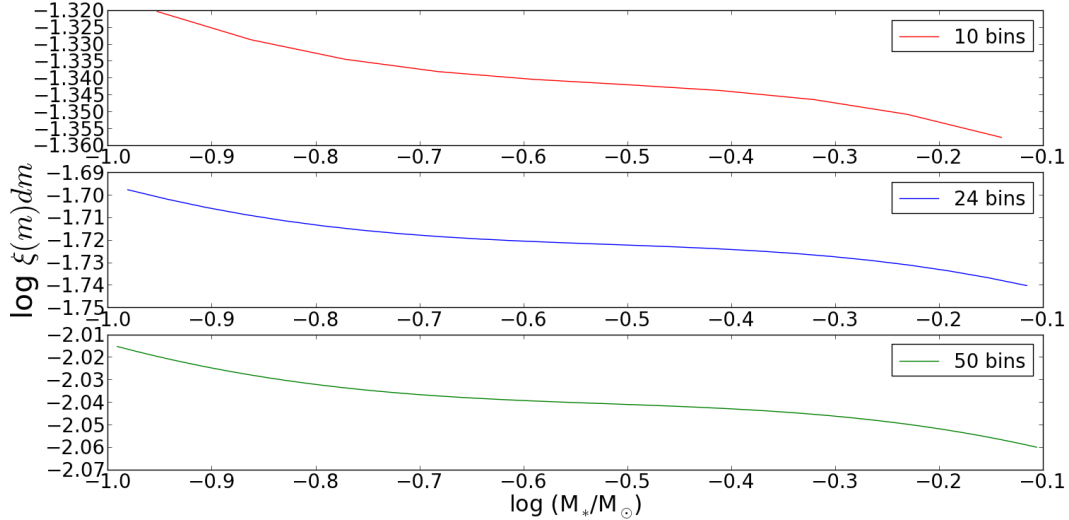


FIGURE 2.2: This figure shows a PDMF which was populated with 50 % of the stellar mass following a Salpeter-like IMF and 50 % of the stellar mass following a Chabrier-like IMF. The PDMF is plotted for 10, 24 and 50 mass bins in the range $0.1\text{--}0.8 M_{\odot}$. The plot for the 10 mass bins shows the change in slope too stochastically, however, both 24 and 50 mass bins present a smooth transition in the curve.

For this reason throughout this project 24 mass bins are used.

2.3 Fitting the PDMF

To get the slope of the PDMF, the relation $y = a * x + b$ is used as a fit. The log of the center of each mass bins (x) is fitted to the log of the PDMF (y), so to the log of the fraction of mass in stars in each bin. The relation $y = a * x + b$ is fitted using python's scipy function `scipy.optimize.curve_fit(f, xdata, ydata)`¹, which uses a non-linear least squares to fit a function f to data. The resulting slope a can then be used to compare to observational values of the PDMF slope. The offset b of this fit is not of interest to this project as it only describes the overall mass normalisation. We are interested in the relative amount of low-mass stars, which is the observed low-mass IMF slope- σ relation. In Figures 2.3a and 2.3b a sole Salpeter or Chabrier populated PDMF respectively are presented with the fitted dashed black line. The slope of the Salpeter PDMF is -1.35 in accordance with the theoretical input value. The slope of the Chabrier PDMF is -0.51 , fitted between 0.1 and $0.6 M_{\odot}$ as in this range the linear fit is more sensitive to the slope of the Chabrier-like curve.

¹for documentation see http://docs.scipy.org/doc/scipy/reference/generated/scipy.optimize.curve_fit.html

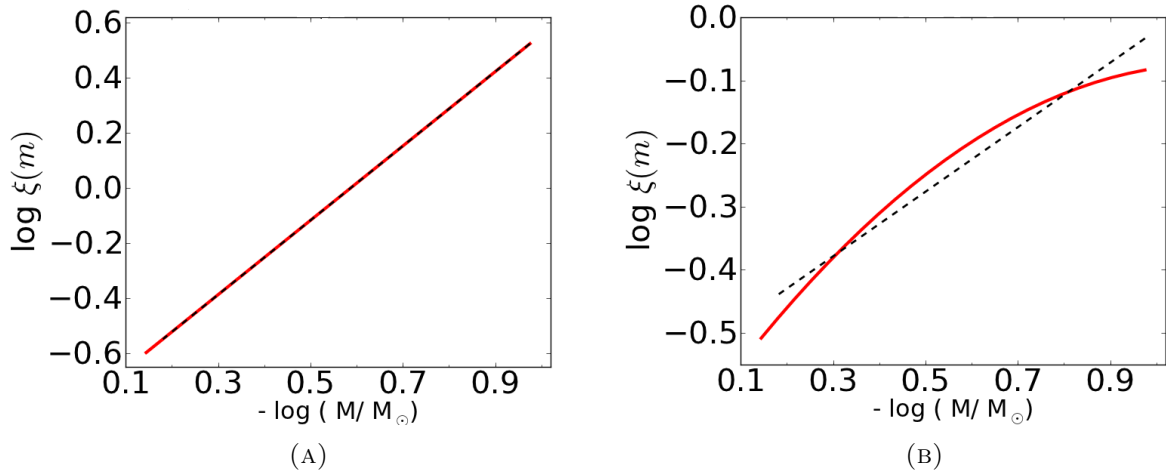


FIGURE 2.3: Fit (dashed black line) to a sole Salpeter populated PDMF (red curve) on the left. The slope of the fit is -0.35. On the right, the fit (dashed black line) to a sole Chabrier populated PDMF (red curve) over the range 0.1 and $0.6 M_{\odot}$. The slope of the fit is -0.51.

2.4 Summary of the PDMF and fitting algorithm

The point wise algorithm for creating and populating the PDMF bins:

I Define the functional form of the Chabier and Salpeter IMF, respectively:

$$\xi(m) = \begin{cases} A e^{-(\log m - \log m_c)^2 / 2 \sigma^2} & \text{if } m < 1M_{\odot} \\ B m^{-y} & \text{if } m > 1M_{\odot} \end{cases} \quad (2.23)$$

where $y = 1.3$, $\sigma = 0.69$, and $m_c = 0.079 M_{\odot}$, and

$$\xi(m) = C m^{-x} \quad (2.24)$$

where $x = 1.35$.

II Find the respective normalisation constants A , B , and C for the Salpeter and Chabrier IMF by requiring that

$$\int_{M_l}^{M_u} \xi(m) dm = 1 \quad (2.25)$$

with $M_u = 120 M_{\odot}$ and $M_l = 0.1 M_{\odot}$

III Generate N number of stellar mass bins in the range $0.1 - 0.8M_{\odot}$ equally spaced in logarithm.

$$\text{bins}[n] = 10^{\log_{10}(\text{bin_up}) - n * \text{stepsize}} \quad (2.26)$$

In this project $N = 24$ mass bins have been used. These mass bins will be populated with formed stars to get the PDMF of galaxies.

IV Determine the fraction of stars in each stellar mass bin for both the Salpeter and the Chabrier case, giving f_{salp} and f_{chab} , by solving this integral

$$f_{imf} = \int_{m_i}^{m_{i+1}} \xi(m) dm < 1 \quad (2.27)$$

where m_i is the left mass bin edge and m_{i+1} the right mass bin edge.

- V Create an empty PDMF array for each galaxy using $\text{bins}[n]$. Populate this PDMF array with stars that have formed in the SAM by reassigning either a Chabrier or Salpeter IMF, using f_{salp} and f_{chab} , to those stars depending on the condition or location of their formation.

$$PDMF_1[N]_{+} = dm_{*}(\text{cond1}) f_{\text{salp}}[N] + dm_{*}(\text{cond2}) f_{\text{chab}}[N] \quad (2.28)$$

The final normalised expression for this PDMF array is

$$PDMF[N] = \frac{PDMF_1[N]}{m_{*,\text{tot}} * dm_{*}\text{-bins}[N]}. \quad (2.29)$$

- VI Determine the slope of the PDMF by fitting the relation $y = a * x + b$ to it. Fit the log of the center of each mass bins (x) to the log of the PDMF (y), so to the log of the fraction of mass in stars in each bin. The resulting slope a can be used to compare to observational values of the PDMF slope.

Models I and II: Star Formation Mode and Morphology Linked to IMF

3.1 Introduction

We investigate different recipes for re-assigning an IMF to stars formed under certain conditions in SAMs and compare the resulting PDMFs of the model galaxies with the observed IMF-slope in local ETGs to gain insight into the origin of the variation in the low-mass IMF. In this chapter two of those recipes will be described. This first recipe is a physically-motivated model that ties the slope of the low-mass IMF to the star formation mode, either quiescently or in bursts; we call this the SF-IMF model. The second recipe is a heuristic model that ties the slope of the low-mass IMF to the present-day location of the stars, either in the bulge or in the disc; we call this the Morph-IMF model.

SAMs connect simple analytic recipes for baryonic processes that govern galaxy formation and evolution to DM merger trees that are formed either via N-body simulations of structure formation (Porter+14) or via the analytic EPS theory (PST14). This method provides global galaxy properties such as stellar mass, size, star formation rate, merger history, and starburst contribution for a statistically large and diverse sample of model galaxies. Moreover, the Porter+14 model is able to compute the velocity dispersion σ of the model galaxies through which we can compare the model results with observed σ -IMF slope relations from for instance Spiniello et al. (2014) directly

The SAM also allows us to determine the fraction of stars per galaxy that have formed under a specific condition or in a specific location. We will use this property of the model to re-assign a bottom-light or bottom-heavy IMF to stars formed under different conditions. In the SF-IMF Model, we assign a bottom-light Chabrier IMF to stars formed in a quiescent environment and a bottom-heavy Salpeter IMF to stars formed in bursts as theories on the origin of the CMF and IMF expect that increased turbulence in the “parent” molecular cloud leads to increased dwarf formation (Hennebelle and Chabrier 2008, 2009; Hopkins 2012a,b, 2013; Padoan and Jones 1997; Padoan and Nordlund 2002). In the Morph-IMF model we will assign a bottom-light Chabrier IMF to stars presently in the disc of a galaxy and a bottom-heavy Salpeter IMF to stars presently in the bulge of galaxies. This Morph-IMF model will take

merger histories and, when applied to the Porter+14 SAM, migration and formation of stars after disc instabilities into account.

3.2 PST14: Method & Results

3.2.1 Specifications

We run the PST14 model to $z = 0$ with a grid of a 100 haloes with 100 realisations of each halo mass for virial masses between $10^8 - 10^{14} M_\odot$ with a mass resolution of $10^{10} M_\odot$ as SAMs are not yet able to correctly model the star formation histories and other observed properties of galaxies below a galaxy mass resolution of $10^{9-10} M_\odot$ (Somerville et al. 2008; Weinmann et al. 2012). However, if the resolution mass is larger than $0.01 \times$ halo mass, the adopted resolution is $0.01 \times$ halo mass.

A flat Λ CDM cosmology is used with the following parameters: $\Omega_m = 0.28$, $\Omega_\Lambda = 0.72$, $h = H_0/(100 \text{ km s}^{-1}) = 0.70$, $\sigma_8 = 0.812$, $n_s = 0.96$, and $f_b = 0.1658$, the cosmic baryon fraction (Komatsu et al. 2009). All other free galaxy formation parameters are fixed to the values in (Popping et al. 2014) and (Somerville et al. 2012), except $M_{BH,seed} = 1.0 \cdot 10^4 M_\odot$.

3.2.2 SF-IMF Model

We use the results of this run to determine the PDMF of the galaxies that are outputted by the SAM at $z = 0$. The PDMF for each galaxy is constructed by adding re-populating the stars that formed in “quiescent” mode with a Chabrier IMF and the stars that formed through bursts with a Salpeter IMF as described in Section . The PDMF is computed in $N = 24$ stellar mass bins equally spaced in log-space in the mass range $0.1 - 0.8 M_\odot$. For the SF-IMF assignment mode, combining Equations (2.21) and (2.22), the PDMF is assigned through:

$$PDMF[N]_+ = \frac{dm_*(\text{quiescent}) f_{\text{salp}}[N] + dm_*(\text{burst}) f_{\text{chab}}[N]}{m_{*,\text{tot}} * dm_{*,\text{bins}}[N]} \quad (3.1)$$

3.2.2.1 Selection Criteria Galaxies

b The PDMF is only determined for central galaxies at $z = 0$, with a stellar mass above $10^7 M_\odot$ and a non-zero stellar contribution that formed in bursts, to filter low-mass galaxies and satellites out of the results. This allows us to better compare the results to observations of ETGs.

For each of these resulting galaxies, the PDMF (3.1) is fitted by a power law in the range $0.1 - 0.7 M_\odot$ as described in Section 2.3.

3.2.2.2 Results

The SAM outputs global galaxy properties like stellar mass, merger history, starburst contribution. We can use the above method to to qualitatively investigate the slope of the low-mass end of the PDMF versus these typical galaxy properties such as stellar mass and stellar mass through bursts.

We use Table BI from (Arrigoni et al. 2010) to find a rough scaling between (dynamical) stellar mass and velocity dispersion as the PST14 of the SAM does not provide σ_{bulge} . This allows for a comparison of the SAM results with the observed IMF slope– σ relation (see red dashed line in Figure 3.1). The model galaxies from the SAM are colour-coded by the mass-weighted mean age of the current stellar population in the galaxy.

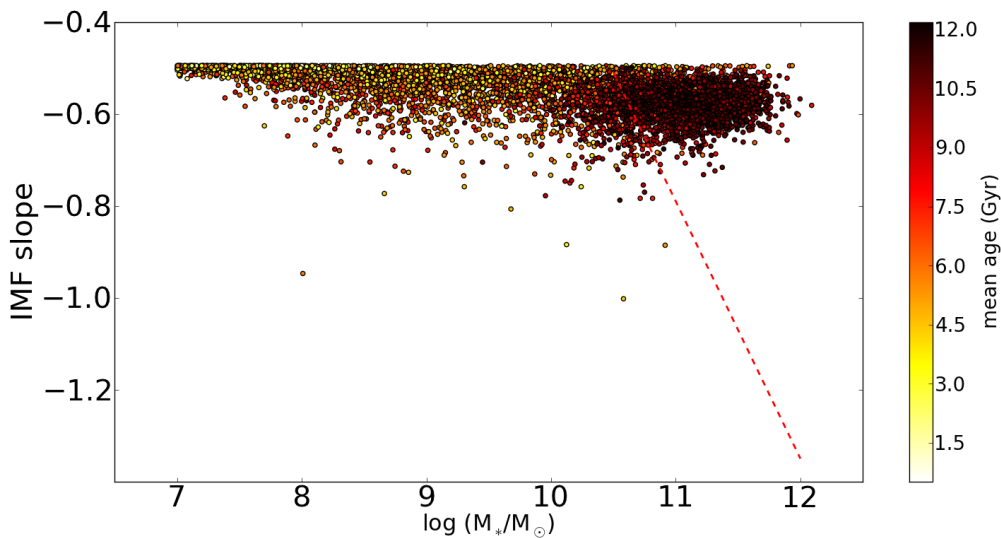


FIGURE 3.1: The PDMF slope versus the total stellar mass for $z = 0$ galaxies from the PST14 SAM to which the SF–IMF model is applied; Stars formed in starbursts in the SAM are re-assigned a Salpeter IMF and stars formed quiescently a Chabrier IMF. Only central galaxies at $z = 0$ with $M_* > 10^7$ and with a non-zero fraction of stars formed in bursts are presented. The galaxies are colour coded based on mass weighted mean age in Gyr. The red dashed line is the schematic observed σ –IMF slope relation converted to M_* . Although a trend is visible between higher M_* and a steeper slope, this is not as strong and steep as the observed relation. The galaxies with the highest mean age have a higher M_* and a slightly steeper slope, the galaxies thus have more stars formed in starbursts.

In Figure 3.1 we do see a slight trend of the PDMF-slope with total stellar mass, however, not as strong as the observations predict. The ansatz of re-assigning an IMF based on star formation mode is thus not sufficient in reproducing the observed IMF slope– σ relation.

As expected from galaxy evolution theory there is a positive relation between galactic stellar mass and mean age of the stellar population where the most massive galaxies have the oldest stellar populations (Panter and Charlot 2007). The highest mass galaxies, and thus the galaxies with the oldest stellar populations do have a steeper and therefore more bottom-heavy slope than the lower-mass galaxies with a lower mean age. These high-mass galaxies have gone through more mergers and therefore have more, merger-induced, stars formed in bursts whereas the lower-mass galaxies experienced most of their star formation more recently and quiescently (Brennan et al. 2015). However, the outliers are not the galaxies with the highest mass or oldest mean age.

We investigate how burst-mode star formation influences the PDMF by plotting the log of M_{burst} and of M_{burst}/M_{tot} versus the slope. Figure 3.2 shows what was put into the model by construction; a larger fraction of burst-mode SF gives a steeper slope. The mean age colour coding shows that the outliers in terms of steepest slope are not the oldest galaxies. Figures 3.3 and 3.2, however, shows these outliers occur among the galaxies with the highest M_{burst} or actually the highest fraction of stellar mass due to M_{burst} . These are the galaxies that had a recent starburst episode. The average PDMF slope in these galaxies with a recent burst has not been mixed yet by addition of more stars and stellar populations that formed in quiescent mode which would have been assigned a Chabrier IMF which would make the slope shallower.

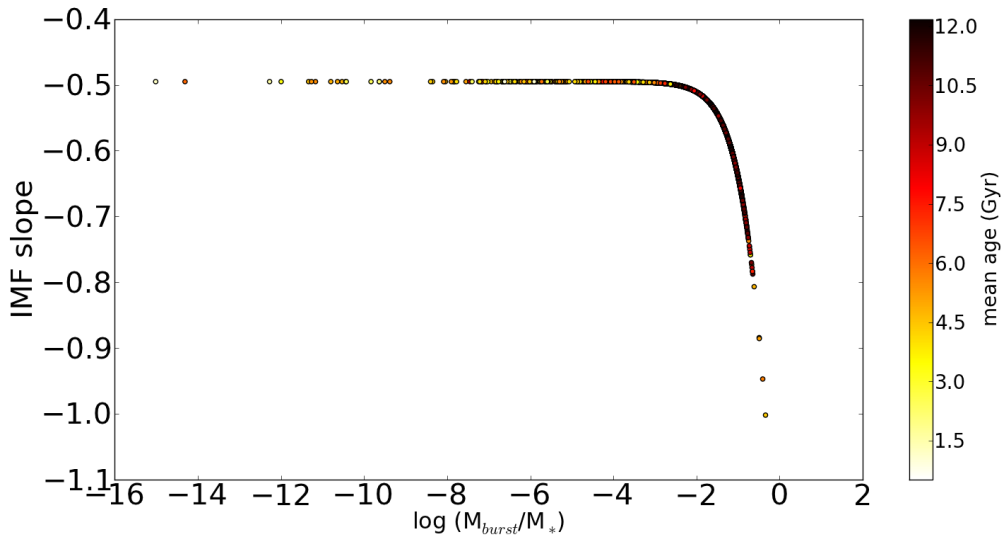


FIGURE 3.2: The PDMF slope versus the fraction of stellar mass due to burst-mode star formation, i.e. M_{burst}/M_{tot} for central model galaxies with $M_* > 10^7$ in the SF-IMF model which re-assigns a Salpter IMF and stars formed quiescently a Chabrier IMF. This figure shows what was put into the model by construction; a larger fraction of burst-mode star formation gives a steeper slope. The galaxies are colour coded by mean age in Gyr, which shows that the outliers in terms of steepest slope are not the oldest galaxies but galaxies with the highest M_{burst}/M_{tot} .

The galaxies with the steepest slope resulting from this model thus formed most of their stars early on or had a recent burst of star formation that contributed to a large fraction of their stellar mass. However, these galaxies and the model population as a whole are not able to reproduce the steepness of the observed slope-mass relation. This could indicate that we would need to expand our criteria for the environments in which stars formed from turbulent gas beyond starburst or to model the starburst physics better, either in the SAM or in the post-processing model.

The PDMF of three model galaxies are depicted in in Figure 3.4 to illustrate how the PDMF slope is derived from actual model galaxies to reach the above relationships between IMF slope and galaxy properties. The PDMF gives the normalised division of number of stars in mass per stellar mass bin at $z = 0$ after they have been re-assigned an IMF in post-processing based on how the stars formed. A linear fit to the number of mass in stars in each bin is performed to find the power-law slope of the low-mass PDMF. We present the PDMF (red-line) and linear fit (black-dashed line) to this PDMF for three model galaxies ; one with the shallowest PDMF slope of the sample, one with an average slope and one with the steepest slope respectively. This slope is determined by the amount of stellar mass in a galaxy through starburst by construction of the model; the galaxy with the largest fraction of stellar mass through bursts has the steepest slope.

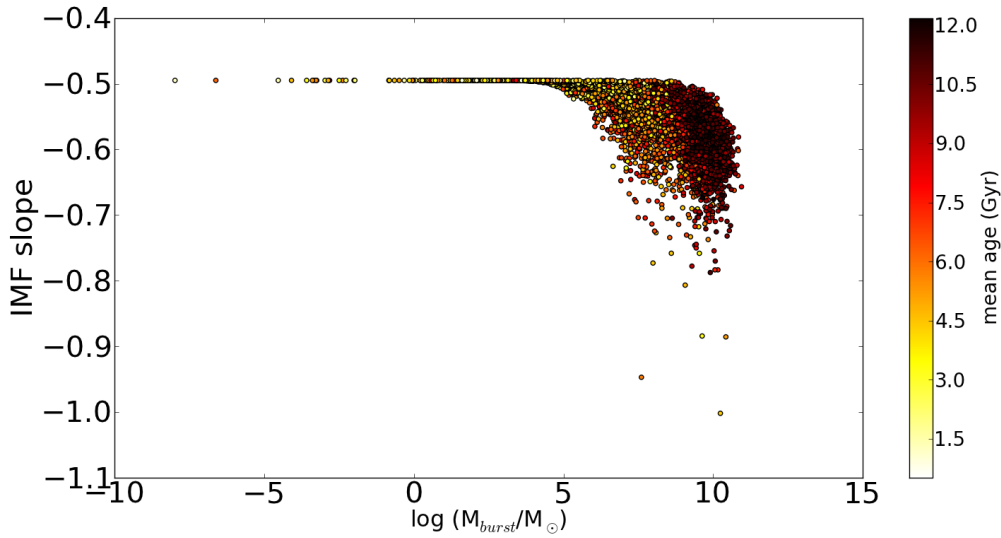


FIGURE 3.3: The PDMF slope versus the stellar mass in per galaxy due to burst-mode star formation for central model galaxies with $M_* > 10^7$ in the SF-IMF model which re-assigns a Salpter IMF and stars formed quiescently a Chabrier IMF. The galaxies are colour coded by mean age in Gyr, which shows that the outliers in terms of steepest slope are not the oldest galaxies. Most outliers are galaxies with the highest M_{burst} but not all as the PDMF slope is determined by both the M_{burst} and M_{normal} . As can be seen in Figure 3.2, the highest M_{burst}/M_{normal} or M_{burst}/M_{tot} will determine the steepness of the PDMF slope in the SF-IMF model.

This burst stellar mass fraction for the three depicted galaxies is respectively $M_*/M_{tot} \sim 0\%$, $\sim 4\%$, and $\sim 46\%$.

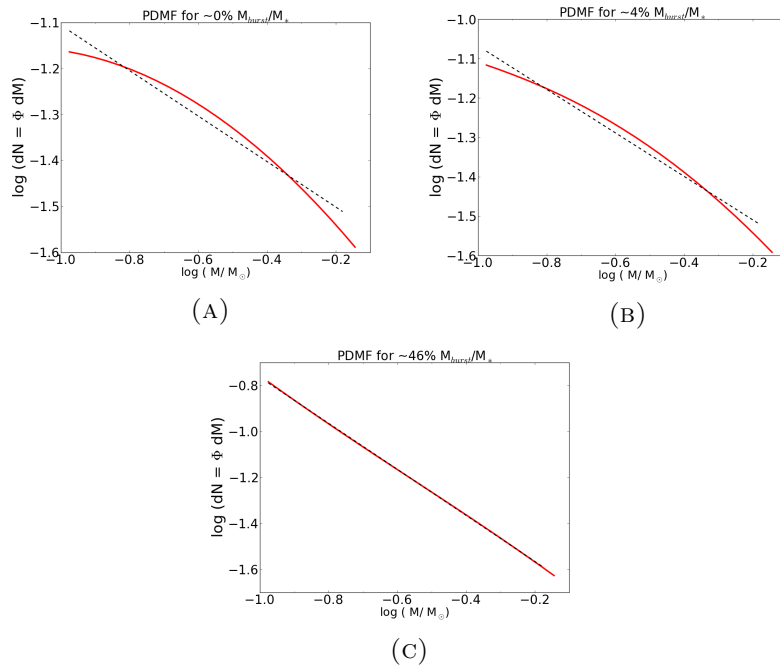


FIGURE 3.4: The PDF (red curve) and linear fit to the PDF (dashed black line) for three model galaxies; One with the lowest fraction of stellar mass through bursts, $M_{burst}/M_{tot} \sim 0\%$, one with an average burst fraction $M_{burst}/M_{tot} \sim 4\%$ and one with the highest burst fraction $M_{burst}/M_{tot} \sim 46\%$. The slope of the linear fit to the PDF of each galaxy gives the PDF slope. By construction of the SF-IMF model, the galaxy with the steepest slope has the highest fraction of stellar mass formed in starbursts.

As a test we increase the power-law coefficient of the input Salpeter IMF to probe the slope required to generate the observed IMF slope-mass relation with our model. An observed system IMF slope is an average of the mass in stars in a certain mass range and it is possible that some of the individual cases that build up this PDF are much steeper than the final observed slope. In Figure 3.5 it can be seen that even with a Salpeter-like power-law input slope of $x = 3$ for stars formed in bursts, the steepness of the observed slope-mass relation is not reproduced. Changing the input IMF power-law slope for bursts shifts the final PDF slope down by at most a factor of 1. However, such a strong increase in IMF slope would have serious implications on the feedback mechanisms and evolution of the subsequent stellar populations in the model and does not represent observations (see e.g. (Bastian and Meyer 2010)). A power-law slope of $x = 3$ would be almost twice as steep than the steepest observed IMF-slope from Spiniello et al. (2014).

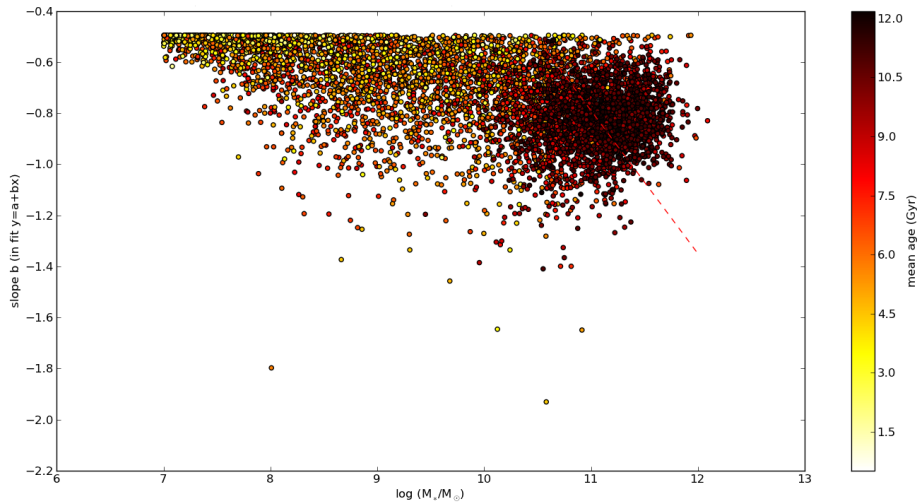


FIGURE 3.5: The PDMF slope versus stellar mass for model galaxies for the SF-IMF model in which we increase the power-law coefficient of the input Salpeter IMF from $x_{salp} = 1.35$ to $x = 3$ that we assigned to burst-mode star formation in the SF-IMF model to probe the slope required to generate the observed IMF slope-mass relation. This increased input slope to an unobserved high value is also not able to reproduce the observed steepness of the stellar mass-IMF slope relation.

The mean age of the outliers in Figure 3.1, 3.3 and 3.2 in terms of slope is relatively low. These galaxies have a younger stellar population with the largest stellar fraction due to starbursts giving these galaxies a lower M/L ratio than the high mass galaxies with old stellar populations. As explained in the Section 1.1.2, Cappellari et al. (2012) have found a strong systematic variation in IMF in ETGs with M/L ratio which suggest a dependence of IMF on the galaxies formation history. In Figure 3.6 we therefore investigate the M/L -slope relation of our model. The SAM gives the absolute magnitude of the model galaxies in different filters. The SAM constructs photometric information on the model galaxies based on Chabrier isochrones in the spectral energy distribution distribution (SED) model from Bruzual and Charlot (2003). To find L_V from these absolute magnitudes in the V -band we use

$$\frac{L_V}{L_\odot} = 10^{(M_{V,\odot} - M_V)/2.5} \quad (3.2)$$

with $M_{V,\odot} = 4.83$. This has been used to derive the M_*/L_V - slope relation in Figures 3.6 and 3.7.

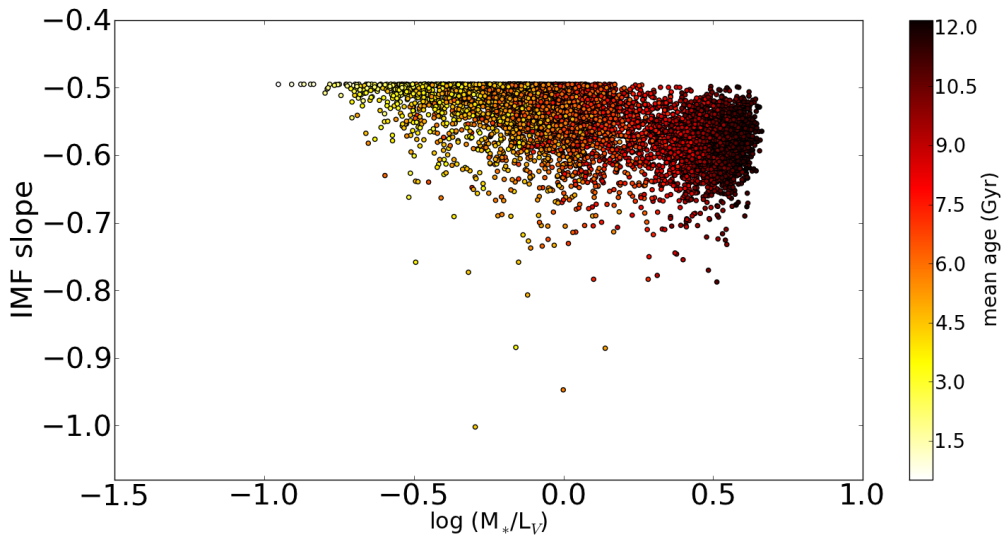


FIGURE 3.6: The PDMF slope versus M/L_V relation of model galaxies for the SF-IMF model. The galaxies with the steepest slope have a relatively low M/L ratio, indicating recent star formation.

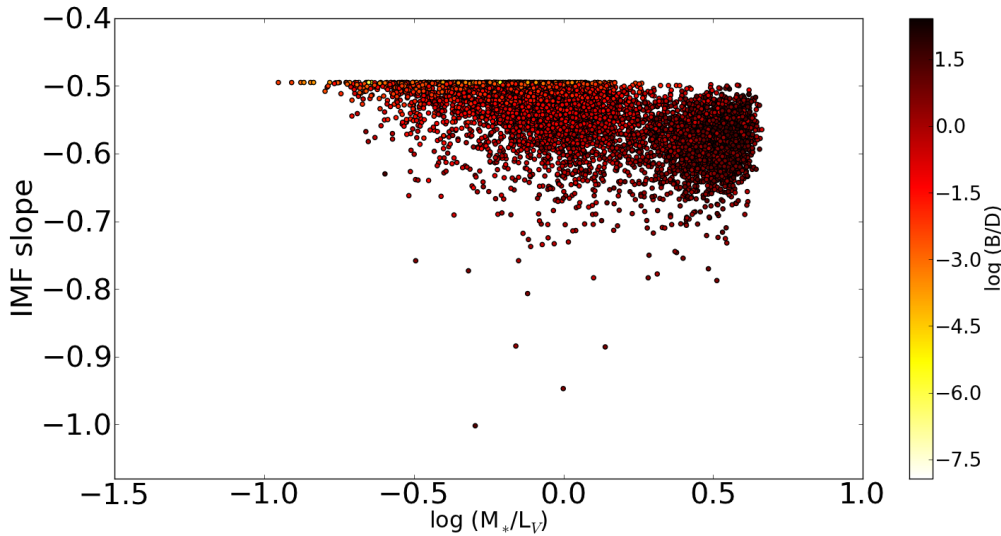


FIGURE 3.7: The PDMF slope versus B/D flux ratio in the B -band of model galaxies for the SF-IMF model. Galaxies with the steepest slope have a relatively high bulge-to-disc flux ratio. As this ratio can be used to distinguish between galaxy morphology we will use it ratio to divide the model galaxies into morphological class in Figure 3.8.

From Figure 3.6 confirms that galaxies with the steepest slope indeed have a relatively low M/L ratio. Moreover, in Figure 3.7 we colour coded the galaxies according to the bulge-to-disc flux ratio in the B -band, which shows that galaxies with the steepest slope have a relatively high bulge-to-disc flux ratio.

The bulge-to-disc (B/D) or bulge-to-total (B/T) ratio can be used as a criteria to distinguish between galaxy morphology. As we see a connection between IMF slope and B/D ratio in Figure 3.7, we will use this to further investigate the relationship between IMF slope and

different types of galaxies in the SF–IMF model. Graham and Worley (2008) derived the dust-corrected B/D ratio in several bands as derived from observed fluxes as a function of galaxy type for a set of galaxies with catalogued Hubble type. As these values from Graham and Worley (2008) are dust-corrected, we use the SAM galaxy magnitudes that are modeled without dust in the B -band. The SAM outputs the absolute and total magnitude. Using Equation (3.2) we can convert these into $L_{B,tot}$ and $L_{B,bulge}$, where $L_{B,\odot}$. From this B/T ratio we get B/D through

$$B/D = \frac{1}{(T/B) - 1} \quad (3.3)$$

We use the $\log(B/D)$ – morphological type classification in the B -band from (Graham and Worley 2008) to distinguish between spirals ($\log(B/D) \leq -0.71$), S0s ($-0.71 < \log(B/D) \leq -0.46$), and ellipticals ($\log(B/D) > -0.46$). The galaxies colour coded by this morphological division from B/D ratio in the B -band are presented in Figure 3.8. The dashed yellow line is a fit to the slope of only the elliptical population.

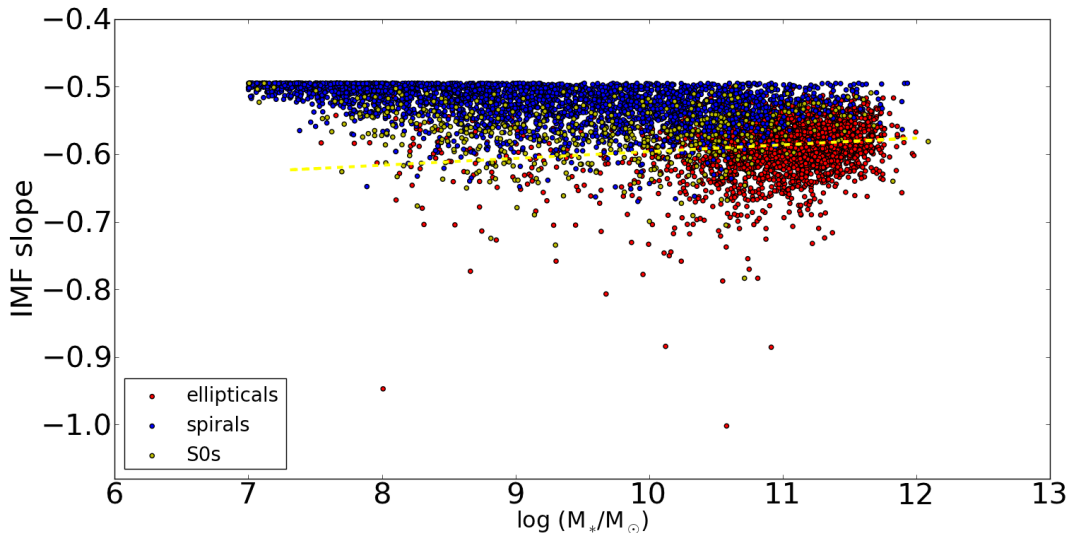


FIGURE 3.8: The PDMF slope versus stellar mass of model galaxies for the SF–IMF model which are colour coded based on B/D B -band flux ratio – morphology class distinction from Graham and Worley (2008) where spirals have $\log(B/D) \leq -0.71$ (blue), S0s have $-0.71 < \log(B/D) \leq -0.46$ (green), and ellipticals have $\log(B/D) > -0.46$ (red). The yellow dashed line is a linear fit to the stellar mass – PDMF slope relation for only the ellipticals in this sample of model galaxies. Although the galaxies with the steepest slopes in the SF – IMF model are elliptical galaxies, a fit to the IMF slope – mass relation of these ellipticals in the SF–IMF model does not reproduce the observed IMF slope – mass relation in ETGs, it even predicts a decline in IMF slope with increasing mass instead of an increase.

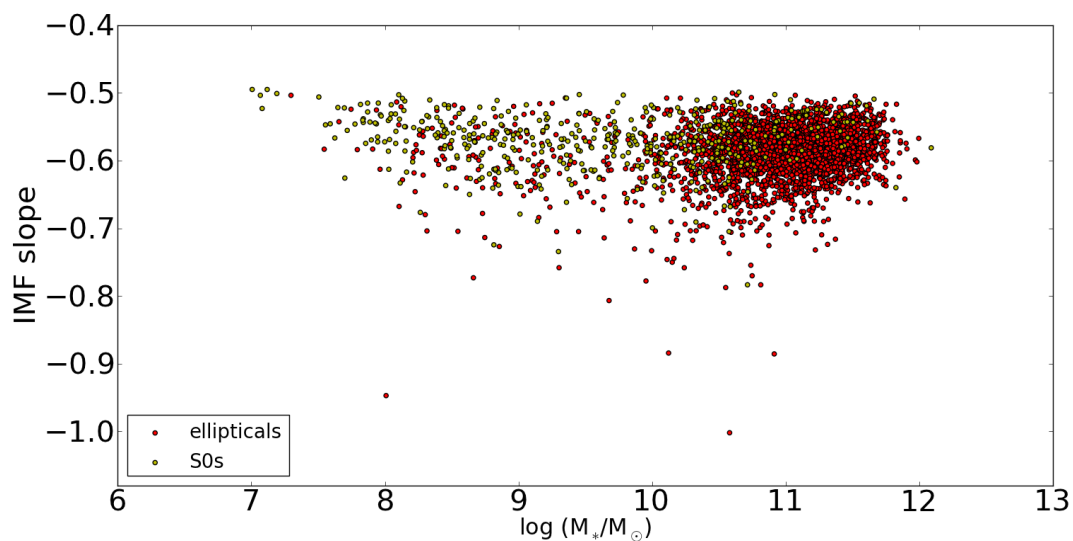


FIGURE 3.9: The PDMF slope versus stellar mass of model galaxies for the SF-IMF model which are colour coded based on B/D B – band flux ratio – morphology class distinction from Graham and Worley (2008). Only the elliptical (red) and S0 (green) galaxies are shown as these galaxies have been observed to have a IMF slope – σ relation that is steeper than in the Milky Way. The SF-IMF model is not able to reproduce the observed IMF slope – mass relation in ETGs, however, we do find the galaxies in our SF-IMF model that have the steepest slopes are ellipticals and S0s which indicates that we could extend our criteria for IMF assignment beyond SF mode to possibly a variation based on the B/D ratio or morphology of the galaxy.

Figure 3.9 isolates the ellipticals and S0s from the full sample. The galaxies with the steepest slopes are ellipticals and S0s, which are expected to have the most stellar contribution due to starbursts in the SAM (Brennan et al. 2015).

3.2.3 Morph–IMF Model

Figures 3.8 and 3.9 indicate that we could extend our criteria for IMF assignment beyond SF mode to possibly a variation based on the B/D ratio or morphology of the galaxy. The B/D ratios represent the formation history of galaxies as bulge dominated galaxies are the results of mergers and subsequent burst induced star formation whereas discs form through gravitational collapse and grow through quiescent star formation out of cold gas that falls into the disc (Brennan et al. 2015). Although, elliptical galaxies can also be the result of the merger of two spiral galaxies whose stars formed quiescently (Schweizer 1982; Toomre and Toomre 1972). The B/D ratio can thus be seen as an indirect tracer of the environment in which the bulk of the stars in a galaxy formed. (Dutton et al. 2013) find that strong lensing and gas kinematics of the bulges of massive spiral galaxies from the SWELLS survey can be best fitted by stellar population synthesis models with a Salpeter-like IMF. The disc masses, though less constrained by lensing and dynamics, are consistent with a Chabrier-like IMF.

We therefore apply a different IMF assignment method based on the present-day location of stars either in the disc or bulge to the same run of the SAM as described in Section 3.2.1. Stars that at $z = 0$ are in the disc were assigned a Chabrier IMF and those in the bulge a Salpeter IMF for N_{24} mass bins ranging from $0.1 - 0.8M_{\odot}$ following

$$PDMF[N]_{+} = \frac{dm_{*}(\text{quiescent}) f_{\text{salp}}[N] + dm_{*}(\text{burst}) f_{\text{chab}}[N]}{m_{*,\text{tot}} * dm_{*}\text{-bins}[N]} \quad (3.4)$$

3.2.3.1 Results

This Morph-IMF model gives the IMF slope–stellar mass relationship in Figures 3.10 and 3.11, colour coded by respectively the mass weighted mean age and the morphological type based on the B/D-flux ratio in the B -band as before.

As can be seen from Figures 3.10 and 3.11 this IMF assignment method produces a much steeper IMF slope–stellar mass relation than the SF assignment method though it does not yet reproduce the offset and slope of the observed relation depicted by the red-dashed line in Figure 3.10. The yellow-dashed line in Figure 3.11 is a fit to the slope of only the ellipticals in the sample.

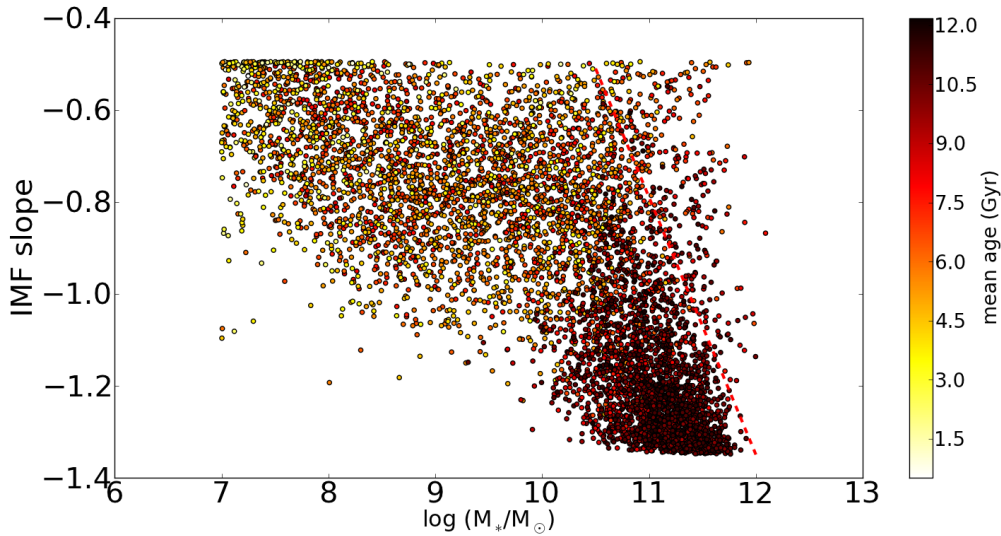


FIGURE 3.10: The PDMF slope versus the total stellar mass for $z = 0$ galaxies from the PST14 SAM to which the Morph-IMF model is applied; Stars in the bulge of the present-day galaxy in the SAM are re-assigned a Salpeter IMF and stars in the disc of the present-day galaxy a Chabrier IMF. Only central galaxies at $z = 0$ with $M_* > 10^7$ and with a non-zero fraction of stars formed in bursts. The galaxies are colour coded based on mass weighted mean age in Gyr. The red dashed line is the schematic observed σ -IMF slope relation converted to M_* . This assignment model based on the present-day location of the stars in a galaxy produces a much steeper IMF slope-stellar mass relation than the SF-IMF model although it does not yet reproduce the offset and slope of the observed relation.

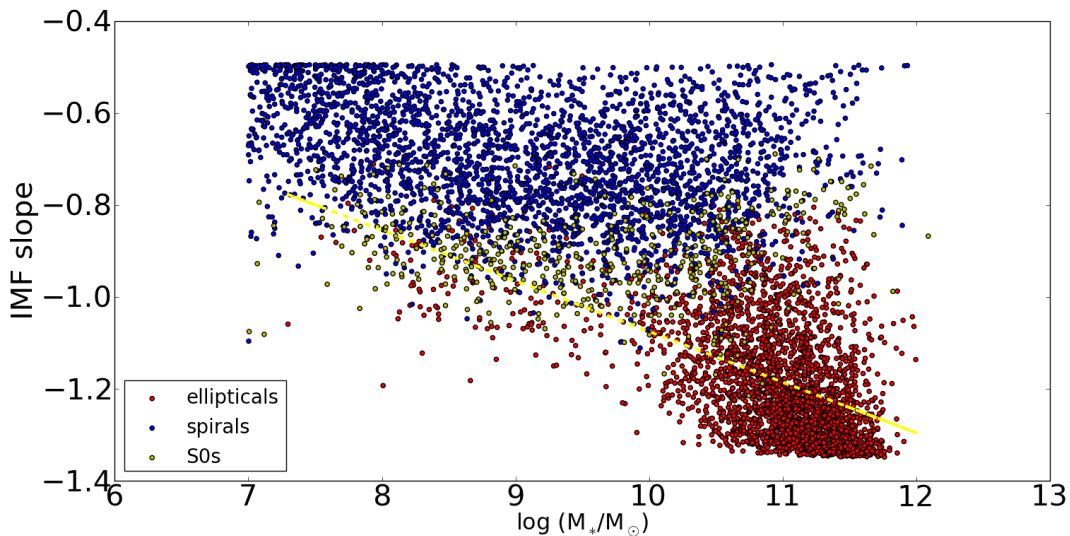


FIGURE 3.11: The PDMF slope versus the total stellar mass for $z = 0$ galaxies from the PST14 SAM to which the Morph-IMF model is applied which are colour coded based on B/D B -band flux ratio - morphology class distinction from Graham and Worley (2008) with ellipticals (red), S0s (green) and spirals (blue). The yellow dashed line is a linear fit to the stellar mass - PDMF slope relation for only the ellipticals in this sample of model galaxies. The IMF slope - stellar mass relation for the ellipticals does not yet reproduce the steepness of the observed Spiniello et al. (2014) relation but does reproduce this relation much better than the SF-IMF model.

3.3 Porter+14: Method & Results

We now apply the SF-IMF and Morph-IMF method to the Porter+14 model. This model provides information on the structural parameters of the spheroid which facilitates comparison of the PDMFs derived from the model with the observed IMF- σ relation. Moreover, unlike the PST14 SAM, it allows for spheroidal growth due to DI when stars and old gas are moved from the disc to the spheroid to create marginal stability. This cold gas will subsequently be used to form stars in a starburst. This better models the physics and morphological formation histories that we are probing with the SF-IMF and Morph-IMF methods.

3.3.1 Specifications

The Porter+14 version uses merger trees from the Bolshoi N-body DM simulation (Klypin et al. 2011), (Trujillo-Gomez et al. 2011) which were generated via the ROCKSTAR method developed by (Behroozi et al. 2014). The simulation follows halos down to $V_{circ} = 50$ km/s or correspondingly $M_{vir} \approx 2 \times 10^{10} M_{\odot}$. The force resolution (i.e. smallest cell size) is $1 h^{-1}$ kpc and the mass resolution (i.e. one particle mass) $1.9 \times 10^8 M_{\odot}$ per particle. The full Bolshoi simulation follows $\sim 8.6 \times 10^9$ particles in a box with sides of $250 \text{ Mpc } h^{-1}$. The cosmological parameters are the same as for the PST14 model as described in Section 3.2.1.

3.3.2 SF-IMF Model & Morph-IMF Model for 4 Merger Trees

We apply the SF-IMF method of Equation 3.1 to the complete merger histories for halos in four $(50 \text{ Mpc } h^{-1})^3$ subvolumes of the Bolshoi simulation (treefiles). We use the tree files without subhaloes because the SAM already tracks the evolution, so merging and tidal stripping and destruction, of subhaloes semi-analytically (Somerville et al. 2008). This results in Figure 3.12. Applying the Morph-IMF method to the same subset of tree files results in Figure 3.13. As for the results in Section 3.2 we only selected the central galaxies that have a stellar mass above $10^7 M_{\odot}$ at $z = 0$ and have a non-zero stellar contribution that formed in bursts. We first apply the SF-IMF and Morph-IMF model to only four tree files in the Porter+14 model to determine whether and how the results differ from the same models applied in PST14. In Section 3.3.3, we will apply the same two models to a larger set of tree files in the Porter+14 model and apply more exclusive filtering criteria for ETGs to better compare the model results with the observations.

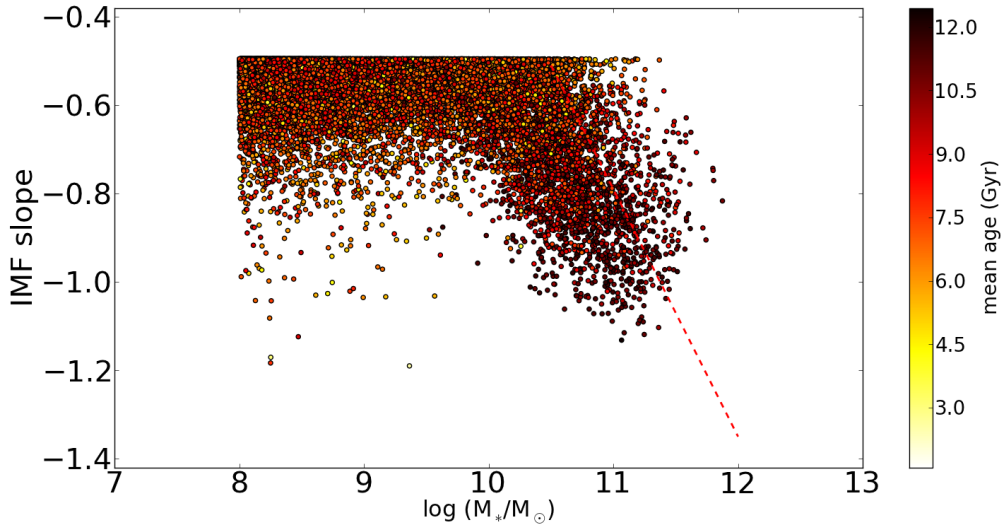


FIGURE 3.12: The PDMF slope versus the total stellar mass for $z = 0$ galaxies for four $(50\text{Mpc h}^{-1})^3$ subvolumes of the Bolshoi simulation in the Porter+14 SAM to which the SF-IMF model is applied. The Porter+14 model can provide structural parameters such as σ for galaxies and models disc instabilities and subsequent spheroid growth due to migration of stars and gas and star bursts. Only central galaxies at $z = 0$ with $M_* > 10^7$ and with a non-zero fraction of stars formed in bursts are presented. The galaxies are colour coded based on mass weighted mean age in Gyr. The red dashed line is the schematic observed σ -IMF slope relation converted to M_* . The SF-IMF model applied to the Porter+14 SAM creates a slightly steeper slope than when applied to PST14 because the burst star formation mode occurs more often as burst-mode star formation after disc instabilities is also taken into account.

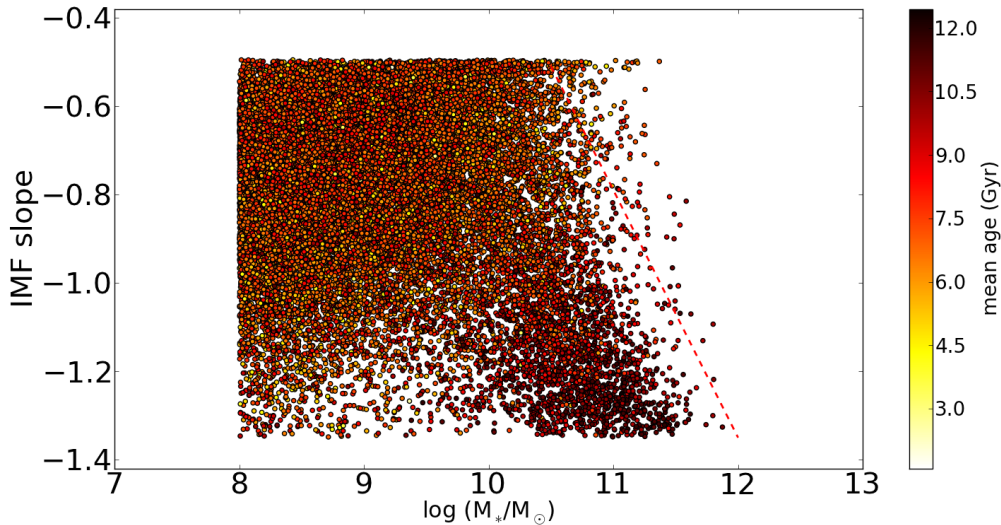


FIGURE 3.13: The PDMF slope versus the total stellar mass for $z = 0$ galaxies for four $(50\text{Mpc h}^{-1})^3$ subvolumes of the Bolshoi simulation in the Porter+14 SAM to which the Morph-IMF model is applied. Only central galaxies at $z = 0$ with $M_* > 10^7$ and with a non-zero fraction of stars formed in bursts are presented. The galaxies are colour coded based on mass weighted mean age in Gyr. The red dashed line is the schematic observed σ -IMF slope relation converted to M_* . The Morph-IMF model applied to Porter+14 model reproduces the steepness of the observed slope, though not the offset, much better than the SF-IMF model or than when applied to the PST14 SAM.

Using the Porter+14 SAM which outputs the σ_{bulge} of each galaxy we can get the PDMF slope as a function of σ_{bulge} in Figures 3.14 and 3.15 for the SF-IMF and Morph-IMF model respectively. These can be directly compared with the observed IMF- σ relation from (Spiniello et al. 2014) (red line).

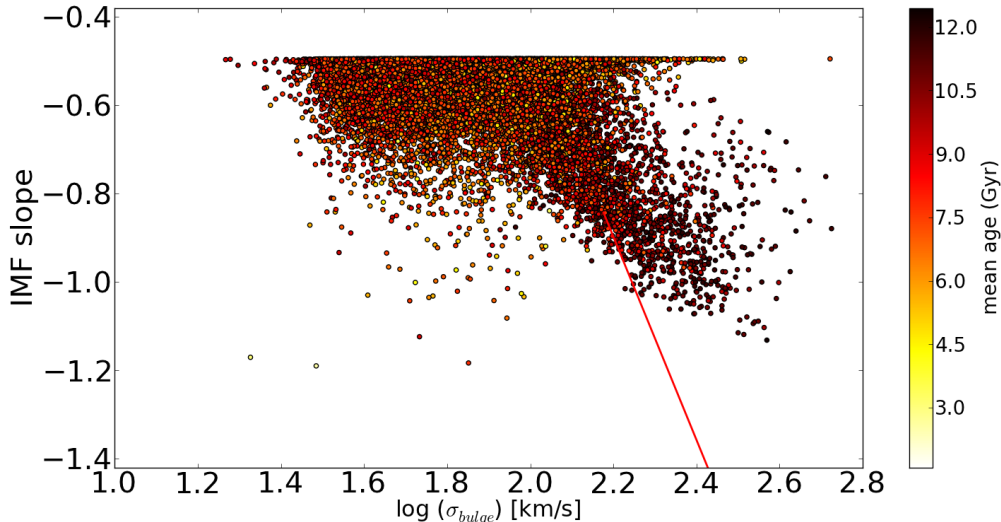


FIGURE 3.14: The PDMF slope versus the σ_{bulge} for $z = 0$ galaxies for four $(50\text{Mpc h}^{-1})^3$ subvolumes of the Bolshoi simulation in the Porter+14 SAM to which the SF-IMF model is applied. Only central galaxies at $z = 0$ with $M_* > 10^7$ and with a non-zero fraction of stars formed in bursts are presented. The galaxies are colour coded based on mass weighted mean age in Gyr. The red line is the observed σ -IMF slope relation from Spiniello et al. (2014). The SF-IMF model does not reproduce the steepness of the σ -IMF slope relation.

The SF-IMF model applied to Porter+14 in Figure 3.12 reproduces a slightly steeper PDMF slope in the high mass end than the same model applied to PST14 in 3.1. The Porter+14 model creates a slightly steeper slope than PST14 because the burst star formation mode occurs more often; It is not only induced after mergers as in PST14 but also after gas migrates from the disc to the spheroid to balance disk instabilities. The SF-IMF model applied to Porter+14 model, however, is still not able to reproduce the observed relation. The Morph-IMF model applied to Porter+14 model in Figure 3.13 reproduces the steepness of the observed slope, though not the offset, much better than the SF-IMF model, as it did when when applied to PST14 in Figure 3.10. The model thus does not generate enough of the highest mass galaxies with a steep slope to reproduce the offset of the observed IMF slope – galaxy mass relation.

Similarly, the σ_{bulge} -PDMF slope relation of the Morph-IMF model in Figure 3.15 is much steeper than of the SF-IMF model in Figure 3.14. This correspondence between the σ_{bulge} -PDMF slope and M_* -PDMF slope relation is expected as σ is known from observations to roughly scale as a power law with M_* (Faber and Jackson 1976).

In Figures 3.16 and 3.17 we separate the morphological classes of the $z = 0$ galaxies using the B/D flux ratio in the B -band as described above. However, the Porter+14 model outputs the magnitudes in the Gunn g' and r' -band, so we convert these values to the Johnson B -band using the corresponding filter transformations from Windhorst et al. (1991). The yellow line is a linear fit to the PDMFs slope as a function of the galaxy's total stellar mass of only the elliptical galaxies (red dots). We see that the galaxies with the steepest slope are the ones classified as ellipticals, as in the results for the PST14 version of the SAM.

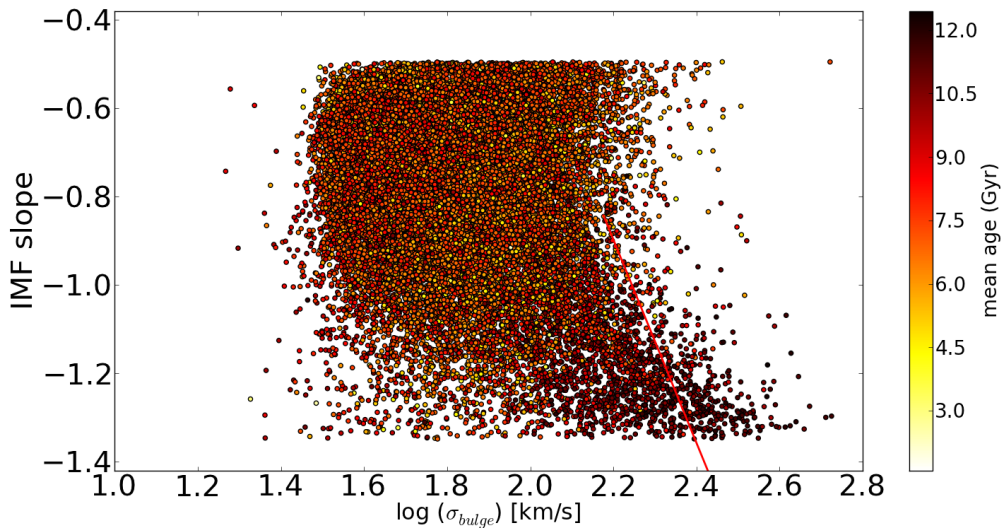


FIGURE 3.15: The PDMF slope versus the σ_{bulge} for $z = 0$ galaxies for four $(50\text{Mpc h}^{-1})^3$ subvolumes of the Bolshoi simulation in the Porter+14 SAM to which the Morph-IMF model is applied. Only central galaxies at $z = 0$ with $M_* > 10^7$ and with a non-zero fraction of stars formed in bursts are presented. The galaxies are colour coded based on mass weighted mean age in Gyr. The red line is the observed σ -IMF slope relation from Spiniello et al. (2014). The SF-IMF model does not reproduce the offset of the observed σ -IMF sloped relation but it does reproduce the steepness much better than the SF-IMF model. This result is similar to the PDMF slope – stellar mass relation from the Morph-IMF model as σ is known from observations to roughly scale as a power law with M_* (Faber and Jackson 1976).

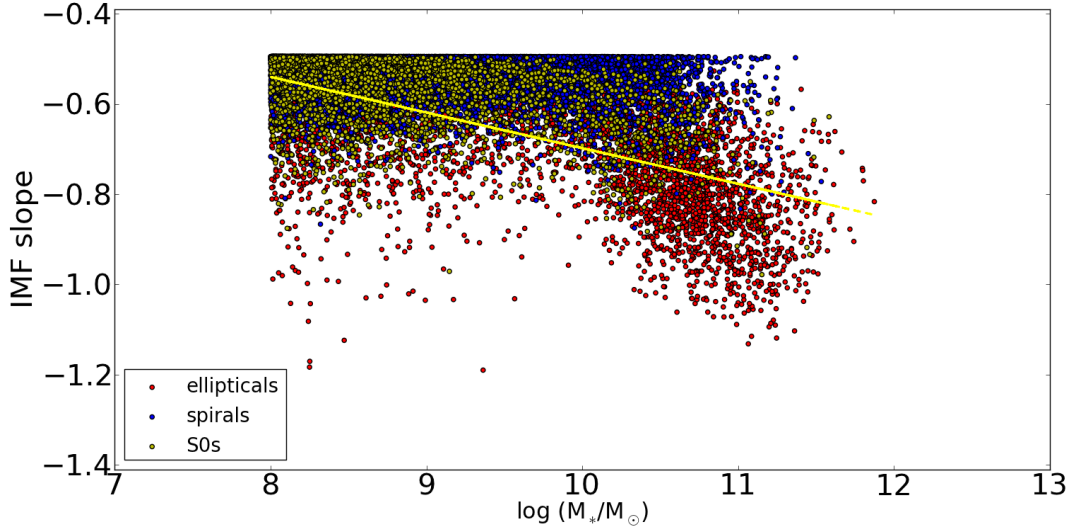


FIGURE 3.16: The PDMF slope versus the total stellar mass for $z = 0$ galaxies for four $(50\text{Mpc h}^{-1})^3$ subvolumes of the Bolshoi simulation in the Porter+14 SAM to which the SF-IMF model is applied which are colour coded based on B/D B – band flux ratio – morphology class distinction from Graham and Worley (2008) with ellipticals (red), S0s (green) and spirals (blue). The yellow line is a linear fit to the stellar mass – PDMF slope relation for only the ellipticals in this sample of model galaxies. Galaxies with the steepest slope are the ones classified as ellipticals although the fit to the stellar mass – PDMF slope relation of the ellipticals does not reproduce the steepness of the observed relation.

3.3.2.1 Updated Selection Criteria Galaxies: Observed ETGs

We apply a further filter to the galaxies to match the selection criteria of the observational relation for ETGs from Spiniello et al. (2014) we compare our results to as much as possible. We

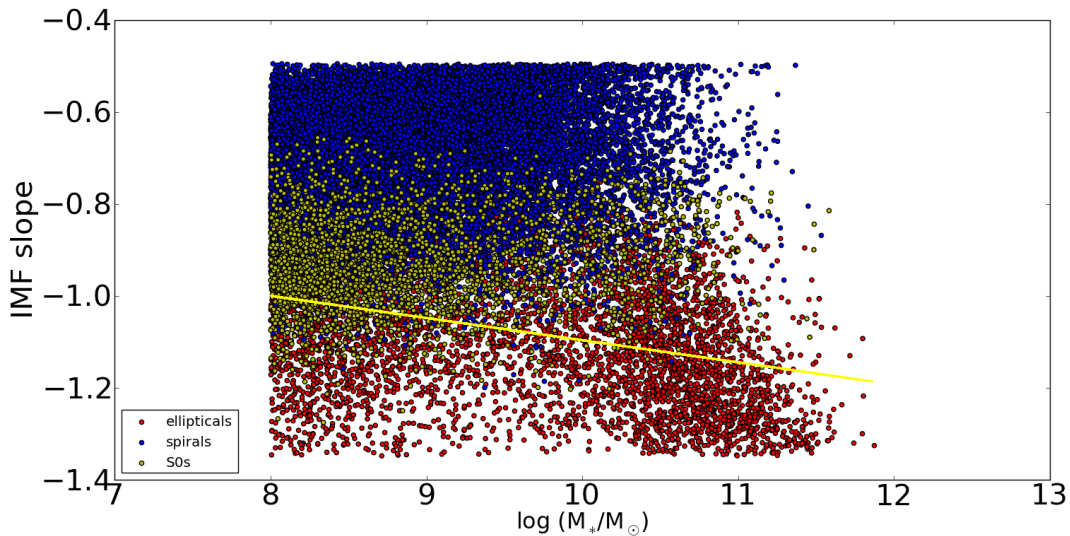


FIGURE 3.17: The PDMF slope versus the total stellar mass for $z = 0$ galaxies for four $(50\text{Mpc h}^{-1})^3$ subvolumes of the Bolshoi simulation in the Porter+14 SAM to which the Morph-IMF model is applied which are colour coded based on B/D flux ratio – morphology class distinction from Graham and Worley (2008) with ellipticals (red), S0s (green) and spirals (blue). The yellow line is a linear fit to the stellar mass – PDMF slope relation for only the ellipticals in this sample of model galaxies. Galaxies with the steepest slope are the ones classified as ellipticals although the fit to the stellar mass – PDMF slope relation of the ellipticals does not reproduce the steepness of the observed relation.

select only central galaxies with large stellar masses of $\log(M_*/M_\odot) > 9.5$ as this is where most of the ellipticals reside in Figures 3.16 and 3.17. We select galaxies with a velocity dispersion of $150 \leq \sigma [\text{km s}^{-1}] \leq 310$ and a low star formation rate of $SFR < 0.3 M_\odot \text{yr}^{-1}$ as in (Spiniello et al. 2014). Finally, we only use galaxies with a stellar mass bulge-to-total ratio of $B/T > 0.5$ to select spheroid-dominated early type galaxies as in (Porter et al. 2014b).

Applying this filter to the galaxies in the same four subvolumes as above leads to Figures 3.18 and 3.19. These selection criteria exclude more galaxies from our sample than the criteria used before as can be seen from comparison with Figures 3.14 and 3.15.

Please note that from here onwards, the vertical axis on all figures which shows the low-mass PDMF slope x has been inverted. We fit the PDMF slope resulting from our models using $y = a \times x + b$, where a gives the slope which will be a negative number as can be seen from Figure 3.4. However, our model defines the power-law coefficient of the input Salpeter and low-mass Chabrier IMF as $x = -1.35$ and $y = 1.3$ respectively instead of as $x = 1.35$ as in Spiniello et al. (2014). Therefore the values of the resulting PDMF slope are inverted, so multiplied by -1 , to have the y-axis of our results present the slope in the same manner as Spiniello et al. (2014).

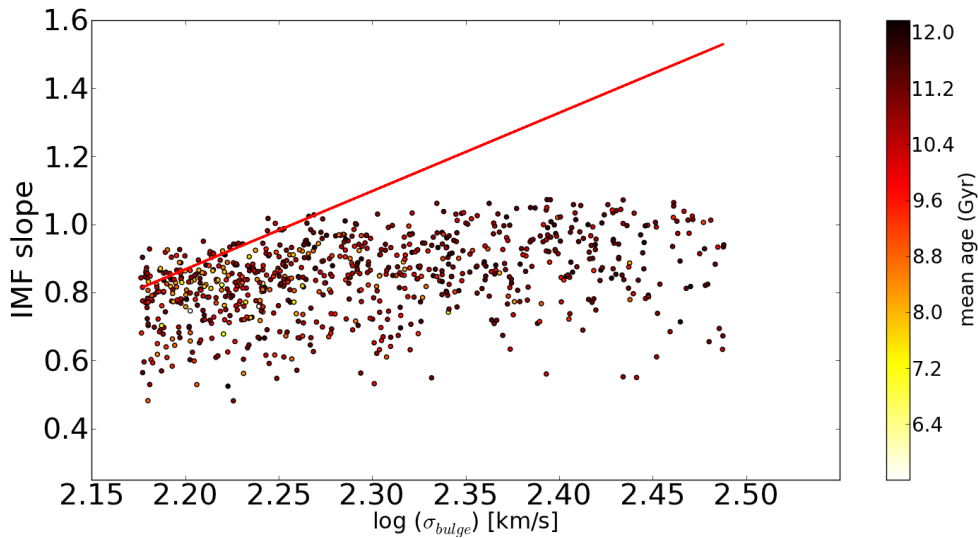


FIGURE 3.18: The PDMF slope versus the total stellar mass for $z = 0$ galaxies for four $(50\text{Mpc h}^{-1})^3$ subvolumes of the Bolshoi simulation in the Porter+14 SAM to which the SF-IMF model is applied filtered to match the selection criteria of the observational relation for ETGs from Spiniello et al. (2014) we compare our results to as much as possible selecting only central galaxies at $z = 0$ with $\log(M_*/M_\odot) > 9.5$, $150 \leq \sigma [\text{km s}^{-1}] \leq 310$, $SFR < 0.3 M_\odot \text{ yr}^{-1}$, and $B/T > 0.5$, stellar mass bulge-to-total ratio. These selection criteria exclude more galaxies from our sample than the criteria used before as can be seen from comparison with Figure 3.14.

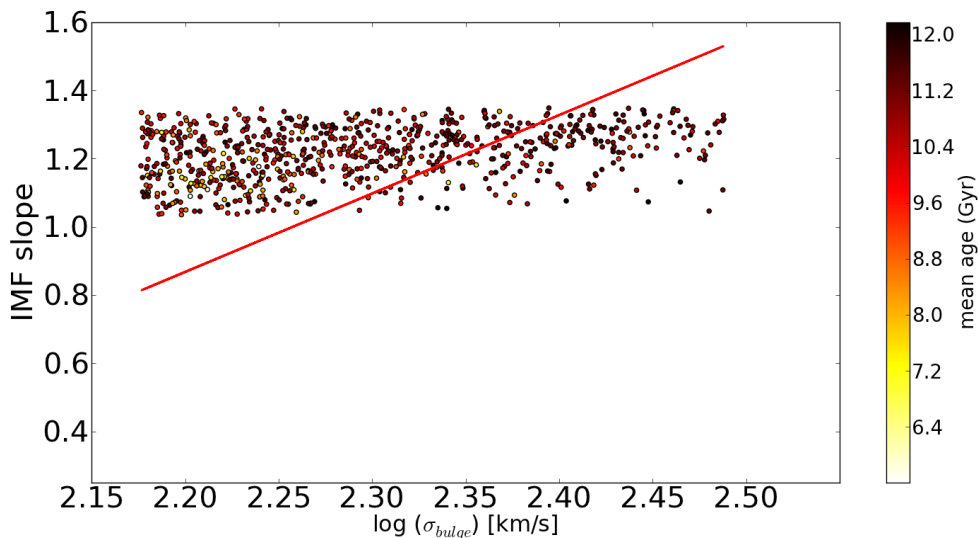


FIGURE 3.19: The PDMF slope versus the total stellar mass for $z = 0$ galaxies for four $(50\text{Mpc h}^{-1})^3$ subvolumes of the Bolshoi simulation in the Porter+14 SAM to which the Morph-IMF model is applied filtered to match the selection criteria of the observational relation for ETGs from Spiniello et al. (2014) we compare our results to as much as possible selecting only central galaxies at $z = 0$ with $\log(M_*/M_\odot) > 9.5$, $150 \leq \sigma [\text{km s}^{-1}] \leq 310$, $SFR < 0.3 M_\odot \text{ yr}^{-1}$, and $B/T > 0.5$, stellar mass bulge-to-total ratio.

3.3.3 SF-IMF Model & Morph-IMF Model for 21 Merger Trees

We now apply the SF-IMF and Morph-IMF model to this galaxy selection to galaxies in 21 subvolumes of $(50\text{Mpc h}^{-1})^3$ of the Bolshoi simulation to get more model points in figures

3.20 and 3.21 respectively.

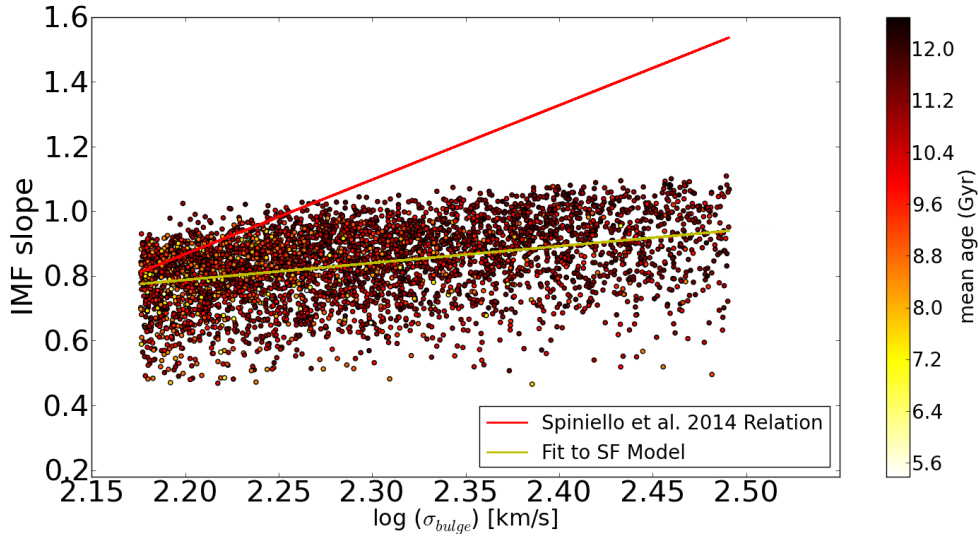


FIGURE 3.20: The PDMF slope versus the σ_{bulge} for galaxies in 21 $(50\text{Mpc h}^{-1})^3$ subvolumes of the Bolshoi simulation in the Porter+14 SAM to which the SF-IMF model is applied. These galaxies are selected to match the selection criteria of ETGs by Spiniello et al. (2014) following Section 3.3.2.1. The yellow line gives the linear fit to the PDMF slope of the model galaxies. The red line is the observed Spiniello et al. (2014) relation. The SF-IMF model only reproduces the observed σ -IMF slope relation for the lowest σ galaxies

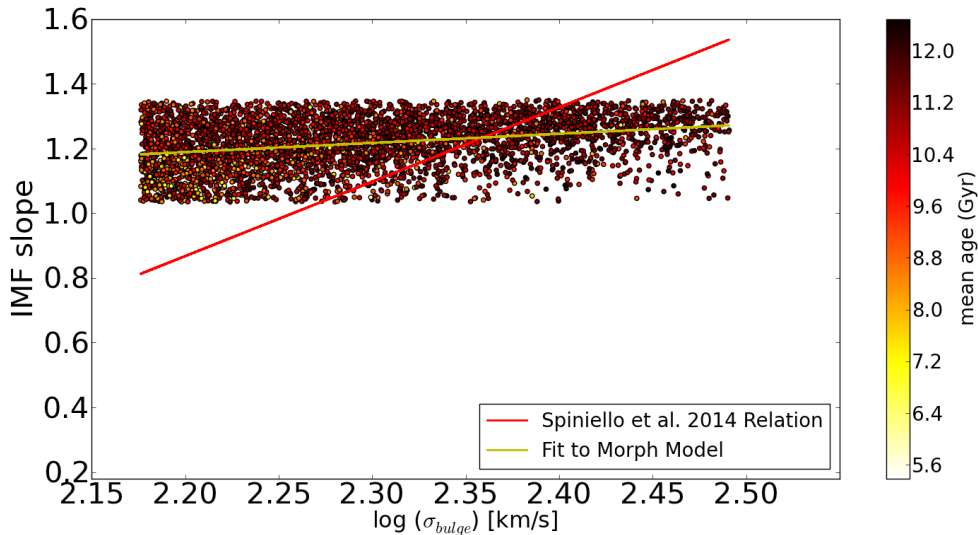


FIGURE 3.21: The PDMF slope versus the σ_{bulge} for galaxies in 21 $(50\text{Mpc h}^{-1})^3$ subvolumes of the Bolshoi simulation in the Porter+14 SAM to which the Morph-IMF model is applied. These galaxies are selected to match the selection criteria of ETGs by Spiniello et al. (2014) following Section 3.3.2.1. The yellow line gives the linear fit to the PDMF slope of the model galaxies. The red line is the observed Spiniello et al. (2014) relation. The Morph-IMF model only reproduces the observed slope relation for the intermediate σ galaxies, over the full σ range it does not reproduce the observed slope of the σ -IMF slope relation.

The yellow line in Figures 3.20 and 3.21 is the fit to the PDMF of the model galaxies; the red line in Figures 3.20 and 3.21 is the observed Spiniello relation. For the SF–IMF model this fit is given by

$$x = -0.36(\pm 0.04) + 0.52(\pm 0.02) \times \log(\sigma) \quad (3.5)$$

For the Morph–IMF model this fit is given by

$$x = 0.57(\pm 0.03) + 0.28(\pm 0.01) \times \log(\sigma) \quad (3.6)$$

The red line is the observed Spiniello et al. (2014) relation

$$x = 1.13(\pm 0.15) + 2.3(\pm 0.1) \times \log \sigma_{200} \quad (3.7)$$

Note that we have modified the Spiniello et al. (2014) relation such that it describes the mass function parametrised as $dN/d \log M$ rather than dN/dM as it does in the original paper.

Spiniello et al. (2014) found this relation by fitting the mean PDMF slope of the observed galaxies in the five σ bins in Table 3.1. Therefore, we also bin the PDMF slope of the model galaxies in the same σ bins and determine the mean and standard deviation of the PDMF slope in each bin. These results are presented in Figures 3.22 and 3.23

TABLE 3.1: The five velocity dispersion bins of the SDSS galaxies in (Spiniello et al. 2014). We will bin the model galaxies using these velocity bins to directly compare the binned σ –IMF slope relation from the model to the observed relation.

SDSS σ_* [km s ⁻¹]
150 ± 20
190 ± 20
230 ± 20
270 ± 20
310 ± 20

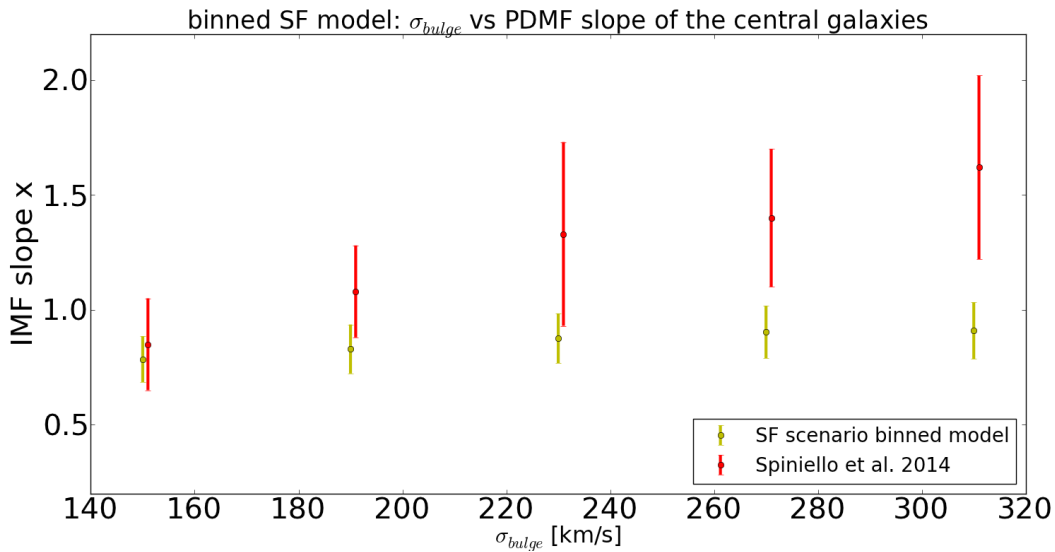


FIGURE 3.22: The binned PDMF slope versus the σ_{bulge} for ETGs in 21 treefiles in the Porter+14 SAM for the SF-IMF model (yellow), binned in the same five σ bins as the Spiniello et al. (2014) observational data (red). The SF-IMF model is able to reproduce the observed IMF- σ relation in the lowest σ bin(s).

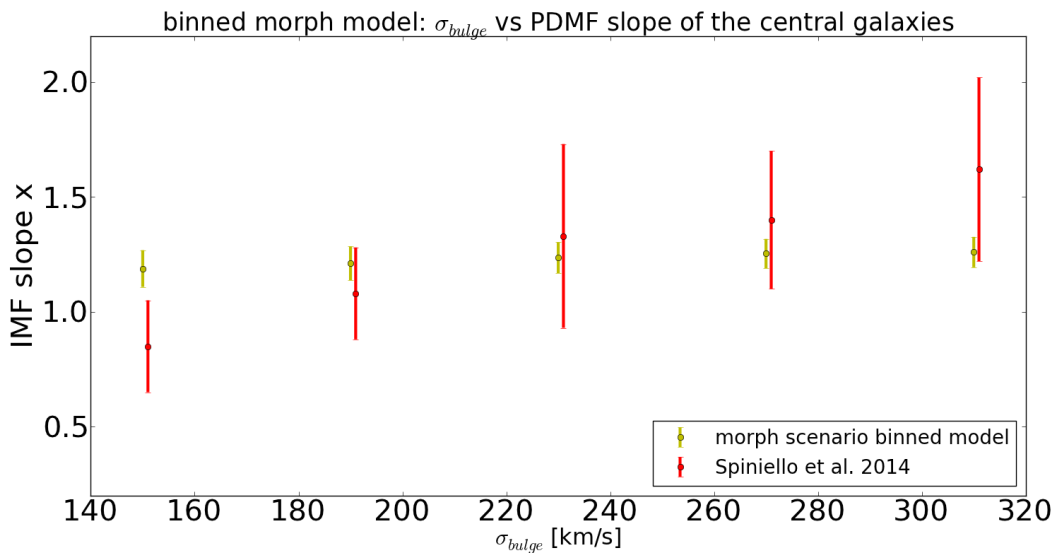


FIGURE 3.23: The binned PDMF slope versus the σ_{bulge} for ETGs in 21 treefiles in the Porter+14 SAM for the Morph-IMF model (yellow), binned in the same five σ bins as the Spiniello et al. (2014) observational data (red). The Morph-IMF model is able to reproduce the observed IMF- σ relation in the higher mass galaxies within the error bars of the observational data. It first the observed relation best in the intermediate σ bin.

We see that the SF-IMF model is able to reproduce the observed IMF- σ relation in the lowest σ galaxies from Figures 3.20 and 3.22. The Morph-IMF model in Figures 3.21 and 3.23, on the other hand, is able to reproduce the observed IMF- σ relation in the higher mass galaxies within the error bars of the observational data.

3.3.3.1 SF–IMF Model & Morph–IMF Model for Power-Law Slope $x = 1.85$

We investigate for which input power-law slope assigned to stars formed in bursts the SF–IMF model is able to reproduce the observed relation. We assign an input power-law IMF coefficient of $x = 1.85$ instead of the Salpeter coefficient 1.35 in Figures 3.24 and 3.25. The red line is the observed Spiniello et al. (2014) relation from Equation (3.7), to be compared with the yellow line in Figure 3.24 which is a fit to the slope of the model galaxies given by

$$x = -0.65(\pm 0.07) + 0.79(\pm 0.03) \times \log(\sigma) \quad (3.8)$$

With a slightly steeper power law slope of 1.85 instead of the Salpeter coefficient of 1.35, the SF–IMF model is able to reproduce the observed IMF slope– σ relation, at least in the three central σ bins, in Figures 3.24 and 3.25. However, such a steep power-law slope has not been observed, at least not in field stars below $1M_{\odot}$ (e.g. see Figure 8 in (Benson 2010)), and is also steeper than observed in ETGs by Spiniello et al. (2014) although it has been observed in ETGs by Ferreras et al. (2013) and LaBarbera et al. (2013).

For comparison, assigning this input power-law slope of 1.85 to present-day bulge stars in the Morph–IMF model will provide PDMF slopes much higher than observed in Figures 3.26 and 3.27. The red line is the observed Spiniello et al. (2014) relation from Equation (3.7), to be compared with the yellow line in Figure 3.26 which is a fit to the slope of the model galaxies given by

$$x = 0.88(\pm 0.04) + 0.35(\pm 0.02) \times \log(\sigma) \quad (3.9)$$

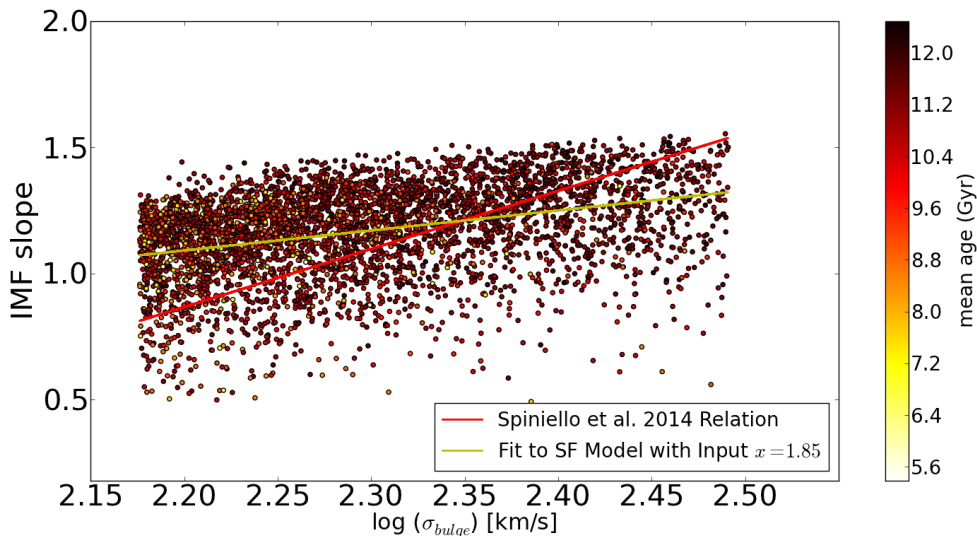


FIGURE 3.24: The PDMF slope versus the σ_{bulge} for ETGs in 21 treefiles in the Porter+14 SAM for the SF–IMF model with the input power-law coefficient for the Salpeter IMF $x = 1.85$ instead of $x = 1.35$ that is assigned to burst-mode star formation in the SF–IMF mode. The yellow line gives the linear fit to the PDMF slope of the model galaxies. The red line is the observed Spiniello et al. (2014) relation.

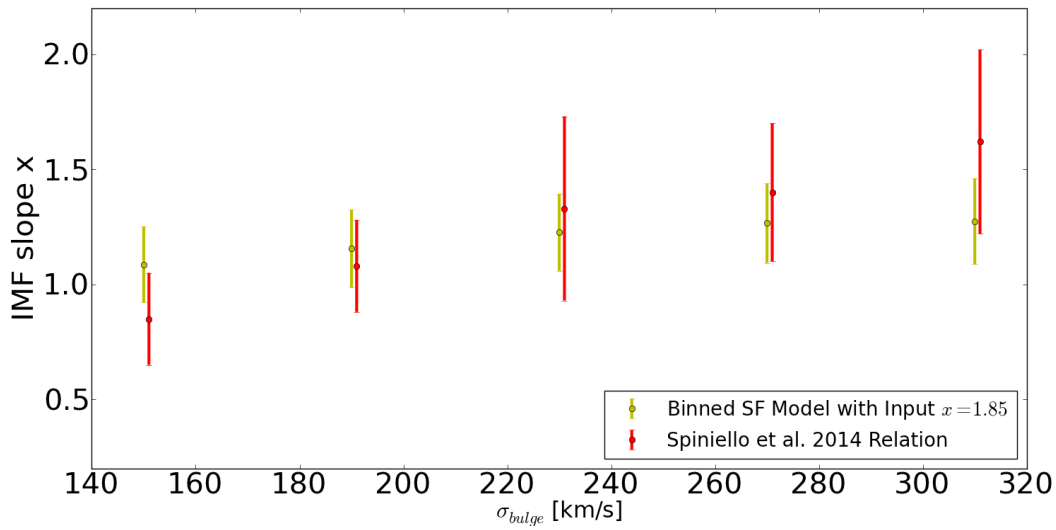


FIGURE 3.25: The binned PDMF slope versus the σ_{bulge} for ETGs in 21 treefiles in the Porter+14 SAM for the SF-IMF model with the input power-law coefficient for the Salpeter IMF $x = 1.85$ instead of $x = 1.35$ that is assigned to burst-mode star formation in the SF-IMF mode. The results are binned in the same five σ bins as the Spiniello et al. (2014) observational data (red). The SF-IMF model is able to reproduce the observed IMF slope- σ relation, at least in the three central σ bins, with this increased input power-law coefficient for the IMF re-assigned to burst-mode star formation.

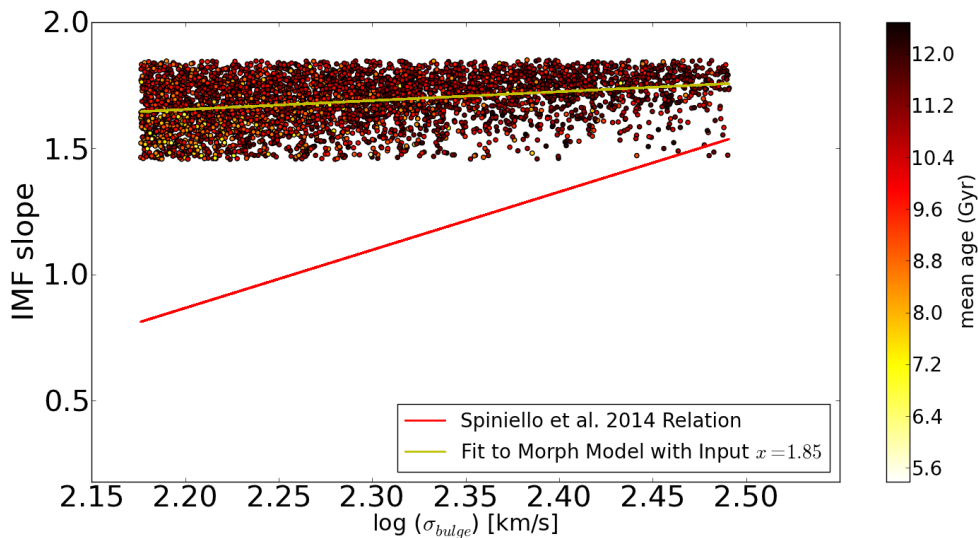


FIGURE 3.26: The PDMF slope versus the σ_{bulge} for ETGs in 21 treefiles in the Porter+14 SAM for the Morph-IMF model with the input power-law coefficient for the Salpeter IMF $x = 1.85$ instead of $x = 1.35$ that is assigned to present-day bulge stars of a galaxy in the Morph-IMF mode. The yellow line gives the linear fit to the PDMF slope of the model galaxies. The red line is the observed Spiniello et al. (2014) relation.

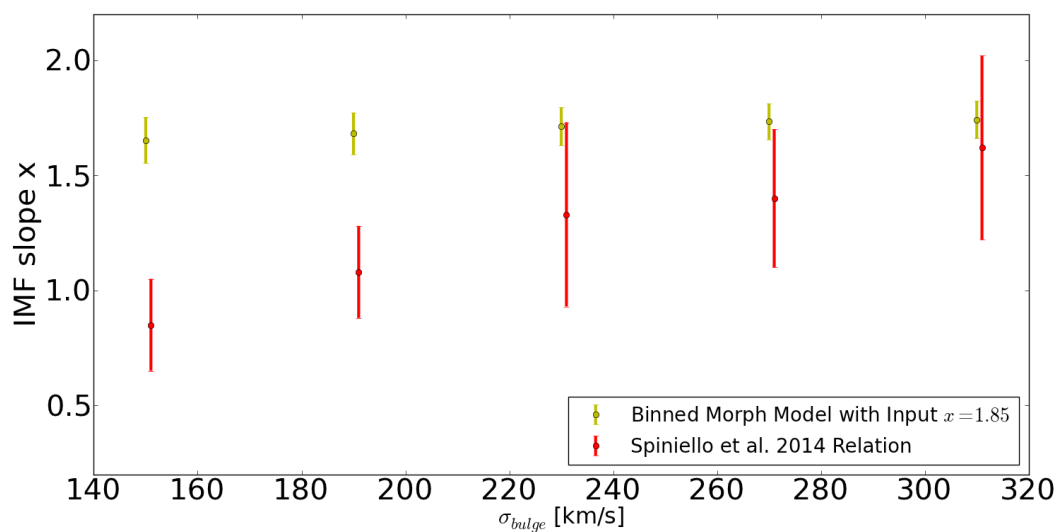


FIGURE 3.27: The binned PDMF slope versus the σ_{bulge} for ETGs in 21 treefiles in the Porter+14 SAM for the Morph-IMF model (yellow) with the input power-law coefficient for the Salpeter IMF $x = 1.85$ instead of $x = 1.35$ that is assigned to present-day bulge stars of a galaxy in the Morph-IMF mode. The results are binned in the same five σ bins as the Spiniello et al. (2014) observational data (red). Increasing the input power-law coefficient in of the IMF re-assigned to present-day bulge stars, generates PDMF slopes much higher than observed in the Morph-IMF model.

3.3.3.2 Selecting Spheroid-Dominated Early Type Galaxies

We do not use the B/D flux ratio to distinguish between morphological types that was used earlier. Instead, in the above sampling of our model galaxies from the Porter+14 model, we have chosen to use a stellar mass B/T criterion of $B/T > 0.5$ to select spheroid-dominated early type galaxies. Cheng et al. (2011) found that a sample of passive, red sequence SDSS galaxies selected with this criterion may include a significant fraction of disc-dominated passive S0 and Sa galaxies. In other literature/research there is wide range in B/T value used to select early type galaxies. Shen et al. (2003) use $B/T > 0.2$ to define early type galaxies whereas others adopt higher cut-off values ranging from $B/T \sim 0.5 - 0.7$ (Shankar et al. 2013; Wilman et al. 2013). Gadotti (2009) found that B/T corresponds more tightly with concentration index in the r -band $c_r \equiv r_{90}/r_{50}$ than with Sérsic index after analysing 1000 SDSS galaxies with bulge-disk decomposition. A B/T of 0.2 is found to correspond to a c_r of 2.86 by Guo et al. (2011). Cheng et al. (2011) show that galaxies selected with $c_r > 2.9$ have a high population of visible bulges with $B/T > 0.5$ but also contains a population of galaxies with $0.2 < B/T < 0.5$. We check the concentration index in the r -band of the selected SDSS galaxies of Spiniello et al. (2014) to determine which B/T we should use for the most consistent comparison of observational and model data. We do this for the galaxies in the four highest velocity dispersion bins Spiniello et al. (2014) used, with outer edges ranging from 170 – 330 km s⁻¹. We retrieve the concentration index for these galaxies from SDSS database using the following criteria in CasJobs:

```
SELECT s.specobjid, s.plate, s.mjd, s.fiberid, s.veldisp, s.veldisperr,
       p.petroR50_r, p.petroR90_r
FROM MyDB.chiarpert AS m
      JOIN SpecObjAll AS s ON (s.plate=$m.plate AND s.mjd=$m.mjd AND s.fiberID=$m.fiber)
      JOIN PhotoTag AS p ON (s.specobjid=$p.specobjid)
```

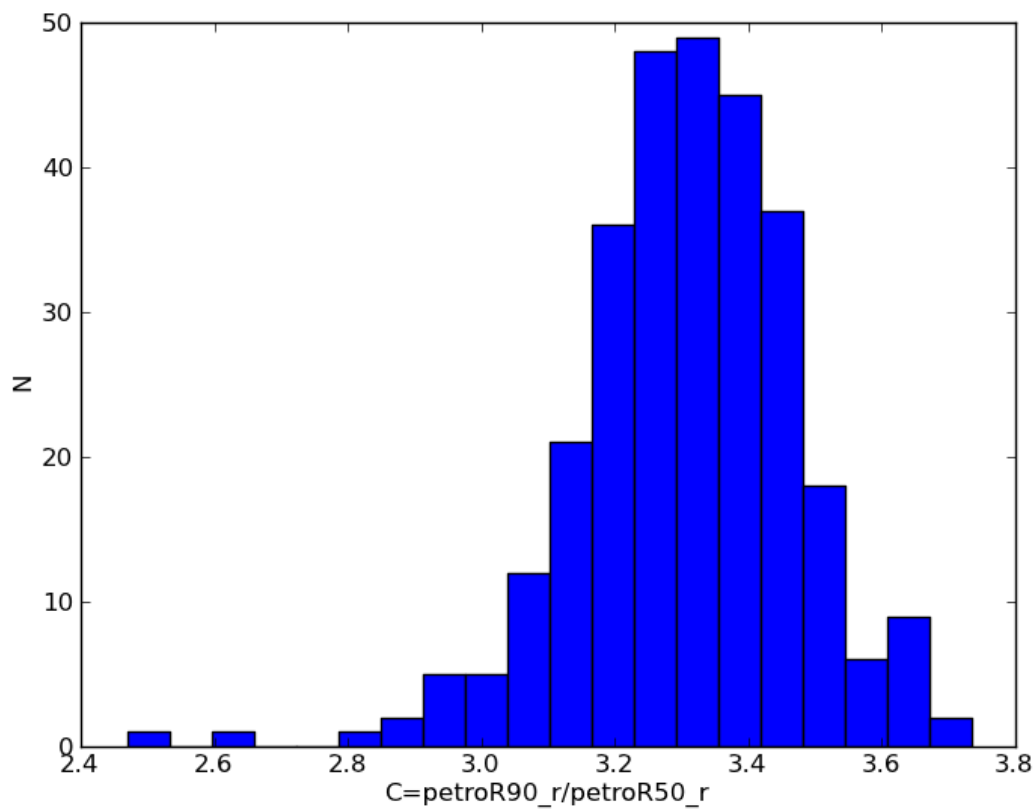


FIGURE 3.28: A histogram of the concentration index $c_r \equiv r_{90}/r_{50}$ values of the observed galaxies in the four highest σ bins from Spiniello et al. (2014). c_r can be related to B/T . The histogram shows that the most of the observed galaxies by Spiniello et al. (2014) have a $c_r > 3.0$ which most likely correspond to a $B/T > 0.5$ but could still be contaminated with some galaxies of $0.2 < B/T < 0.5$ (Cheng et al. 2011).

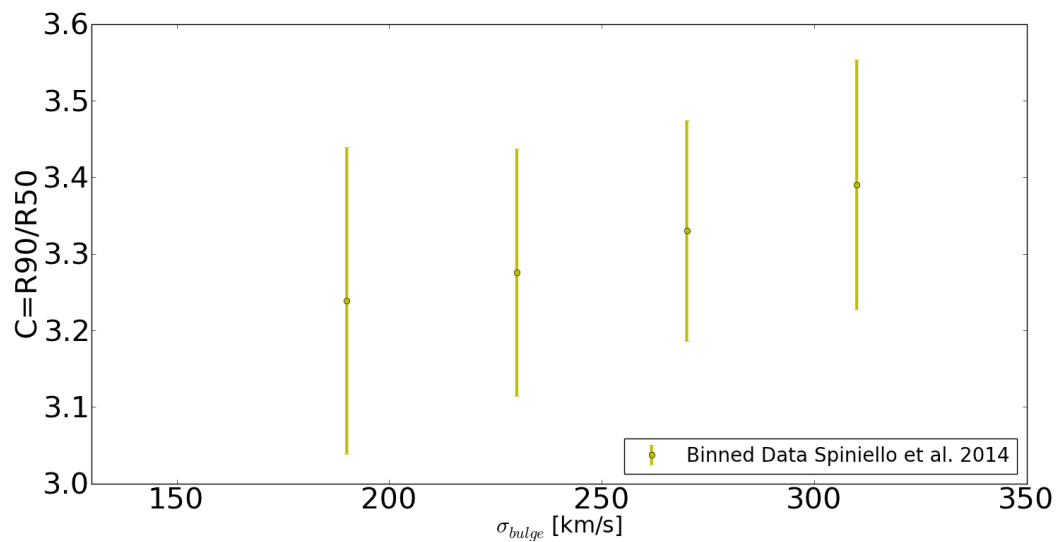


FIGURE 3.29: A binned plot containing the mean and standard deviation of the concentration index $c_r \equiv r_{90}/r_{50}$ values of the observed galaxies in the four highest σ bins from Spiniello et al. (2014). c_r can be related to B/T . This binned plot, like the histogram in Figure 3.28 shows that the most of the observed galaxies by Spiniello et al. (2014) have a $c_r > 3.0$ and that the mean c_r and thus B/T ratio increases with σ .

The histogram and binned plot in Figures 3.28 and 3.29 respectively show that the majority of the concentration indices of the SDSS galaxies selected by Spiniello et al. (2014) lie above 3.0 so are expected to correspond mainly to a $B/T > 0.5$. However, Cheng et al. (2011) found that galaxies selected with $c_r > 2.9$ could contain some galaxies with $0.2 < B/T < 0.5$. We therefore test extending the selection criteria of ETGs in our SAM output down to stellar mass B/T ratio of 0.3 and 0.2 in Figures 3.30 and 3.31. Extending the B/T ratio downward gives a larger spread of a couple of tenths in PDMF slope per bin, with the largest increase in standard deviation in the lowest σ bin. This is because a lower B/T criterion includes more galaxies with a wider variety in morphological (B/T) types and thus a wider variety in (star) formation histories. We choose to continue to the selection criterion $B/T > 0.5$ in the remainder of this thesis unless stated otherwise, as the mean c_r of the Spiniello data lies above 3.2, and well above 2.9, and as decreasing the B/T to 0.2 only changes the PDMF slope by a couple of tenths at most.

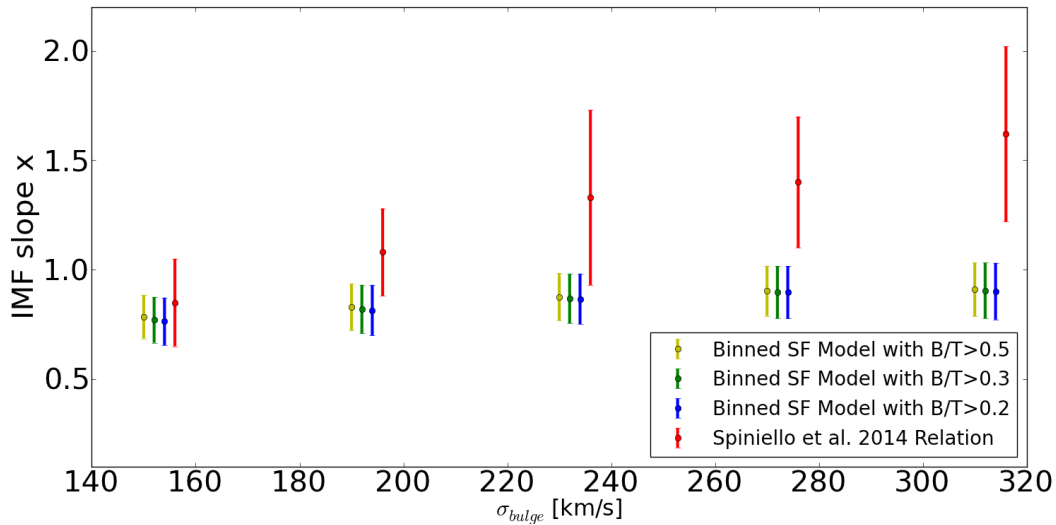


FIGURE 3.30: The binned PDMF slope versus the σ_{bulge} for ETGs in 21 treefiles in the Porter+14 SAM for the SF-IMF model selected with $B/T > 0.2$ (blue), $B/T > 0.3$ (green), and $B/T > 0.5$ (yellow) to check how an extension of our ETG morphological selection criteria will affect the PDMF slope- σ relation. These results are binned in the same five σ bins as the Spiniello et al. (2014) observational data (red) Decreasing the B/T to 0.2 only changes the PDMF slope by a couple of tenths at most.

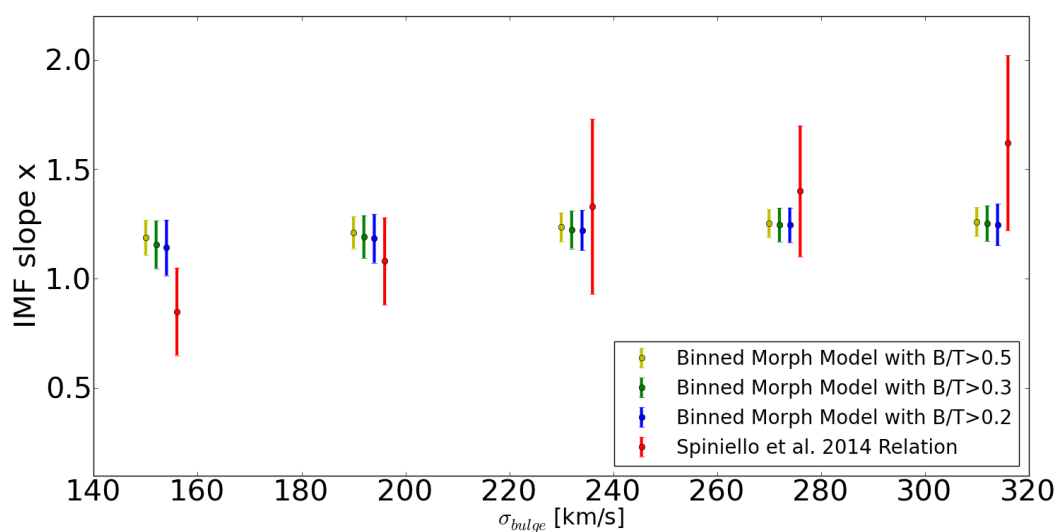


FIGURE 3.31: The binned PDMF slope versus the σ_{bulge} for ETGs in 21 treefiles in the Porter+14 SAM for the Morph-IMF model selected with $B/T > 0.2$ (blue), $B/T > 0.3$ (green), and $B/T > 0.5$ (yellow) to check how an extension of our ETG morphological selection criteria will affect the PDMF slope- σ relation. These results are binned in the same five σ bins as the Spiniello et al. (2014) observational data (red) Decreasing the B/T to 0.2 only changes the PDMF slope by a couple of tenths at most.

3.4 Conclusion and Discussion

We applied the physically motivated SF–IMF model which ties a Salpeter shape to stars formed in bursts and a Chabrier shape to stars formed quiescently in the ETGs to two versions of the ‘Santa Cruz’ SAM, PST14 (see Figure 3.1) and Porter+14 (see Figures 3.20 and 3.22). This SF–IMF model is unable to reproduce the observed low-mass PDMF slope of the most massive ETGs in both versions of the SAM.

Starbursts in the SAMs occur after mergers with mass ratios above 1 : 10 and after gas is moved from the disc to the spheroid to balance disc instabilities in the Porter+14 model. However, burst mode star formation only makes up a small portion of the stellar mass in the large galaxies in our model. The stellar mass contribution through bursts in the high mass galaxies is in most cases still a small fraction of the total stellar mass, as can be seen from Figures 3.4b and 3.4c. Moreover, Robaina et al. (2009) have shown by combining observations and hydrodynamical simulations that less than 10% of star formation between $0.4 \leq z \leq 0.8$ is directly triggered by mergers and instabilities. Therefore the conditions for assigning a Salpeter slope to a stellar population need to be extended beyond stars formed in bursts to steepen the final PDMF slope to the one observed in local ETGs.

We applied the Morph–IMF model which ties the shape of the IMF to the present-day location of stars, either in the disc or bulge, in ETGs from both versions of the SAM, i.e. PST14 (see Figure 3.10) and Porter+14 (see Figures 3.21 and 3.23). The Morph–IMF model is not directly physically motivated but is motivated by the observed IMF slope distinction in discs and bulges of SWELLS galaxies and by the B/D -flux ratio of the galaxies with the steepest slopes from the SF–IMF model. The galaxies with the steepest slope derived from this model were also the ones with the highest B/D ratio which indirectly traces the formation history of the galaxy. We therefore tie a Salpeter shape to stars in the spheroid and a Chabrier shape to stars in the disc of the present-day galaxy ETGs from the SAM. In the high-mass end this method is able to reproduce the observed σ -IMF relation in local ETGs within the error bars of the observational data. In our two models, the present day location of the stars, in either the disc or spheroid, thus has a larger effect on the steepness of the final PDMF slope than the manner in which these stars formed, either in bursts or quiescently. However, as we select ETGs in our model to have a high $B/T > 0.5$ ratio, these galaxies will by selection end up with relatively steep PDMF slopes in the Morph–IMF model.

Bulges in our SAM grow through mergers and subsequent triggered star burst episodes and through the migration of stars and gas from the disc to the bulge and subsequent star burst episodes after disk instabilities in the Porter+14 model. As burst star formation only contributes a fraction of the total stellar component, the Morph–IMF model is more successful due to the formation history of stars currently residing in spheroids of ETGs. Brennan et al. (2015) show that high mass bulge dominated galaxies in the ‘Santa Cruz’ SAM we use often form through at least one major merger ($< 1 : 3$) early on and subsequent multiple minor mergers and disk instabilities which form the dominant spheroidal component. The present-day bulge stars thus most likely formed in discs at higher redshift and moved to the spheroid after a merger or a disk instability to eventually form a current ETG. The higher mass galaxies on average formed their stars earlier than galaxies in the lower-mass bins; see for instance the mass weighted mean age colour coding in Figure 3.21. The process in which more massive galaxies form most of their stars at higher redshifts, galactic downsizing, is observed in red sequence high σ galaxies at low redshifts Nelan et al. (2005) and predicted in massive ETGs in the ‘Santa Cruz’ SAM (Trager and Somerville 2009). The majority of the stars in the bulges of the highest mass galaxies thus most likely formed at high redshift discs in turbulent gas when

average temperature and gas density was higher. The SFR of quiescent mode star formation in the SAM scales with this surface density of cold gas in the disc following Kennicutt (1998) and most of the major merger(s) will have happened early in the lifetime of a currently quiescent spheroid-dominated SAM galaxy following Brennan et al. (2015) so a time dependence of the IMF slope will affect the turn-over mass in both modes of star formation. In Chapter 4 we will therefore investigate the possibility that IMF slope varies with the time at which the stars formed such that the highest mass galaxies with on average the oldest stellar populations will end up with the steepest PDMF slope.

Model III: σ linked to IMF in post-processing and in SAM

In this chapter we test two empirically motivated models that assign (a variation of) the observed σ -IMF slope relation to stars formed in the SAM to further investigate what shapes this relation. We tie a power-law IMF following the observed σ -IMF slope relation to stars formed based on the time at which they formed and the average σ of galaxies in the SAM at that time; the σ - $\langle t \rangle$ -IMF Model which is implemented in post-processing. Next, we tie a power-law IMF following the observed σ -IMF slope relation to stars formed based on the σ of their “host” galaxy at the time of star formation; the σ -IMF model which is implemented within the Porter+14 SAM, although not self-consistently.

4.1 σ - $\langle t \rangle$ -IMF Model

4.1.1 Method

In Chapter 3 we saw that assigning an IMF-shape to stars based on the present-day location of stars was able to reproduce the σ -IMF slope relation in ETGs within the error bars of this relation in the high-mass end. In the low-mass end the model deviated from the observed slope. The high mass galaxies on average formed their stars early on in the universe when the gas was more turbulent than galaxies in lower mass bins. This could indicate that the low-mass IMF slope varies with the redshift at the time stars formed. So instead of using a Chabrier and a Salpeter IMF for different conditions we will now assign a single power-law IMF slope to a set of stars formed that varies with the time at which they formed, the σ - $\langle t \rangle$ -IMF model.

We first apply the σ - $\langle t \rangle$ -IMF model in post-processing (from here on $\langle t \rangle$ -IMF model) to a run of the Porter+14 version of the SAM with the specifications as given Section 3.3.1. We run this SAM for galaxies in 21 subvolumes of $(50\text{Mpc h}^{-1})^3$ of the Bolshoi simulation. The SAM outputs the stars formed in both the bulge and disk per galaxy at a pre-set 195 ages t_{out} from $13.75 - 0$ Gyr in 25 metallicity bins. We get the total stellar mass per age by adding the stars formed in both the bulge and the disk in each bin. We only do this for the galaxies filtered on ETG properties so central galaxies with $\log(M_*/M_\odot) > 9.5$, $150 \leq \sigma \text{ [km s}^{-1}] \leq 310$,

$SFR < 0.3 M_{\odot} \text{yr}^{-1}$ and $B/T > 0.2$ (instead of $B/T > 0.5$ as in Section 3.3 though it only make a slight difference as can be seen in Figure 3.31).

I We know the relation between IMF slope and σ from the Spiniello relation

$$x = 2.3 \log(\sigma_{200}) + 1.13 \quad (4.1)$$

II We know the mass weighted mean age $\langle t \rangle$ and σ of each $z = 0$ galaxy from the SAM.

By combining the observed relation with these two galaxy properties from the SAM we get the $\log\langle t \rangle$ - x relation in Figure 4.1. The IMF slope on the x-axis is found by plugging the σ of the galaxies found from the SAM into the Spiniello relation from Equation (4.1). The y-axis is the corresponding mean age of these galaxies.

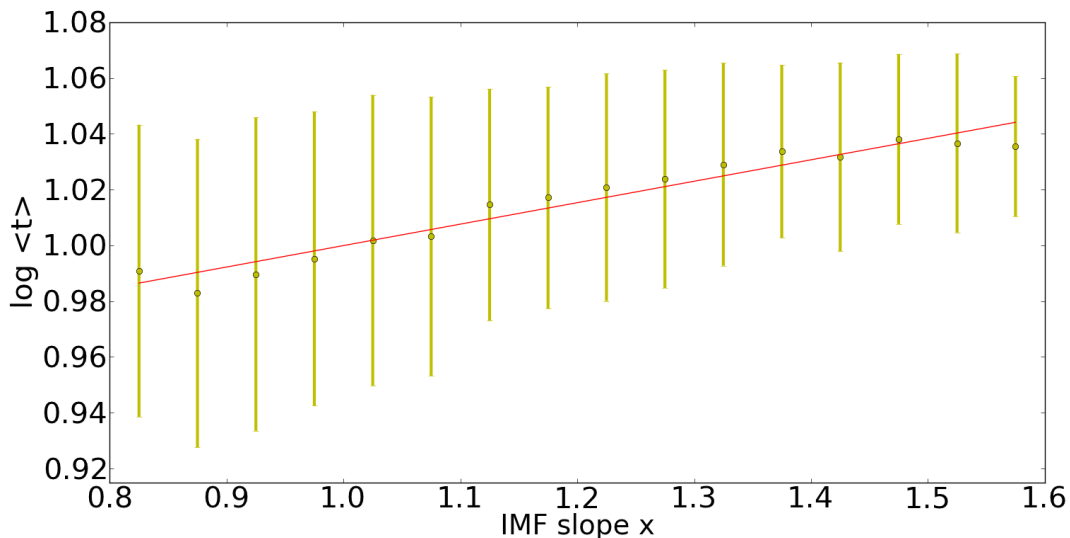


FIGURE 4.1: The $\log\langle t \rangle$ - x relation for ETGs in found by combining the $\langle t \rangle$ - σ relation found from the properties of the galaxies in the SAM and the observed σ - x relation from (Spiniello et al. 2014). The linear fit to the mean of his relation in each bin will be used as to assign a slope x to the stars formed per output age t_{out} for galaxies in the SAM.

We bin the IMF slopes into bins with left and right most edge in the range $0.8 - 1.6$ with a width of 0.05 , giving 16 bin centers. We apply a linear fit $y = a + b x$ to the mean in each bin (red line in Figure 4.1). This gives us an expression to relate $\langle t \rangle$ to x :

$$\log\langle t \rangle = a + b x \quad (4.2)$$

where the fit gives $a = 0.0768$ and $b = 0.923$

We can use this relation to find the x corresponding to each of the 195 output ages t_{out} :

$$t_{out} = 0.0768 + 0.923 x \quad (4.3)$$

The t_{out} - x relation we get from the fit in Figure 4.1 is only based on a small range of $\log\langle t \rangle$ and corresponding x as we selected ETGs from the SAM that were used to make this fit that

have by nature a relatively high mean age that does not cover the entire possible age spectrum. We therefore choose to fix Equation 4.4 below $x = 0.8$ such that $\log(t_{out})(x < 0.8) = 0.985$. The relation in Equation 4.3 then becomes

$$t_{out} = \begin{cases} 0.0768 + 0.923 x & \text{if } x \geq 0.8 \\ 0.985 & \text{if } x < 0.8 \end{cases} \quad (4.4)$$

We know how many stars were formed per galaxy for 195 different ages. For each of these ages we have the power-law slope x with which they formed using Equation 4.4. For each of these ages with corresponding x we can now determine the the fraction of stellar mass in each mass bin, $[i]$ from $0.1 - 0.8 M_{\odot}$ as described in Section 2.2.4. For each x , so at each t_{out} , we determine the corresponding fractional stellar mass array f_{tx} using

$$f_{tx} [i] = \frac{C}{1-x} (\text{bins}[i]^{1-x} - \text{bins}[i+1]^{1-x}) \quad (4.5)$$

where the normalisation constant C is determined for each x following

$$C = \frac{1-x}{M_l^{1-x} - M_u^{1-x}} \quad (4.6)$$

We now have at each output age t_{out} an array which represent the normalised fraction of mass in stars in the range $0.1 - 0.8 M_{\odot}$ for the power-law slope x corresponding to that t_{out} . For each selected ETG we know the amount of stars $\Delta m_{*,t}$ that formed between two output ages. These stellar masses are output without taking into account stellar mass loss due to massive stars as is done in the rest of the SAM. So we multiply the mass of the stars formed in each time step with $(1 - f_{recycle})$, where $f_{recycle} = 0.43$, to determine the fraction of mass in stars at each time step that is left today. Now for each galaxy we can additively populate the PDMF array at each of the 195 time steps using:

$$PDMF_1[N] = \sum_{t=13.75}^{t=0} \Delta m_{*,t} (1 - f_{recycle}) f_{tx}[N]_t \quad (4.7)$$

which is normalised and put in the right format at $t = 0$ using

$$PDMF[N] = \frac{PDMF_1[N]}{m_{*,tot} dm_{*} \text{-bins}[N]} \quad (4.8)$$

where

$$m_{*,tot} = \sum_{t=13.75}^{t=0} \Delta m_{*,t} (1 - f_{recycle}) \quad (4.9)$$

For each galaxy a linear fit is applied to the log of this $PDMF[N]$ as described in Section 2.3, which gives us the σ - x relation for the model galaxies at $z = 0$.

4.1.2 Results

The σ -PDMF slope relation from the $\langle t \rangle$ -IMF model for the ETGs of the SAM is shown in Figure 4.2. In Figure 4.3 we bin these results as before following Table 3.1 to best compare them with the observed Spiniello relation.

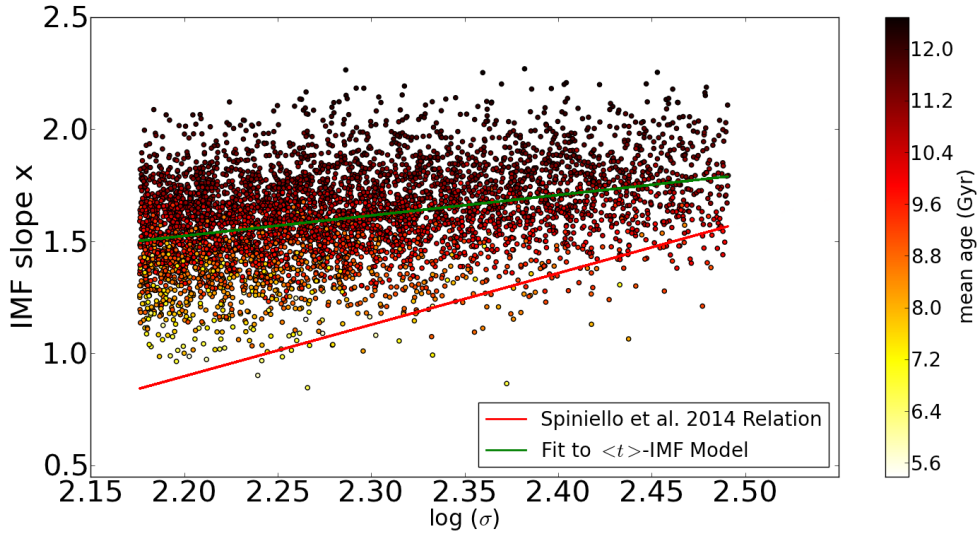


FIGURE 4.2: The σ -PDMF slope relation from the $\langle t \rangle$ -IMF model for the ETGs in the Porter+14 SAM. This model assigns a power-law slope to a set of stars based on the $\langle t \rangle$ and σ at which they formed. The red line is the observed σ -IMF slope relation from Spiniello et al. (2014) and the green line is a linear fit to the PDMF slope of the model galaxies. This model is able to reproduce some gradient in IMF slope with increasing σ but it does not fully reproduce the offset or steepness of the observed relation, especially for the lower σ galaxies.

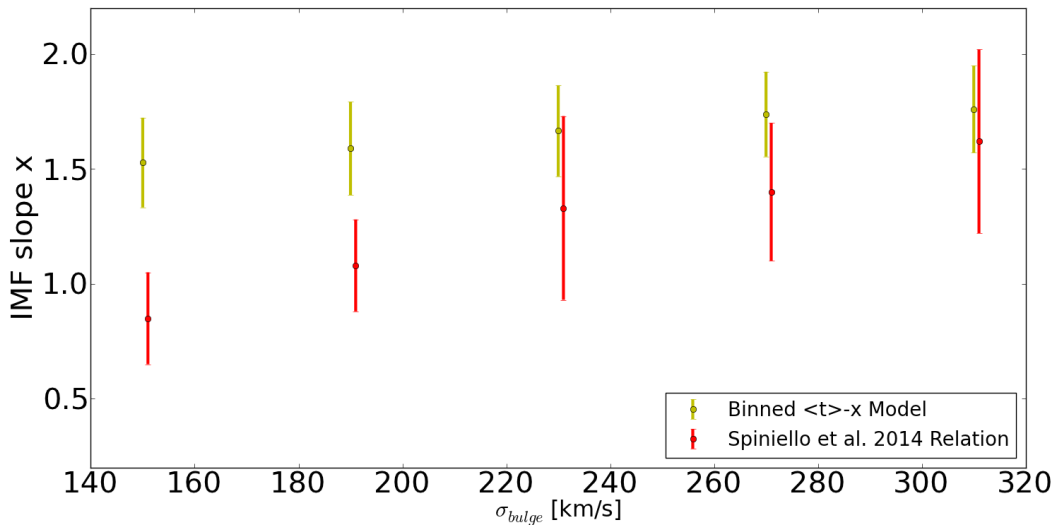


FIGURE 4.3: The binned σ -PDMF slope relation from the $\langle t \rangle$ -IMF model for the ETGs in the Porter+14 SAM. This model assigns a power-law slope to a set of stars based on the $\langle t \rangle$ and σ at which they formed. This method is only able to reproduce the observed relation in the highest σ bin. In the lower σ bins the final PDMF slope is higher than the errorbars of the observed relation.

This method is only able to reproduce the observed relation in the highest σ bin. In the lower σ bins the final PDMF slope is higher than the (errorbars of) the observed relation. The IMF we assign to stars formed at each t thus appears to be too high. We will therefore test how using the top of the scatter in the $\log\langle t \rangle - x$ relation as an input IMF slope will affect the results. A fit to this upper limit will provide an input power-law IMF with a lower slope x at a higher $\langle t \rangle$ than when the same fit is applied to the mean which should bring the final PDMF slope down as well.

We determine the $\log\langle t \rangle - x$ relation from Equation 4.2 for the upper limit of the scatter in the $\log\langle t \rangle - x$ plot. We do the same for the lower limit of the scatter for comparison. We therefore fit the mean plus the standard deviation and the mean minus the standard deviation, so the upper and lower limits of the error bars in Figure 4.1, to get the two corresponding relations for $t_{out} - x$. We apply the same routine as before to determine the PDMF slope- σ relation at $z = 0$. The resulting PDMF slope- σ relation for the input IMF determined from the mean plus the standard deviation is presented in Figures 4.4 and 4.5 and for the mean minus the standard deviation in Figures 4.6 and 4.7.

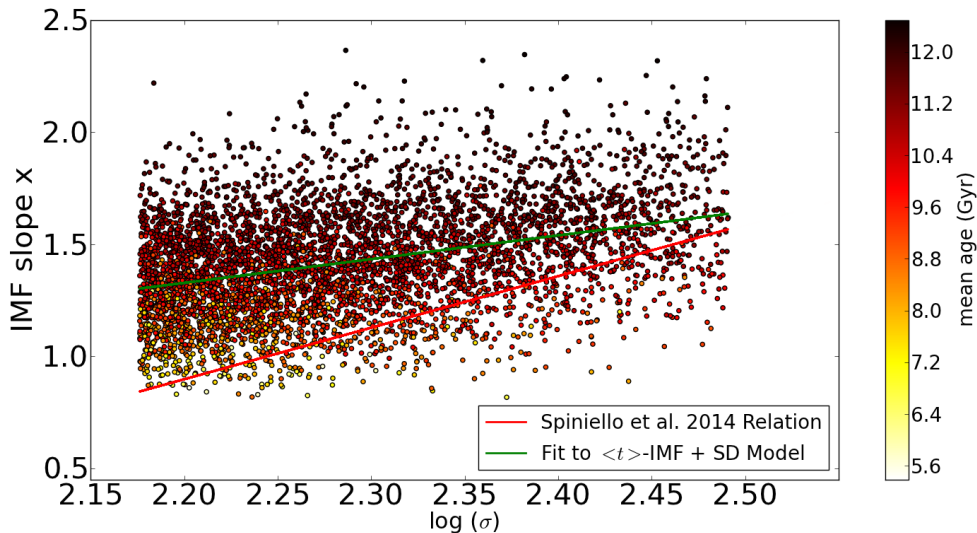


FIGURE 4.4: The σ -PDMF slope relation from the $\langle t \rangle$ -IMF model for the ETGs in the Porter+14 SAM, using an input IMF determined from the mean plus the standard deviation of the $\langle t \rangle - x$ relation. The red line is the observed σ -IMF slope relation from Spiniello et al. (2014) and the green line is a linear fit to the PDMF slope of the model galaxies. This input relation brings the overall σ -IMF slope relation from the model down such that it fits the offset, although not fully the steepness, of the observed relation better.

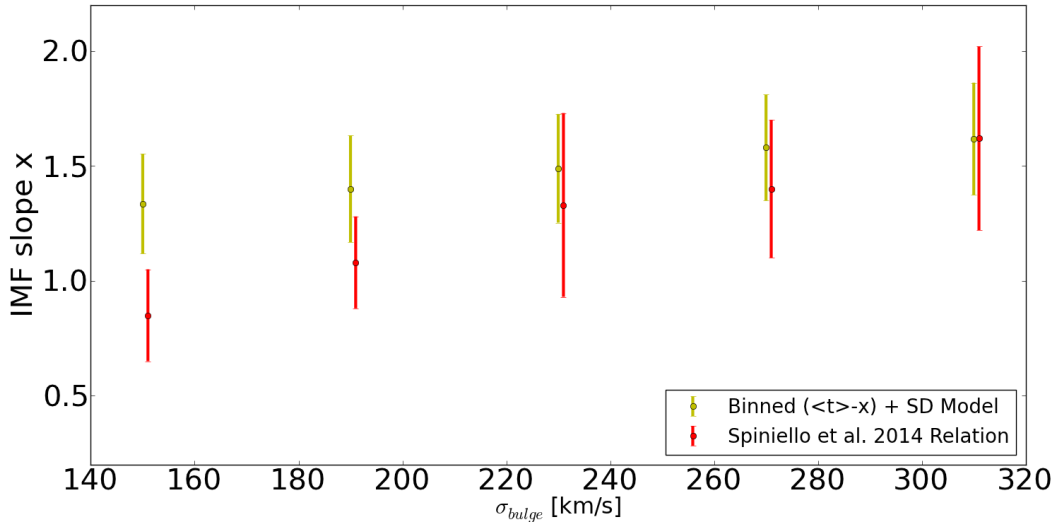


FIGURE 4.5: The binned σ -PDMF slope relation from the $\langle t \rangle$ -IMF model for the ETGs in the Porter+14 SAM with the mean plus the standard deviation of the $\langle t \rangle$ - x relation as input t_{out} - x relation. This model reproduces the observed slope in the high σ bins well, and comes closer to the slope in the low σ bins than when using the mean of the $\log \langle t \rangle$ - x relation as an input IMF but it does not yet reproduce the correct slope in these lower mass bins.

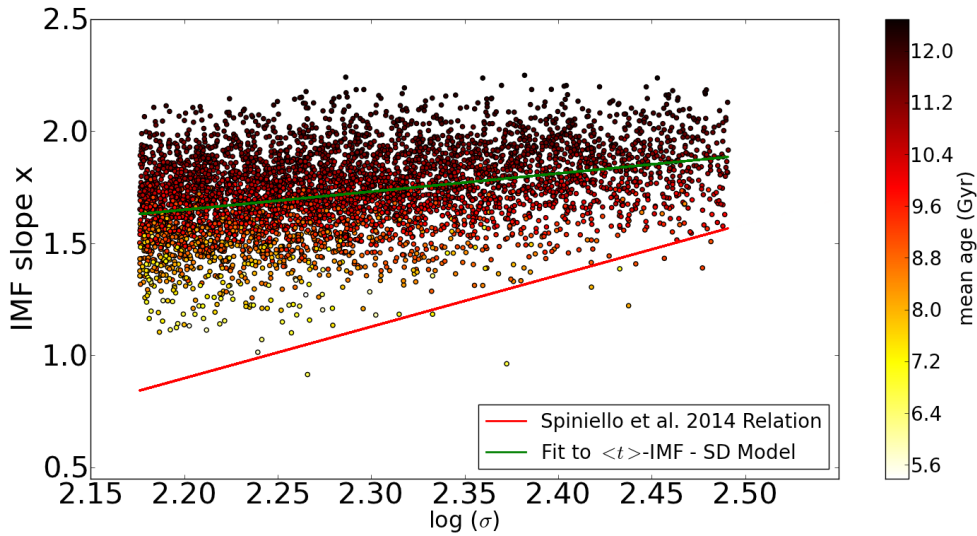


FIGURE 4.6: The σ -PDMF slope relation from the $\langle t \rangle$ -IMF model for the ETGs in the Porter+14 SAM, using an input IMF determined from the mean minus the standard deviation of the $\langle t \rangle$ - x relation. The red line is the observed σ -IMF slope relation from Spiniello et al. (2014) and the green line is a linear fit to the PDMF slope of the model galaxies. To illustrate how a change in input t_{out} - x relation in this model affects the PDMF slope. As expected a higher input power-law slope at a lower $\langle t \rangle$ increases the resulting PDMF to steeper than the observed values per σ of the galaxy.

This method of varying the slope if the IMF assigned to a set of stars with the time at which they formed is only able to reproduce the observed relation in the high mass end when using the mean of the $\log \langle t \rangle$ - x relation as an input IMF (see Figure 4.3). Using the upper limits of the error bars (see Figure 4.5 as input IMF brings the PDMF slope down over the entire σ

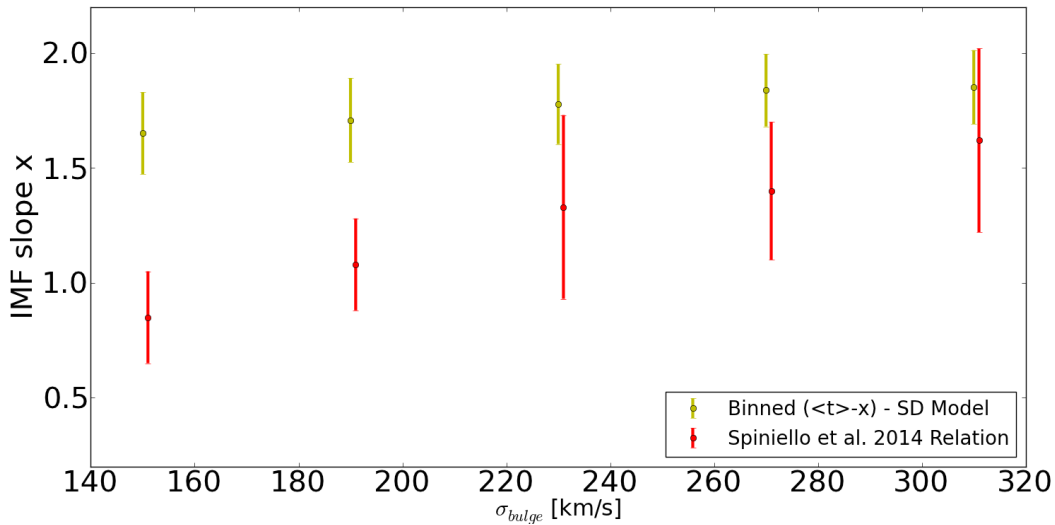


FIGURE 4.7: The binned σ -PDMF slope relation from the $\langle t \rangle$ -IMF model for the ETGs in the Porter+14 SAM with the mean minus the standard deviation of the $\langle t \rangle$ - x relation as input t_{out} - x relation. As expected a higher input power-law slope at a lower $\langle t \rangle$ increases the resulting PDMF to steeper than the observed values per σ bin.

range and is therefore also able to reproduce the observed relation in the intermediate σ bins as well. However, like the Morph-IMF model, neither implementation of the $\langle t \rangle$ -IMF model reproduces the observed IMF slope for the lower mass galaxies in the lower σ bins.

4.2 σ -IMF Model in SAM

The SF-IMF model is only able to reproduce the low end of the observed σ - x relation, the Morph-IMF Model the high and intermediate relation, and the $\langle t \rangle$ -IMF model only the intermediate bins. However, none of these models is able to reproduce the steepness of the Spiniello relation over full σ range. One of the problems in reproducing the slope for lower mass galaxies is that these have varying assembly and star formation histories, whereas higher mass galaxies have fewer options for potential formation histories. By construction, the $\langle t \rangle$ -IMF model is not able to apply a varying IMF slope over the entire history of the galaxies in the SAM in post-processing; The selected ETGs that were used to relate $\langle t \rangle$ to σ and then to the power-law slope by nature all have a relatively high mean age that does not cover the entire possible age spectrum and all time steps. We chose to truncate the assigned slope below the lowest mean age in the sample. We will therefore now apply a variation of this model within the SAM which can directly relate the σ of the galaxy to a power-law IMF slope at all time step when stars are formed.

We now let the IMF slope vary with the σ_* of the galaxy at the time that the stars formed within the SAM, instead of in post-processing as before, and additively populate the low-mass PDMF of the eventual present-day ETGs. This method takes into account the formation histories of the present day ETGs we look at and indirectly also the time at which the stars formed as most of the lower σ galaxies which eventually merged to form ETGs formed early in the universe.

4.2.1 Method

We populate the low-mass PDMF with a power-law IMF at each time step stars are formed in the SAM. This IMF power-law coefficient depends on the σ of the galaxy at the time the stars are formed and is determined by an input σ - x relation. Each time stars are formed the normalised fractional mass array corresponding to the IMF power-law coefficient x is computed and the stars are added to the galaxy's PDMF array following this IMF. The slope of the final PDMF of each central (early type) galaxy at $z = 0$ is then determined in post-processing. Below we describe briefly how this PDMF routine is implemented in the Porter+14 SAM (for more details on the general method, see Chapter 2).

In the parameter file, that sets up the necessary variables and other input information for the SAM, we provide the following information to execute the σ -IMF model :

I a relation between σ and IMF slope x :

$$x = -(a \times \sigma_{200} + b) \quad (4.10)$$

II the number N of stellar mass bins and the mass range $m_{low} - m_{up}M_{\odot}$, to compute an array logarithmically-spaced stellar mass bins; and

III the mass range $M_{low} - M_{up}M_{\odot}$ over which the IMF should be normalised

We use the following values, although these values can be changed for each new run of the SAM if needed:

I the Spiniello et al. (2014) relation, where $a = 2.3$ and $b = 1.13$ in Equation 4.10.

II $N=24$ stellar mass bins and the mass range $0.1 - 1.0 M_{\odot}$

III the normalisation mass range $0.1 - 120 M_{\odot}$

This implemented in the parameter file in the following way:

```
#pdmf routins bin generation (added by Judith 19-11-2014)
#compute_pdmf 0=off 1=on
1
#Mnormlow_pdmf Mnormup_pdmf binlow_pdmf binup_pdmf BINNR_PDMF
0.1 120 0.1 1.0 24
# imf slope x= -1*(a * sigma + b): a_slope b_slope
2.3 1.13
```

In the file which provides member functions for the halo and galaxy classes, `haloclass.cc`, we use these parameters to:

IV generate $bins_{imf}[N + 1]$: an array that contains the edges of the logarithmically-spaced stellar mass bins;

V initialise $bins_{salp}[N]$: an array which will give the fraction of stars in each stellar mass bin following a power-law slope dependent on the σ of the galaxy and the input σ - x relation. This will be computed per galaxy at each time step stars are formed in `stars.cc`, the file of the SAM that adds the baryonic physics to the DM merger trees and forms and tracks the luminous galaxies.

VI initialise $bins_{pdmf}[N]$: an array that will be populated additively per galaxy each time stars are formed following the fractional mass array. This is done in stars.cc as well.

This is implemented in haloclass.cc as follows:

```

//added by Judith ter Horst 19-11-2014
//setting the arrays for the PDMF routine
bins_imf = NULL; // mass bins
bins_pdmf = NULL; //PDMF bins
bins_fsalp = NULL; //fractional mass array dependent on sigma-slope relation
if (compute_pdmf) {
//generate mass bins used in PDMF routine with lower and upper edge and number of bins given in param file
bins_imf = new double[BINNR_PDMF+1];
double stepsize= (log10(binup_pdmf)-log10(binlow_pdmf))/BINNR_PDMF;
for (int n=BINNR_PDMF; n >= 0; --n){
bins_imf[n]=pow(10,(log10(binup_pdmf)-n*stepsize));
}
bins_pdmf = new double[BINNR_PDMF];
bins_fsalp = new double[BINNR_PDMF];
// initialising the PDMF bins for each galaxy, they will be populated in stars.cc
for (int m=BINNR_PDMF; m > 0; --m){
bins_pdmf[m] = 0.0;
bins_fsalp[m] = 0.0;
}
}
}

```

We determine the normalised fractional mass array $bins_{fsalp}[N]$ and populate the PDMF $bins_{pdmf}[N]$ in stars.cc. This part of the SAM that implements the recipes for baryonic physics and at each time step computes and updates the properties of all the galaxies that are being followed for each galaxy individually. These properties are linked to the current (central) galaxy being followed in the loop via `g->property`. From the Porter+14 model we know the σ of each central galaxy at any timestep. We also know the stars that formed in each galaxy at that time step. We then implement the central part of the σ - x model at each time step for each of the central galaxies as follows:

VII We know the σ of the galaxy $g \rightarrow \sigma$ and we have an input σ - x relation, Equation 4.10, defined in the parameter file. Combining these determines the power-law IMF slope we re-assign to the stars formed in that galaxy at that time step:

$$x = -1 \times (a \times (\log 10(g \rightarrow \sigma_{bulge}) - \log 10(200)) + b) \quad (4.11)$$

VIII We then determine the normalisation constant C corresponding to the power-law IMF with the computed slope x

$$C = \frac{1 - x}{M_{low}^{1-x} - M_{up}^{1-x}} \quad (4.12)$$

IX We now compute the fractional mass in each of the mass bins of `g->bins_imf[N + 1]` from $m_{low} - m_{up} M_{\odot} = 0.1 - 1.0 M_{dot}$ per galaxy for the specific slope x and corresponding normalisation constant C , for the indices $m = N = 24$ up until $m = 1$:

$$g \rightarrow bins_{fsalp}[m] = -\frac{C}{x + 1} (g \rightarrow bins_{imf}[m]^{1-x} - bins_{imf}[m - 1]^{1-x}) \quad (4.13)$$

X The PDMF $g \rightarrow bins_{pdmf}$ with the same mass bins $0.1 - 1.0 M_{\odot}$ can now be populated using the fractional mass array `g->bins_fsalp` corresponding to the power-law slope x and the amount of stars formed in this galaxy at this time step. This happens additively for each central galaxy over all the time steps.

$$g \rightarrow \text{bins}_{\text{pdmf}}[m] + = g \rightarrow \text{bins}_{\text{fsalp}}[m] * (dm_{*,\text{norm}} + dm_{*,\text{burst}}) * (1.0 - f_{\text{recycle}}); \quad (4.14)$$

This is implemented in stars.cc as follows:

```

if (compute_pdmf){
  for (int m=BINNR_PDMF; m > 0; --m){
    g->bins_fsalp[m] = 0.0; //fractional array that gives the fractions of mass in each mass bin
    // for specific slope is set to zero at each galaxy
    // and time iteration

    double x_slope= 0.0; // IMF slope
    double C= 0.0; //Salpeter normalisation constant

    // link the slope x in Salpeter like IMF ksi(M) /propto M^x to the current timestep's and galaxy's sigma
    //following the sigma-x relation from the param file (a_slope and b_slope)
    x_slope= -1. * (a_slope * (log10(g->sigma_bulge)-log10(200)) + b_slope);

    // to determine normalisation constant of the specific IMF form
    C=(-1.0*(x_slope + 1.0))/ (pow(Mnormlow_pdmf, x_slope+1.0) - pow(Mnormup_pdmf, x_slope+1.0));

    for (int m=BINNR_PDMF; m > 0; --m){
      //populating the Salpeter like fractional array using the specific slope x and normalisation constant C
      //Uses the edges of the mass bins (imf_bins) as limits in the integral of the corresponding IMF function to
      //populate the fractions.
      g->bins_fsalp [m]=-C/(x_slope+1.0) *(pow(g->bins_imf [m], x_slope+1.0)-pow(g->bins_imf [m-1], x_slope+1.0));

      // populating PDMF array additively per galaxy with mass in stars formed (and still remaining) times the
      //fractional mass array.
      g->bins_pdmf [m]+=g->bins_fsalp [m]* (dm_star_norm+dm_star_burst)* (1.0 - f_recycle);
    }
  }
}

```

The PDMF of each galaxy outputted at $z = 0$ per central galaxy in a separate file, pdmf.dat, along with the galaxy and halo id and some typical galaxy properties such as total stellar mass and velocity dispersion. Before the PDMF of each galaxy is outputted at $z = 0$ we divide $\text{bins}_{\text{pdmf}}$ by the dm in each mass bin to end up with $\xi(m)$ rather than $\xi(m) dm$. We do not divide the *PDMF* by the total stellar mass in each galaxy as described in 3.2.2 as this will only affect the offset of the *PDMF* relation and not the slope which is what we are interested in. In post-processing we fit this *PDMF* of each galaxy using a linear fit as described in 2.3 to determine the slope x of the PDMF.

4.2.2 Results

4.2.2.1 Spiniello Relation as Input σ - x Relation

We first implement this σ -IMF model with the observed Spiniello et al. (2014) relation (from here on the Spiniello relation) as input IMF relation in Equation 4.10 to test if and how we should change the input σ - x relation in our model to end up with the observed relation. We run the Porter+14 SAM with the PDMF routine addition described in Section 4.2.1 for subvolumes of $(50\text{Mpc h}^{-1})^3$ of the Bolshoi simulation with the specifications in 3.3.1.

Figure 4.8 shows the fit (black dashed line) to the PDMF (red line) of one galaxy with $\log(\sigma) \approx 2.35$, one of the intermediate galaxies within our σ -range. The slope of this fit is can be plotted against typical properties of the galaxy, stellar mass and velocity dispersion. This is done for all the selected ETGs from the sample. The resulting m_* - x and σ - x relations are presented in Figures 4.9 and 4.10 for ETGs selected as central galaxies with with $\log(M_*/M_\odot) > 9.5$, $150 \leq \sigma [\text{kms}^{-1}] \leq 310$, $SFR < 0.3 M_\odot \text{yr}^{-1}$ and $B/T > 0.5$. We bin these results following Table 3.1 and determine the mean value and standard deviation in each bin in Figure 4.11.

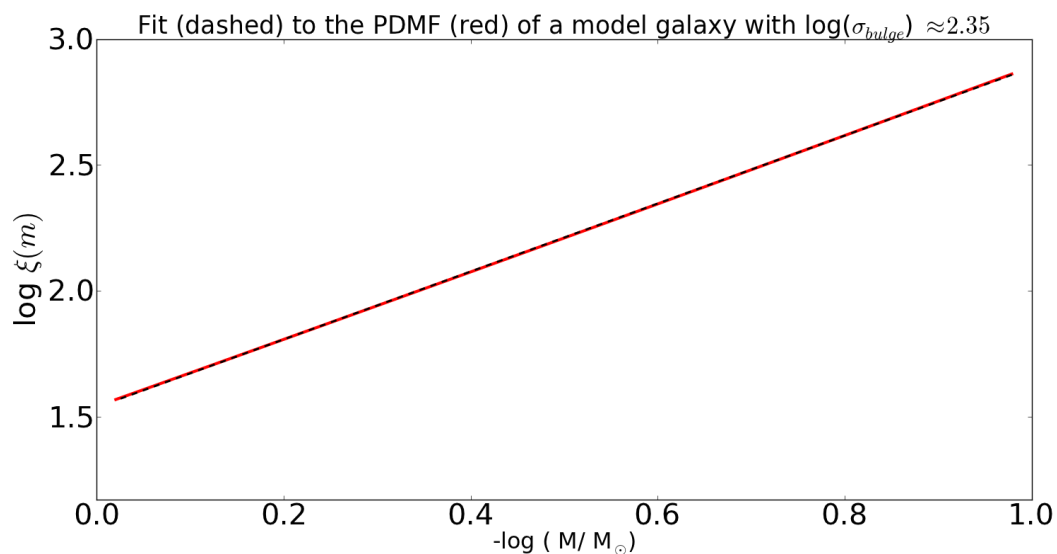


FIGURE 4.8: A fit (black dashed line) to the PDMF (red line) of one galaxy with $\log(\sigma) \approx 2.35$ from the σ -IMF model which assigns a power-law IMF slope to stars formed within the SAM following a σ - x relation and the σ of the galaxy at the time the stars were formed, to illustrate what the PDMF of a model galaxy, in the intermediate σ bin, looks like.

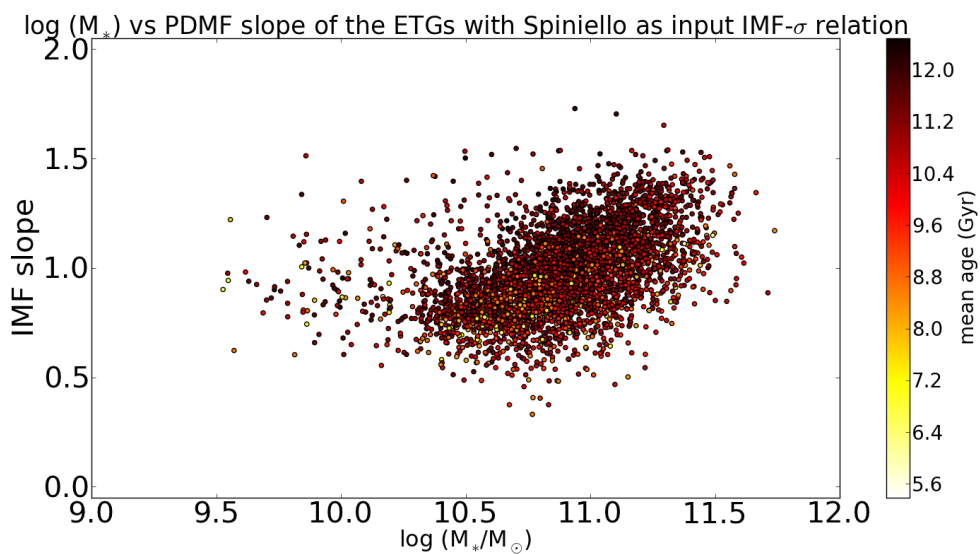


FIGURE 4.9: The M_* -IMF slope relation for ETGs in the Porter+14 SAM for the σ -IMF model, which assigns a power-law IMF slope to stars formed within the SAM following the observed Spiniello et al. (2014) σ - x relation and the σ of the galaxy at the time the stars were formed. The the highest mass galaxies have the steepest IMF slopes.

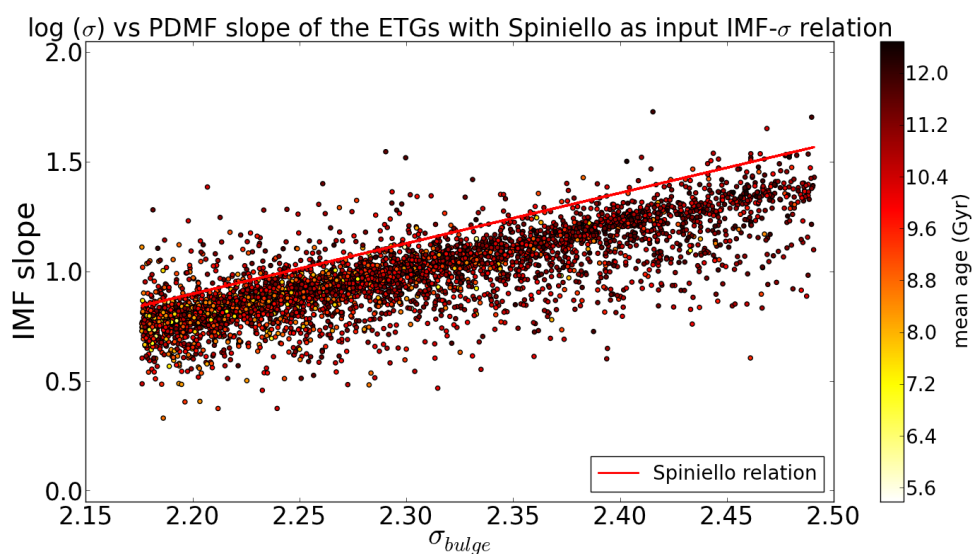


FIGURE 4.10: The σ -IMF slope relation for ETGs in the Porter+14 SAM for the σ -IMF model with the observed Spiniello et al. (2014) as input σ - x relation (red line). The PDMF slope of the ETGs from the model reproduces the steepness of the observed relation but lies below the observed slope values. The input σ - x relation serves as the upper limit for the slope of the majority of the galaxies as most of the stars of a particular galaxy were not formed when that galaxy had reached its present day size. By drawing a horizontal line at a fixed IMF slope between the input relation and the model points, we can estimate at which σ most of the stars formed that contribute to the slope of particular present day σ -galaxy.

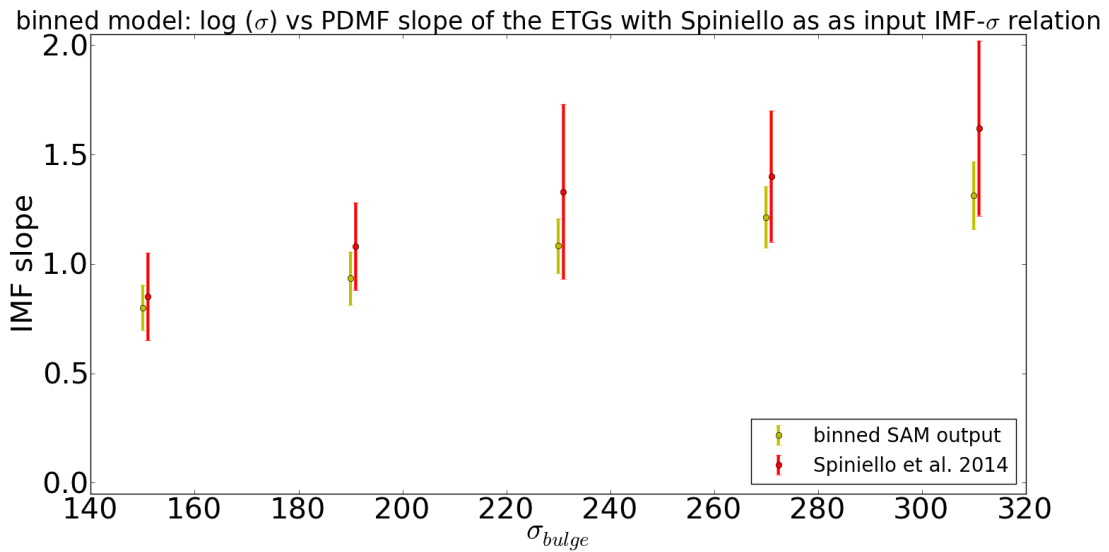


FIGURE 4.11: The binned σ -IMF slope relation for ETGs in the Porter+14 SAM for the σ -IMF mode with the observed Spiniello et al. (2014) as input σ - x relation. The binned model data is shown in yellow and the observational data from Spiniello et al. (2014) in red. The σ - x model is able to reproduce the steepness of the observed relation over the entire σ range, though not fully the offset of the observational slope.

From Figures 4.10 and 4.11 we see that σ - x model is able to reproduce the steepness of the observed relation over the entire σ range, though not fully the offset of the observational slope. The red line in Figure 4.10 is the input σ - x relation, the Spiniello et al. (2014) relation from observations. The input relation serves as the upper limit for the slope of the majority of the galaxies as most of the stars of a particular galaxy were not formed when that galaxy had reached its present day size. These stars formed in lower mass galaxy which ended up in the present-day ETG and were thus re-assigned an IMF with a lower slope than if they would have formed in the galaxy with the present-day σ . We can estimate at which σ most of the stars formed that contribute to the slope of particular present day σ -galaxy formed by drawing a horizontal line at a fixed IMF slope between the input relation and the model points.

In the SF-IMF, Morph-IMF, and $\langle t \rangle$ -IMF models we populate and determine the PDMF slope for the stellar mass bins from $0.1 - 0.8 M_{odot}$. However, the upper limit for which solar metallicity stars have not moved off the MS in 10 Gyrs is $1.0 M_{\odot}$ as explained in section 2.2.1. We therefore apply the σ -IMF model to stellar mass bins extended to this upper limit of $1.0 M_{\odot}$ which results in Figures 4.9, 4.10 and 4.11. Figure 4.12 shows the results of the PDMF routine with the exact same specifications except one run with stellar mass bins from $0.1 - 0.8 M_{\odot}$ and one with the bins in the range $0.1 - 1.0 M_{\odot}$. Extending the mass range of the stellar mass bins for which the PDMF slope is determined only makes a minute difference in slope; the mean difference is 0.003.

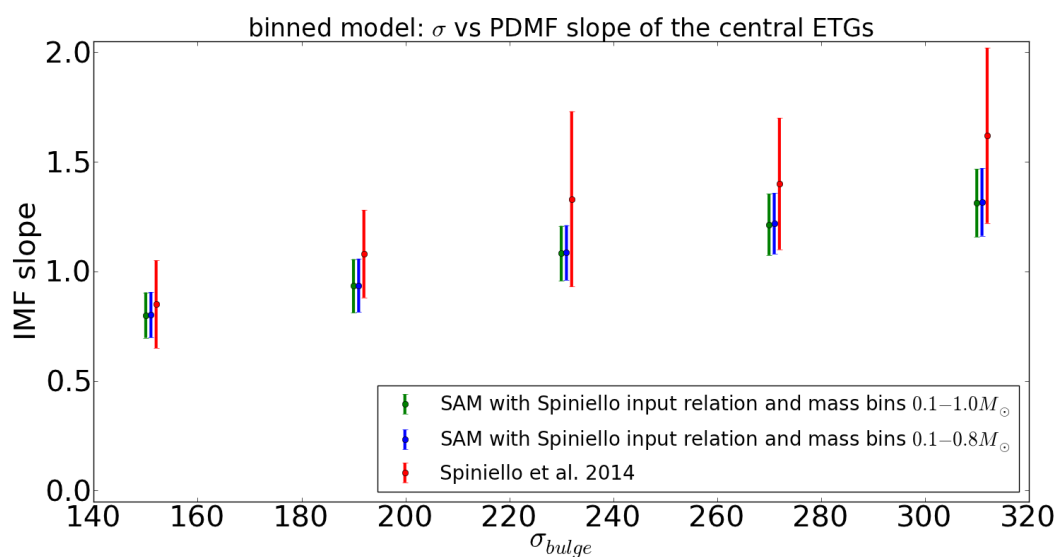


FIGURE 4.12: The σ -IMF model with the low-mass IMF ranging $0.1 - 0.8 M_{\odot}$, which has been used in the SF-IMF, Morph-IMF, and $\langle t \rangle$ -IMF models and $0.1 - 1.0 M_{\odot}$, which has been used in the σ -IMF model. An increase in the upper mass limit for which stars have not yet moved off the MS such that we can equate their observed IMF with the PDMF, only affects the final PDMF slope in our models by a couple of hundreds at most. We therefore do not change the upper mass limit of the low-mass IMF in the other models in this thesis.

4.2.2.2 Spiniello + 0.15 Relation as Input σ - x Relation

We change the offset of the input σ - x relation from Equation 4.10 by 0.15 such that $a = 2.3$ and $b = 1.28$, which is approximately the amount that the observed relation needs to be shifted to better fit the mean of the σ bins. When applied to the SAM with the exact same specifications as before this leads to Figures 4.13, 4.14 and 4.15.

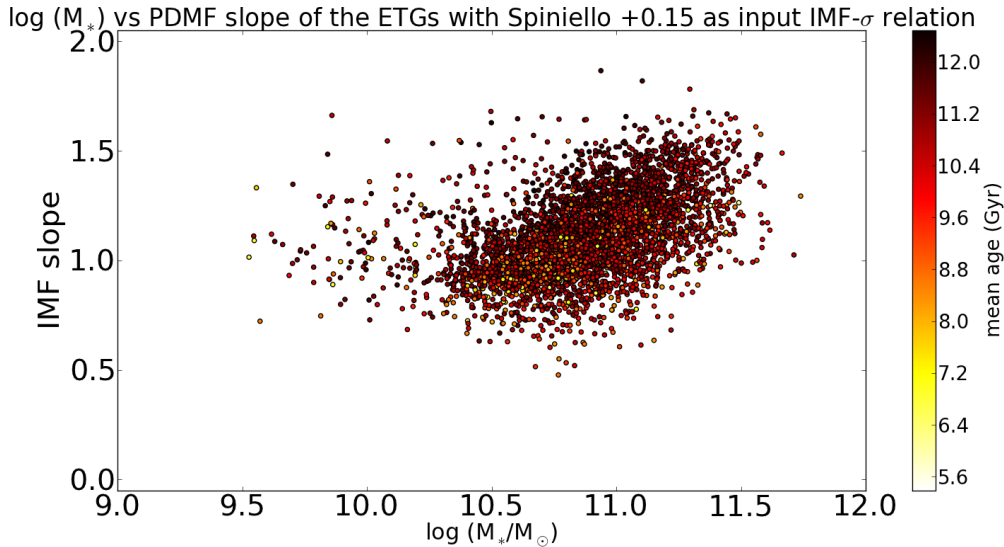


FIGURE 4.13: The M_* -IMF slope relation for ETGs in the Porter+14 SAM for the σ -IMF model with the observed Spiniello et al. (2014) +0.15 as input σ - x relation. The overall PDMF slope at each galaxy mass is higher than when Spiniello et al. (2014) was used as input σ - x relation

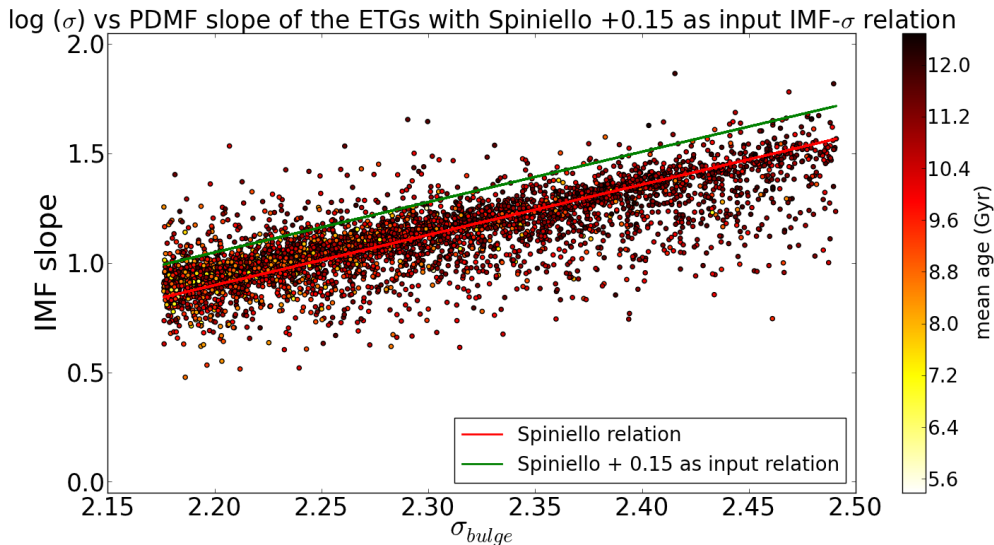


FIGURE 4.14: The σ -IMF slope relation for ETGs in the Porter+14 SAM for the σ -IMF model with the observed Spiniello et al. (2014) +0.15 as input σ - x relation (green line), to be compared with the Spiniello et al. (2014) relation (red line). This model is able to reproduce both the steepness and the offset, so height, of the observed σ -IMF slope relation over the entire σ range of ETGs considered.

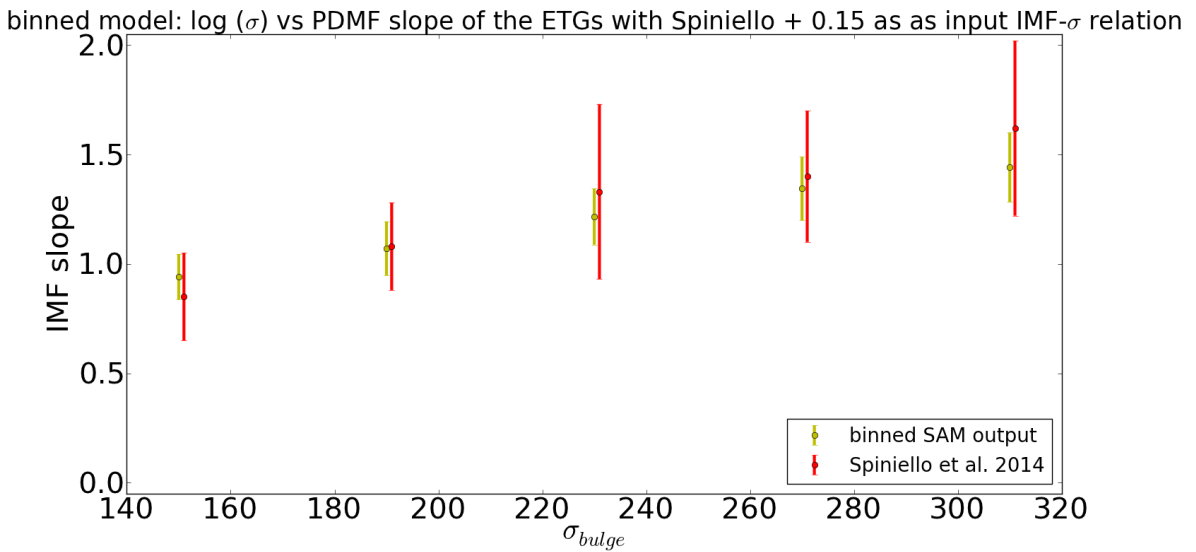


FIGURE 4.15: The binned σ -IMF slope relation for ETGs in the Porter+14 SAM for the σ -IMF mode with the observed Spiniello et al. (2014) +0.15 as input σ - x relation. The binned model data is shown in yellow and the observational data from Spiniello et al. (2014) in red. The σ - x model with Spiniello + 0.15 is thus able to reproduce both the offset and steepness of the ETGs at $z = 0$ well within the errorbars of the observational data, although a slightly steeper slope would fit the mean IMF slope in the highest mass bins from the observations even better.

The green line in Figure 4.14 is the Spiniello + 0.15 input relation and as before this input relation serves as an upper limit to the slope of the galaxies. The red line is the observed Spiniello et al. (2014) relation and fits the slope and offset of the model galaxies nicely, which can also be seen in the binned Figure 4.15. The σ - x model with Spiniello + 0.15 is thus able to reproduce both the offset and steepness of the ETGs at $z = 0$ well within the errorbars of the observational data, although a slightly steeper slope would fit the mean IMF slope in the highest mass bins from the observations even better. Figure 4.16 compares the results of the model with Spiniello and Spiniello +0.15 as input relations with the observed σ - x relation. Though both models fall within the errorbars of the observed relation, the model with Spiniello + 0.15 as input relation lies closest to the mean of the observed relation. In future works, however, it should be investigated how much the slope, and not just the offset, of the input σ - x relation should be adjusted to reproduce the slope of the observed relation fully.

4.2.2.3 The σ - x Relation at $z = 1$ and $z = 0$

The σ -IMF model with an input σ - x relation that is higher than the observed relation for local ETGs is able to reproduce the observations as we expect that the model galaxies in the SAM formed most of their stars earlier in galaxies with a lower σ and grew from there to end up as high-mass ETGs. We investigate the proposed evolution of the σ - x relation in the SAM from $z = 1$ to $z = 0$ to investigate the evolution of the PDMF slope with time and to see whether we can make predictions for future observations of the IMF of ETGs at higher redshifts

The Bolshoi DM tree files are generated to end at $z = 0$, but we can output the PDMF and typical galaxy properties for the central galaxies in the SAM at the intermediate step at $z = 1$ in a separate output file, galpropz.dat. We output the galaxies at $z = 1$ for a run of the SAM with the Spiniello relation and a run with the Spiniello + 0.15 as input σ - x relation. At $z = 1$, we do not have the information for the star formation rate averaged over the entire timescale of

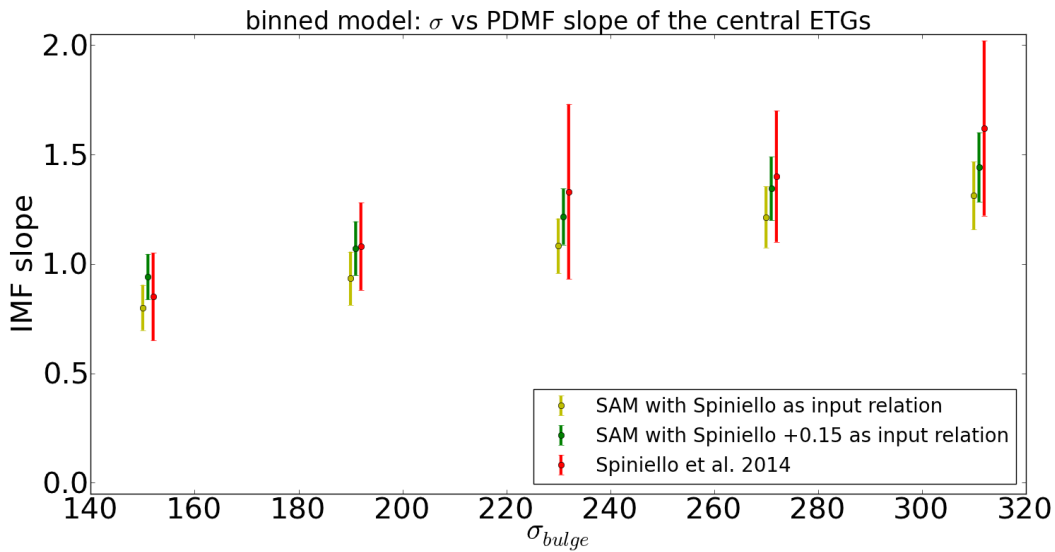


FIGURE 4.16: The binned σ -IMF slope relation for ETGs in the Porter+14 SAM for the σ -IMF mode with the Spiniello et al. (2014) as input σ - x relation (yellow) and with the Spiniello et al. (2014) +0.15 as input σ - x relation (green), to be compared with the observed σ -IMF slope relation (red). The PDMF slope of both models fall within the errorbars of the observed relation but the model with Spiniello + 0.15 as input relation is able to reproduce both the offset and steepness best. Although a slightly steeper slope would fit the mean of the IMF slope in the highest mass bins from the observations even better

the galaxy so we select our ETGs as in the rest of the σ -IMF model but without the condition $SFR < 0.3 M_{\odot}/yr$. These results are not colour coded by the mass weighted mean age of the galaxy as we also do not have that information at the intermediate output time at $z = 1$. The results for the Spiniello relation as input σ - x relation are given in Figures 4.17 and 4.18. The results for the Spiniello +0.15 as input relation are given in Figures 4.19 and 4.20.

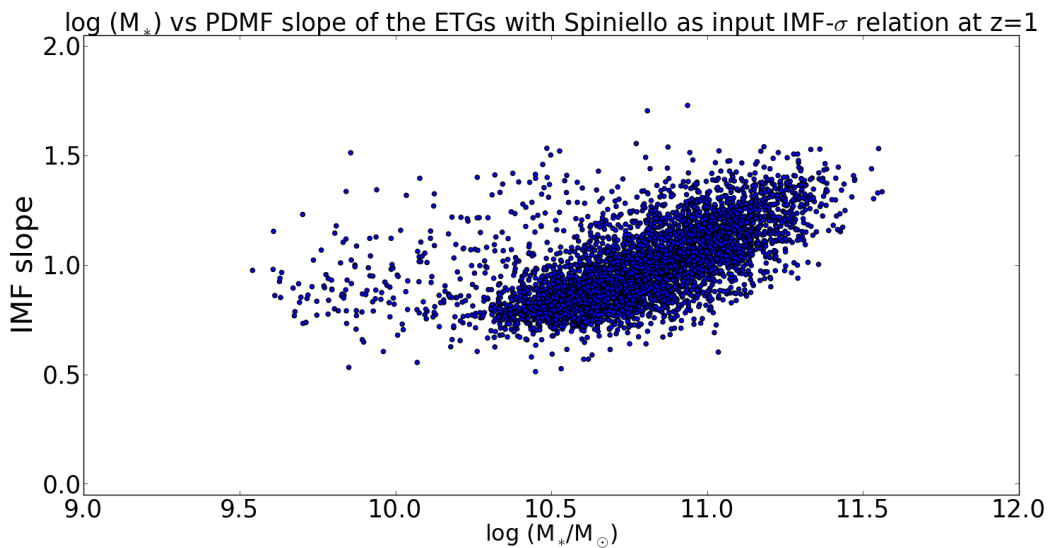


FIGURE 4.17: The M_* -IMF slope relation for ETGs at $z = 1$ in the Porter+14 SAM for the σ -IMF model with the observed Spiniello et al. (2014) as input σ - x relation.

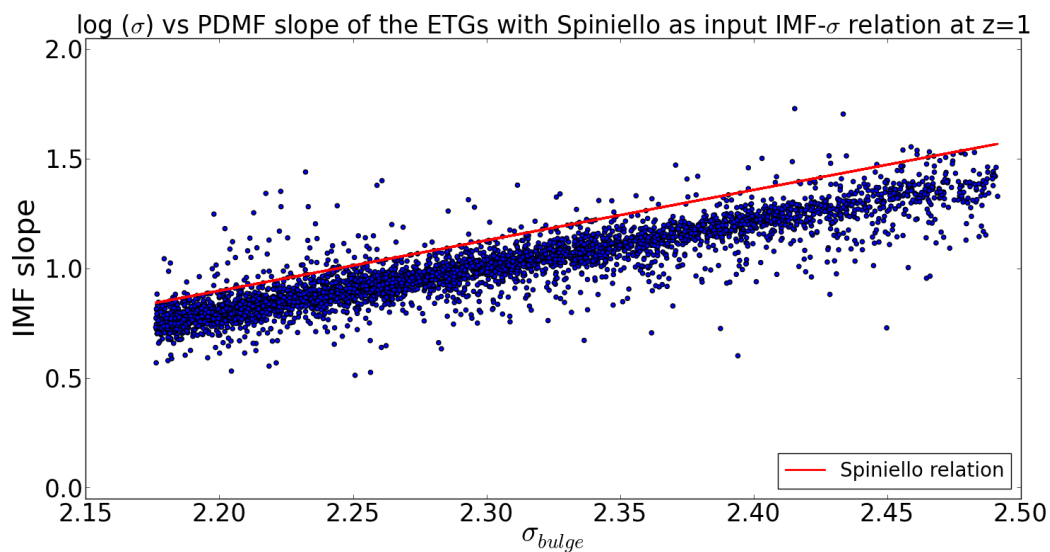


FIGURE 4.18: The σ -IMF slope relation for ETGs at $z = 1$ in the Porter+14 SAM for the σ -IMF model with the observed Spiniello et al. (2014) as input σ - x relation (green line), to be compared with the Spiniello et al. (2014) relation (red line).

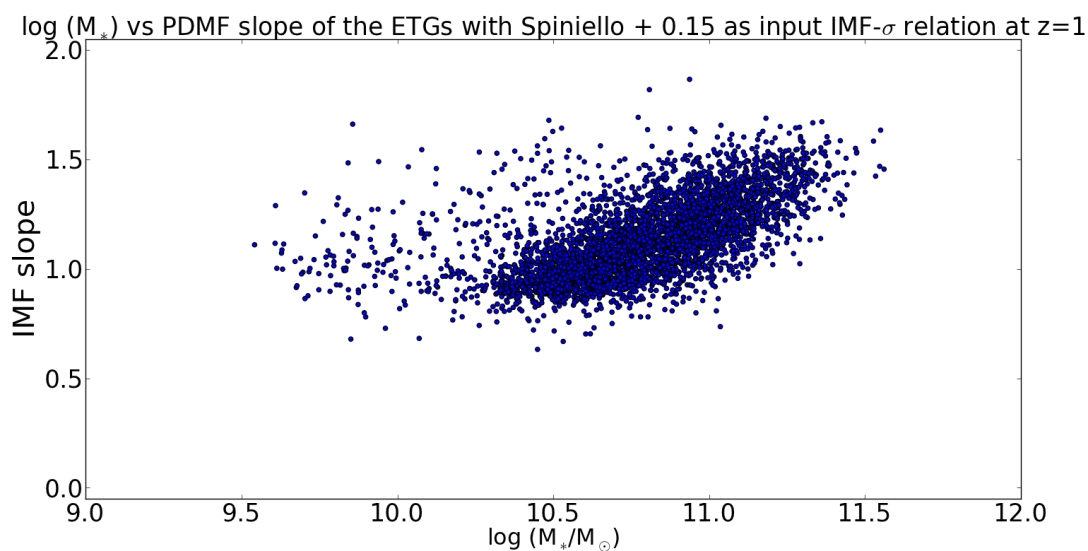


FIGURE 4.19: The M_* -IMF slope relation for ETGs at $z = 1$ in the Porter+14 SAM for the σ -IMF model with the observed Spiniello et al. (2014) +0.15 as input σ - x relation.

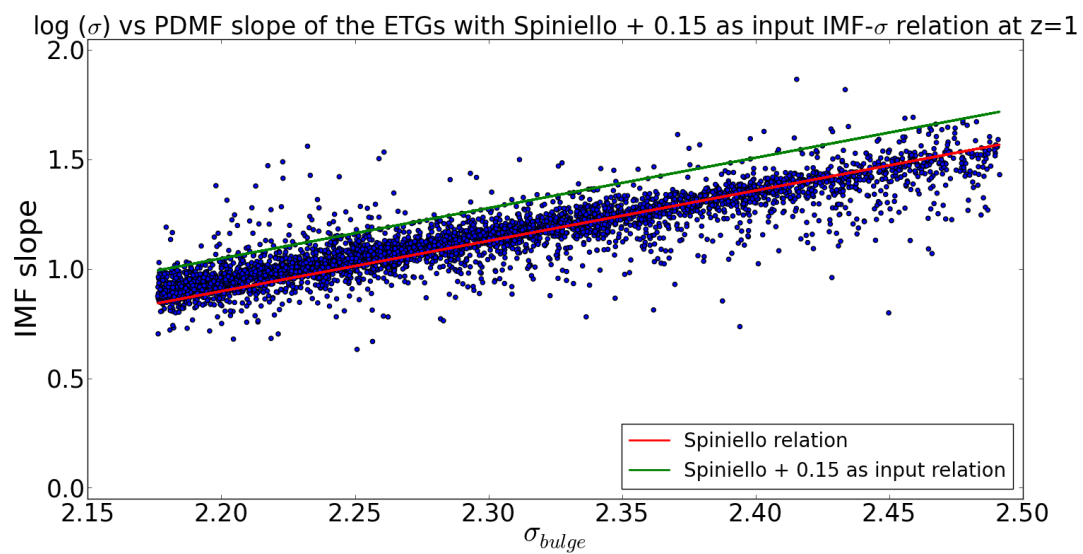


FIGURE 4.20: the σ -IMF slope relation for ETGs at $z = 1$ in the Porter+14 SAM for the σ -IMF model with the observed Spiniello et al. (2014) as input σ - x relation (red line).

We apply the same filtering, so without the condition $SFR < 0.3 M_{\odot}/yr$, to the central galaxies at $z = 0$ for the model with the Spiniello relation and the Spiniello + 0.15 as input σ - x relation. This allows us to fairly compare the binned results of the σ -IMF model at $z = 0$ and $z = 1$. For the Spiniello relation as input σ - x relation this is done in Figure 4.21 and for the Spiniello +0.15 as input relation in Figure 4.22.

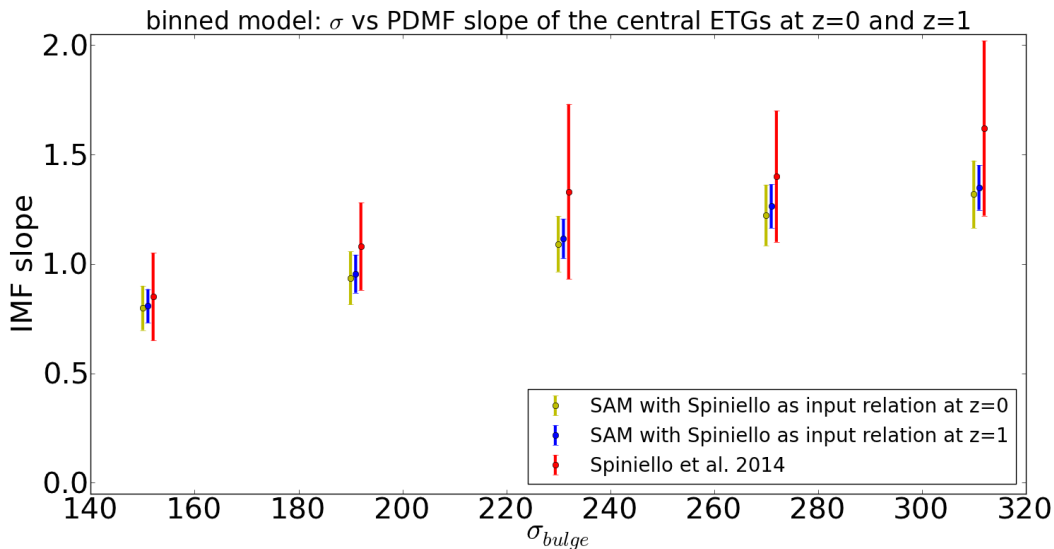


FIGURE 4.21: The σ -IMF slope relation for ETGs at $z = 0$ (yellow) and $z = 1$ (blue) in the Porter+14 SAM for the σ -IMF model with the observed Spiniello et al. (2014) as input σ - x relation. The binned σ -IMF slope from Spiniello et al. (2014) is shown in red. There is no significant evolution in the IMF slope of ETGs in this model between $z = 1$ and $z = 0$. At $z = 1$ there is a slightly smaller spread in possible IMF slopes as there are multiple formation paths that would lead to a particular σ galaxy between $z = 1$ and $z = 0$.

The low-mass PDMF slope of the galaxies at $z = 1$ lies slightly above the slope at $z = 0$ for either input σ - x relation. These galaxies at $z = 1$ must thus have merged with low σ galaxies, in which the stars had been formed at this low σ and thus with a lower slope, between $z = 1$ and $z = 0$ to decrease the slope. Moreover, at $z = 1$ there is a slightly smaller spread in possible slopes as there are multiple formation paths that would lead to a particular σ galaxy between $z = 1$ and $z = 0$.

4.3 Conclusion and Discussion

Using the observed Spiniello et al. (2014) σ -IMF slope relation we re-assign in post-processing an IMF slope to a set of formed stars to the σ of the galaxy in which they formed in the $\langle t \rangle$ -IMF model. This is done for the stars formed between 195 different ages from 0 – 13.75 Gyrs. The slope is connected to these ages by combining the Spiniello et al. (2014) relation and the mean age of each ETG at $x = 0$ we retrieve from the SAM. This method is only able to reproduce the observed relation in the highest σ bin and in the intermediate σ bins when the input $\langle t \rangle$ - x relation is a fit to the upper standard deviation of this relation rather than the mean. In the lower σ bins, however, the final PDMF slope for either of these models is higher than the observed relation.

Next, we apply the observed Spiniello et al. (2014) σ -IMF slope relation within the SAM each time stars are formed. We re-assigned the IMF slope following this relation based on the

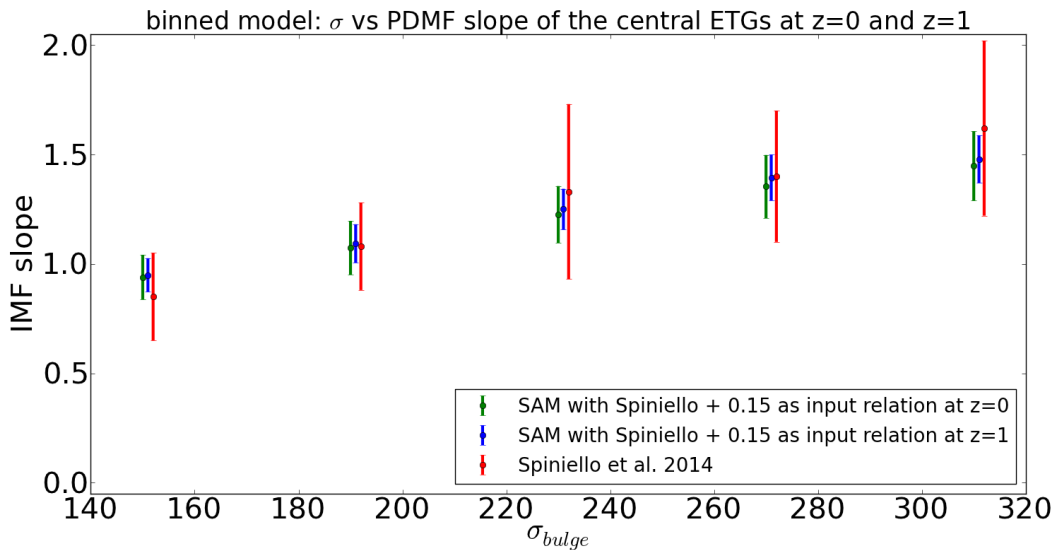


FIGURE 4.22: The σ -IMF slope relation for ETGs at $z = 0$ (green) and $z = 1$ (blue) in the Porter+14 SAM for the σ -IMF model with the observed Spiniello et al. (2014)+0.15 as input σ - x relation. The binned σ -IMF slope from Spiniello et al. (2014) is shown in red. There is no significant evolution in the IMF slope of ETGs in this model between $z = 1$ and $z = 0$. These results for redshift evolution are the same as when Spiniello et al. (2014) is used as input σ - x relation (in Figure 4.21, but the offset of the slope at both $z = 1$ and $z = 0$ is moved upward and better fits the mean of the observed relation as is shown in Figure 4.16).

σ of the galaxy in which the stars are formed using this relation and the PDMF for each galaxy is populated additively. This σ -IMF model is able to reproduce the slope of the observed σ -IMF relation over the entire considered σ range better than if we assign it in post-processing. However, the input σ -IMF slope relation serves as an upper limit of the slope as most of the stars of a particular galaxy were not formed when that galaxy had reached its present day size. By drawing a horizontal line at a fixed IMF slope between the input relation and the model points, we can see at which sigma most of the stars contributing to this slope formed. To retrieve the observed relation the offset of the input relation needs to be shifted by 0.15. Applying the σ -IMF model with Spiniello + 0.15 as input relation in the SAM is thus able to reproduce both the offset and steepness of the ETGs at $z = 0$.

To fully test this σ -IMF model the next step will be to assign the change in IMF slope to a set of stars corresponding to the σ of the galaxy self-consistently within the SAM. In our current model we merely ascribe an IMF slope to the stars formed and populate the low-mass PDMF of the galaxy accordingly. However, the chemical enrichment and subsequent cooling and heating and stellar feedback of the stars formed remain those prescribed following a Chabrier IMF. These processes should depend on the power-law slope each time stars are formed to fully investigate the implications of the σ -IMF model in the SAM. However, as we in our current models only re-assign the low-mass IMF, this could be considered as applying a two-fold IMF with a varying low-mass part and a fixed high-mass slope. Implementing such a two-fold model self-consistently in the SAM will not affect the SN feedback from high mass stars and keep the overall normalisation the same (Fontanot et al. 2009).

Moreover, we investigate the evolution of the σ - x relation in the SAM from $z = 1$ to $z = 0$ and find that there is no significant evolution in the IMF slope of ETGs in the SAM to $z = 1$.

This is in agreement with observations by Martín-Navarro et al. (2014) who determined the

IMF of 49 massive quiescent galaxies between $0.9 < z < 1.5$ using the TiO2 absorption feature which has a dependence on stellar age and on the content of the low mass stars. They fit the IMF using a bimodal IMF from Vazdekis and Beckman (1996) which is flattened for stellar masses below $M < 0.6M_{\odot}$ and is further solely defined by a single parameter Γ_b . They find that at $z \sim 1$ the IMF is more bottom heavy, $\Gamma_b = 3.2 \pm 0.2$ for the most massive galaxies $M > 10^{11}$ than the $\Gamma_b = 2.7^{+0.3}_{-0.4}$ for the lighter galaxies $2 \times 10^{10} < M < 10^{11}M_{\odot}$. After converting the stellar mass to velocity dispersion they find that these slopes at $z = 1$ are only slightly higher than the observed bimodal slope in ETGS of Ferreras et al. (2013) at $z = 0$. They thus do not find any evolution in IMF slope since $z = 1$. However, as the Ferreras et al. (2013) σ -IMF slope relation is steeper than Spiniello et al. (2014) we compare our results to, the slope of Martín-Navarro et al. (2014) $z = 1$ lies a couple of tenths in slope above the observed Spiniello et al. (2014) at $z = 0$.

We thus predict no evolution for IMF slope for the most massive galaxies after $z \sim 1$. This makes sense as the most massive galaxies have finished forming most of their stars before $z = 1$ (Panter and Charlot 2007). In future works it should be investigated from which z onward the models would predict a discernible evolution in IMF slope and for which lower galaxy masses the model does predict some evolution in slope between $z = 1$ and $z = 0$. This information could be used to guide and compare to future observations of IMF at higher z or in less massive galaxies.

As explained in more detail in Section 1.1.2, a relation between $[\text{Mg}/\text{Fe}]$ and IMF slope has been proposed as a driver for IMF variations (Conroy and van Dokkum 2012a; van Dokkum and Conroy 2010), besides velocity dispersion (Ferreras et al. 2013; LaBarbera et al. 2013; Spiniello et al. 2014). Martín-Navarro et al. (2015) studied the stellar population and kinematic properties of 24 local ETGA from the CALIFA survey to determine whether σ or metallicity is the driver for the IMF observed low-mass IMF variations in ETGs. They again assumed a bimodal IMF truncated below $0.6M_{\odot}$ and fit the slope above $0.6M_{\odot}$ with Γ_b , the only free parameter. They do not find a tight correlation between $[\text{Mg}/\text{Fe}]$, age or V_r but do find a strong correlation between IMF slope- $[M/H]$. They find that with increasing metallicity the slope increases, so becomes more bottom heavy. They postulate that this metallicity-IMF slope relation drives IMF variations and that the observed σ -IMF slope relation is a result of the combination of the galaxy mass-metallicity relation and this metallicity-IMF slope relation. If this is indeed the case, it will also have an influence on the evolution of galaxies and their IMF relation (Martín-Navarro et al. 2015). Massive galaxies increase their metallicity during the formation of different stellar populations due to stellar feedback and chemical enrichment. Following the proposed metallicity-IMF slope relation the IMF should have been shallower at higher redshifts above $z \sim 1$.

If the underlying metallicity-IMF relation indeed drives IMF variations, it is possible that the success of our σ -IMF model in the SAM is actually due to this underlying metallicity-IMF slope relation. In this model, we re-assign an IMF slope to galaxies in the SAM based on the σ of the galaxy in which the stars formed and the metallicity-mass relation could connect the metallicity-IMF slope relation to the σ of the galaxy. To fully test the σ -IMF model in the SAM we will need to implement it self consistently such that each time stars are formed the assigned IMF slope is also used in prescribing the heating, cooling and chemistry following from that formed stellar population. In our current SAM, all those quantities are modeled based on a Chabrier IMF. When a varying IMF is implemented self-consistently such that it can model the subsequent evolution of the chemical enrichment, it can be used to connect the IMF slope to the metallicity of the gas out of which the stars formed. Such an implementation can test

whether this, underlying, metallicity relation is able to reproduce the observed σ -IMF slope relation in the SAM.

Conclusion

The stellar IMF is an observationally derived relation that describes the mass distribution of stars formed in a single stellar population; it describes the ratio of high to low-mass stars. Understanding the IMF is important for observing and interpreting observations of galaxies as high-mass stars are responsible for most of the chemical enrichment and stellar feedback and will dominate the light of a galaxy whereas the low-mass stars dominate the galaxy's total stellar mass.

Due to observational limitations, most observational studies of the IMF have been performed on stellar populations in the Milky Way and in the Local Group. These observations indicate that the IMF is the same in all these environments and can be described by a power-law in the high-mass end with a log-normal turn over and an exponential cut-off below $1 M_{\odot}$. In SSP and other models, it has been assumed that this type of IMF is universal over cosmic time and galactic environment. However, recent studies using a combination of lensing, stellar dynamics, spectral features and SSP indicate that the low-mass IMF varies with galaxy properties such as velocity dispersion (Auger et al. 2010; Conroy and van Dokkum 2012a,b; Ferreras et al. 2013; LaBarbera et al. 2013; Spiniello et al. 2014, 2012; Treu et al. 2010; van Dokkum and Conroy 2010). ETGs with high velocity dispersion in the local Universe appear to have relatively more low-mass stars than predicted by a universal IMF.

The physical origin for this bottom-heavy IMF is unclear but theories based on increased low-mass fragmentation due to turbulence provide promising results. These theoretical and computational models derive the CMF and by extension the IMF from turbulence in molecular clouds all predict a Salpeter-like powerlaw slope at high core masses and a log-normal turnover (Hennebelle and Chabrier 2008, 2009; Hopkins 2012a,b, 2013; Padoan and Jones 1997; Padoan and Nordlund 2002). In all three models, the location of this turnover depends on the scale below which thermal and/or magnetic support becomes greater than that of turbulence. A larger Mach number thus allows for fragmentation to smaller scales, creating a more bottom-heavy IMF.

However, these theories of the CMF/IMF formation and variation in itself do not yet provide an explanation of the difference in conditions in galaxies that appears to lead to a more bottom-heavy IMF in ETGs than in our own Milky Way. Merger-induced star formation and starbursts could provide such turbulent conditions out of which a bottom-heavy IMF can form as these lead to high local temperatures, but also high densities and velocity dispersion. Such

a dependence on star formation history and environment could link the theories on the origin of a bottom-heavy IMF to the observations of the bottom-heavy IMF in ETGs.

We use the PST14 and Porter+14 model of the “Santa Cruz” SAM to test the variation of the IMF with typical galaxy properties, such as fraction of starburst, total stellar mass, and morphology, that could possibly influence the mass distribution of stars. SAMs tie physically motivated recipes for the baryonic processes that govern galaxy formation and evolution to DM halo merger trees. They can provide global properties of galaxies for a large number of galaxies in a computer-time efficient manner and are therefore ideal to study variations of the IMF with galaxy- and star formation environment. SAMs also allows us to track under what conditions or in what location stars formed. We used this to test several recipes of re-assigning a bottom-heavy IMF to stars formed under certain conditions in the SAM and compared the resulting PDMF slope with the observed Spiniello et al. (2014) IMF-slope to gain insight into the underlying physical reasons of the observed variation in the low-mass end of the IMF in ETGs.

We tested four different models of re-assigning an IMF to stars formed in the SAM and compared to resulting PDMF – galaxy mass or σ relation to the observed Spiniello et al. (2014) relation to disentangle drivers of low-mass IMF variation in ETGs. We will recap the results of these models and their implications for postulated physical drivers of a bottom-heavy IMF:

- The physically motivated **SF-IMF model**, which ties a Chabrier shape to stars formed quiescently and a Salpeter shape to stars formed in bursts and under the assumption that stars formed in bursts formed under more turbulent conditions. This model is implement as theories of IMF formation suggest that turbulent conditions can lead to a more bottom-heavy IMF. This SF-IMF model is unable to reproduce the observed low-mass PDMF slope of the most massive ETGs as the majority of their stars did not form in bursts. If turbulence drives the increased low-mass fragmentation molecular clouds, this model shows that only taking turbulence associated with starburst star formation, whether merger- or disc instability induced, into account is not sufficient to reproduce the observed bottom-heavy IMF in ETGs.
- The **Morph-IMF model**, which ties the shape of the IMF to the present-day location of stars, either a Chabrier slope to stars in the disc or a Salpeter slope to stars in the bulge. In the high-mass end this method is able to reproduce the observed σ -IMF relation in local ETGs within the error bars of the observational data, though not the low-mass galaxy end. The present day location of the stars, in either the disc or spheroid, thus has a larger effect on the steepness of the final PDMF slope than the manner in which these stars formed, either in bursts or quiescently. This is because by selection of ETGs in the model, these are the galaxies with high bulge-to-total stellar masses (i.e. $B/T > 0.5$). The present-day location of the stars is not necessarily the location where the stars formed as they could have migrated from the disc to the bulge in the SAM, however, it can be seen as an indirect tracer of the formation history of the galaxy. It indirectly traces the time of the majority of the star formation as the present-day bulge stars most likely formed in discs at higher redshift and moved to the spheroid after a merger or a disk instability to eventually form a current ETG. The partial success of this Morph-IMF model could thus be due to the scaling of turbulence with cosmic time, where gas conditions out of which stars in discs formed had a higher density and were more turbulent at earlier times.
- The **$\langle t \rangle$ -IMF model**, which assigns a single power-law IMF slope to a set of stars formed that varies with the time at which they formed in post-processing. This power-law slope

varies with $\langle t \rangle$ following the σ - $\langle t \rangle$ relation which can be determined from the output of the SAM and the observed σ -IMF slope in ETGs. This model re-assigns an increased dwarf-to-giant ratio in a stellar population through an increase in a single low-mass power-law slope instead of using a Chabrier and a Salpeter IMF for different conditions. This model can reproduce the observed relation in the intermediate and high σ bins but over predicts the relative number of low-mass stars formed in the lower bins. These high σ galaxies have the oldest mean age and thus are expected to have most of their stars formed in high-redshift turbulent gas. However, by construction, the $\langle t \rangle$ -IMF model in post-processing is not able to apply a varying IMF slope over the entire age history of the galaxies in the SAM; the selected ETGs that were used to relate $\langle t \rangle$ to σ and then to the power-law slope by nature all have a relatively high mean age that does not cover the entire possible age spectrum and all time steps. We chose to truncate the power-law slope below the lowest mean age in the sample. As the lower mass ETGs have more of their stars formed below this mean age than the highest mass ones, the PDMF slope in the low-mass galaxies is over predicted due to the model construction whereas the high-mass end is not significantly affected by this model choice.

- The σ -IMF model, which assigns a single power-law IMF slope to a set of stars formed that varies with the σ of the galaxy in which they formed. This is implemented within the Porter+14 SAM such that for each galaxy the PDMF is re-populated additively based on this σ -x relation each time stars are formed. The σ -IMF model is able to reproduce the slope of the observed σ -IMF relation over the entire considered σ range better than the $\langle t \rangle$ -IMF model in post-processing. However, the input σ -IMF slope relation serves as an upper limit of the slope as most of the stars of a particular galaxy were not formed when that galaxy had reached its present day size. By drawing a horizontal line at a fixed IMF slope between the input relation and the model points, we can see at which sigma most of the stars contributing to this slope formed. To retrieve the observed steepness and offset of the Spiniello et al. (2014) relation of ETGs at $z = 0$, the offset of the input relation needs to be shifted upwards by ≈ 0.15 . throughout their lifetime, larger σ galaxies merges with multiple smaller galaxies, which have more bottom-light stellar population and thus brings their PDMF slope down. The input σ -x relation in the σ -IMF model thus needs to be higher than the the one observed in $z = 0$ galaxies to account for this accretion and still be able to reproduce the observed relation. The input power-law slope thus has to scale with the σ of a galaxy at time most of the galaxy's stars formed. This input power-law slope needs to be higher than present-day observed relation to reproduce observations. If increased turbulence indeeds decreases fragmentation scales to lower masses, this method takes into account a decrease in turbulence in overall gas conditions in discs over time.

5.0.1 Future Prospects

We investigate for the σ -IMF Model the evolution of the σ -x relation in the SAM from $z = 1$ to $z = 0$ and find that there is no significant evolution in the IMF slope of ETGs in the SAM to $z = 1$ in agreement with observational results from Martín-Navarro et al. (2014). This result makes sense as the most massive galaxies have finished forming most of their stars before $z = 1$ (Panter and Charlot 2007). We expect this evolution of σ -x relation to occur at higher redshift. In future works it should be investigated from which z onward the models would predict a discernible evolution in IMF slope and for which lower galaxy masses the model does predict some evolution in slope between $z = 1$ and $z = 0$. This information could be used to guide and compare to future observations of IMF at higher z or in less massive galaxies. Especially the coming generation of extremely large telescopes with apertures of > 30 m, i.e.

the European Extremely Large Telescope (E-ELT) and Thirty Meter Telescope (TMT), will be sensitive enough and have a large enough range up to the Near Infra Red (NIR) to pick up lines indicative of low-mass stars such as TiO2 at high redshifts out to $z \approx 3$.

Martín-Navarro et al. (2015) find a strong correlation between IMF slope– $[M/H]$. They find that with increasing metallicity the IMF slope increases, so becomes more bottom heavy. They postulate that the metallicity–IMF slope relation drives IMF variations and that the observed σ –IMF slope relation is a result of the combination of the galaxy mass–metallicity relation and this metallicity–IMF slope relation. Following the proposed metallicity–IMF slope relation the IMF should have been shallower at higher redshifts above $z \sim 1$. When a varying IMF is implemented self-consistently in the SAM, it can model the evolution of the chemical enrichment when the IMF slope is connected to the metallicity of the gas out of which the stars formed. Such an implementation can determine whether this relation can reproduce the observed σ – x relation in the SAM and thus be considered the underlying driver. The evolution of the IMF slope with redshift could be used to disentangle whether σ or metallicity is a driver of IMF variations.

However, the implementation of the σ –IMF model within SAM is not yet self-consistent; we only re-assign a power-law IMF slope to the stellar population after the stars have formed such that e.g. SN fractions, metallicities and photometry are all still calibrated based on a Chabrier IMF. As we only re-assign the low-mass IMF, this could be considered as applying a two-fold IMF with a varying low-mass part and a fixed high-mass slope. If this fixed high-mass slope is similar to the one in a Chabrier IMF, this should not significantly affect gas and metallicity injection from, short-lived, high-mass stars. The different theories of the low-mass IMF/CMF variation predict not a power-law but a log-normal turn over with an exponential cut-off of the IMF in the low-mass end. The peak of this turn-over mass is shifted towards smaller masses and shifted upwards with increasing turbulence when turbulence will dominate over thermal support up until smaller fragmentation scales. This creates more mass in smaller stars, such that a power-law fit to this slope will steepen. However, due to the turn-over, the amount of mass in the smallest stars will be over-estimated by such a power-law. A re-assignment of a low-mass IMF with different peak masses varying with, for instance, σ should thus be implemented to correctly model the formation of the low-mass PDMF at the smallest stellar scales. The line indices from the SED model in the SAM taking into account the varying IMF slope could be applied in SSP models to compare to line indices of actual observed galaxies to compare metallicity evolution and star formation histories in the model galaxies and the observed galaxies to further narrow down the physical driving mechanisms for a bottom-heavy low-mass IMF in ETGs.

Moreover, in future recipes it should be investigated how assigning an IMF slope self-consistently based on properties associated more directly with the star-formation process in the SAM influences the final PDMF slope. One quantity that would be ideal for this purpose is the gas surface density as it is related to star formation via the Kennicutt-Schmidt law and we know that it evolves with cosmic time and contributes to setting turbulent conditions and thus possibly fragmentation scales. In our σ –IMF model we assigned an input σ –IMF slope relation based on an empirical relation from Spiniello et al. (2014) to test what is needed to shape that observational relation in the SAM. This method does not yet directly point out the underlying physical process that causes the molecular clouds in galaxies to fragment and form stars following a certain mass distribution. In this project we have shown that we can model and investigate the low-mass IMF variation with global galaxy properties using a SAM. However, assigning an IMF slope based on more directly star formation related properties such as gas surface density could help to reach a better understanding of the star formation environment

and evolution thereof in galaxies that could lead to the relatively bottom-light IMF observed in the Milky Way and the bottom-heavy IMF observed in ETGs.

Acknowledgements

First of all, I would like to sincerely thank my supervisors Scott Trager and Gergö Popping for all of their support, feedback, useful discussions and for always answering all of my questions. Scott, I wanted to let you know how much I truly appreciated your patience and understanding over the course of this project and also for teaching me so much about doing academic research in general. This thesis would not have its current form without it and I hope to take all that I have learned with me to new studies and projects. Gergö, thank you for familiarizing me with the SAM and still answering my questions about the model and the results all the way from Munich, I've really grown to like (and hopefully understand) the SAM thanks to your help. To everyone whose been in our group over the years, I enjoyed the weekly motivator and interesting article discussions and am especially thankful for the helpful suggestions from everyone in these last couple of months of the project. I am grateful to Marco Spaans for willing to be the second reader of this thesis. I would also like to thank Rachel Somerville for helping me with some details of the SAM when no one else could and for her interest in this project.

To all of the teachers, secretaries, computer group and everyone else at the Kapteyn Institute, I am grateful for all that you have taught me and for creating such a warm place to work and study, I will miss it. Marlies, thank you for introducing me to the planetarium; teaching at schools always helped remind me why I loved astronomy and chose to study it in the first place. I'd especially like to thank everyone in the large student room (the number of which I still don't know by heart) over the years for the 'gezellige' atmosphere. Jorien, thank you for your support and kindness, I will miss our tea breaks and delicious cake baking but luckily we'll be living in the same country next year!

I'm also grateful to all my friends who pulled me away from my computer every once in a while. Melanie en Laura in het bijzonder, bedankt voor alle afleiding met goed eten, spelletjes en reizen, maar ook jullie gezelschap en steun toen ik die nodig had! Op naar jaren vol nieuwe reizen en meer tijd voor spelletjes avonden. Tot slot wil ik mijn moeder, Thijs, oma, Ineke en de rest van mijn familie bedanken voor hun interesse in mijn studie, en hun vertrouwen en warmte. Mama, bedankt voor het laatste steuntje in de rug toen ik het nodig had, maar voornamelijk bedankt dat je er altijd voor me bent geweest!

Bibliography

- Alves, J. et al. *AA*, 462:L17, 2007.
- Arrigoni, M., Trager, S. C., Somerville, R. S., and Gibson, B. K. *MNRAS*, 402:173, 2010.
- Auger, M.W. et al. *ApJ*, 721:L163, 2010.
- Bastian, Covey K. R.,N. and Meyer, M. R. *ARAA*, 48:339, 2010.
- Baugh, C.M. *Rept.Prog.Phys.*, 69:3101, 2006.
- Behroozi, P. S., Wechsler, R. H., Wu, H.-Y., Busha, M. T., and Klypin, A. A. *ApJ*, 763:18, 2014.
- Benson, A.J. *Physics Reports*, 495:33, 2010.
- Blumenthal, G.R. et al. *Nature*, 311:517, 1984.
- Bond, J. et al. *ApJ*, 379:440, 1991.
- Bondi, H. *MNRAS*, 112:195, 1952.
- Bournaud, F. et al. *ApJ*, 730:4, 2011.
- Bower, R.G. et al. *MNRAS*, 370:645, 2006.
- Brennan, R. et al. *MNRAS*, 451:2933, 2015.
- Bruzual, G. and Charlot, S. *MNRAS*, 344:1000, 2003.
- Cappellari, M. et al. *Nature*, 484:485, 2012.
- Chabrier, H. *PASP*, 115:763, 2003.
- Cheng, J.Y. et al. *MNRAS*, 412s:727, 2011.
- Cole, S. *ApJ*, 367:45, 1991.
- Cole, S. et al. *MNRAS*, 271:781, 1994.
- Cole, S. et al. *MNRAS*, 319:168, 2000.
- Conroy, C. and van Dokkum, P. *ApJ*, 747:69, 2012a.
- Conroy, C. and van Dokkum, P. *ApJ*, 760:71, 2012b.

- Covington, M., Dekel, A., Cox, T. J., Jonsson, P., and Primack, J. R. *MNRAS*, 384:94, 2008.
- Covington, M. D. et al. *MNRAS*, 415:1029, 2011.
- Crosby, B.D. et al. *ApJ*, 773:108, 2013.
- Croton, D. J. et al. *MNRAS*, 365:11, 2006.
- Debattista, V. P., Carollo, C. M., Mayer, L., and Moore, B. *ApJL*, 604:L93, 2004.
- Dekel, A. et al. *Nature*, 457:451, 2009.
- Dekel, A. et al. *MNRAS*, 435:999, 2013.
- Dutton, A. A. et al. *MNRAS*, 428:3183, 2013.
- Efstathiou, G., Lake, G., and Negroponte, J. *MNRAS*, 199:1069, 1982.
- Faber, S.M and Jackson, R.E. *ApJ*, 204:668, 1976.
- Ferreras, I. et al. *MNRAS*, 429:L15, 2013.
- Fontanot, F. *MNRAS*, 442:3138, 2014.
- Fontanot, F., De Lucia, G., Monaco, P., Somerville, R. S., and Santini, P. *MNRAS*, 397:1776, 2009.
- Gadotti, D.A. *MNRAS*, 393:1531, 2009.
- Gnedin, N. Y. *ApJ*, 542:535, 2000.
- Graham, A.W. and Worley, C.C. *MNRAS*, 388:1708, 2008.
- Guo, Q., White, S., Li, C., and Boylan-Kolchin, M. *MNRAS*, 404:1111, 2010.
- Guo, Q. et al. *MNRAS*, 413:101, 2011.
- Hennebelle, P. and Chabrier, G. *ApJ*, 684:385, 2008.
- Hennebelle, P. and Chabrier, G. *ApJ*, 702:1428, 2009.
- Hennebelle, P. et al. *A&A*, 446:43, 2008.
- Henriques, B. M. B. et al. *MNRAS*, 3373:431, 2013.
- Hirschmann, M., Somerville, R. S., Naab, T., and Burkert, A. *MNRAS*, 426:237, 2012.
- Hopkins, P. F., Cox, T. J., Younger, J. D., and Hernquist, L. *ApJ*, 691:1168, 2009a.
- Hopkins, P. F., Hernquist, L., Cox, T. J., Keres, D., and Wuyts, S. *ApJ*, 691:1424, 2009b.
- Hopkins, P. F. et al. *MNRAS*, 397:802, 2009c.
- Hopkins, P.E. *MNRAS*, 423:2016, 2012a.
- Hopkins, P.E. *MNRAS*, 423:2037, 2012b.
- Hopkins, P.E. *MNRAS*, 170:433, 2013.
- Johansson, P. H., Naab, T., and Burkert, A. *ApJ*, 690:802, 2009.

- Kauffman, G., White, S., and Guiderdoni, B. *MNRAS*, 264:201, 1993.
- Kennicutt, R. C. *ApJ*, 498:181, 1998.
- Klypin, A. A., Trujillo-Gomez, S., and Primack, J. *ApJ*, 740:102, 2011.
- Komatsu, E. et al. *ApJS*, 180:330, 2009.
- Kritsuk, A. G. et al. *ApA*, 665:416, 2007.
- Kroupa, P. *Science*, 295:82, 2002.
- Kroupa, Tout C. A.,P. and Gilmore, G. *MNRAS*, 262:545, 1993.
- LaBarbera, F. et al. *MNRAS*, 433:3017, 2013.
- Lacey, C. and Cole, S. *MNRAS*, 262:627, 1993.
- Leroy, A. K. et al. *AJ*, 136:2782, 2008.
- Longair, M. *Galaxy Formation*. Springer, 2 edition, 2008.
- MacLow, M.M. and Klessen, R. *Rev. Mod. Phys*, 76:125, 2004.
- Martín-Navarro, I. et al. *to appear in ApJL*, arXiv:1407.4455v2, 2014.
- Martín-Navarro, I. et al. *to appear in ApJL*, arXiv:1506.00638, 2015.
- McKee, C.F. and Ostriker, J.P. *ApJ*, 218:448, 2007.
- Mo, Mao S.,H. J. and White, S. D. M. *MNRAS*, 295:319, 1998.
- Nelan, J.E. et al. *ApJ*, 632:137, 2005.
- Offner, S. S. R. et al. The origin and universality of the stellar initial mass function. In Beuther, H. et al., editors, *Protostars and Planets VI*. University of Arizona Press, 2014.
- Ostriker, J. P. and Peebles, P. J. E. *ApJ*, 186:467, 1973.
- Padoan, Nordlund A.,P. and Jones, B. *MNRAS*, 288:145, 1997.
- Padoan, P. and Nordlund, A. *ApJ*, 526:279, 1999.
- Padoan, P. and Nordlund, A. *ApJ*, 576:870, 2002.
- Panter, Jimenez R. Heavens A. F.,B. and Charlot, S. *MNRAS*, 378:1550, 2007.
- Peebles, P. J. E. *ApJ*, 155:393, 1969.
- Popping, G., Somerville, R.S., and Trager, S.C. *MNRAS*, 442:2398, 2014.
- Porter, L.A. et al. *MNRAS*, 444:942, 2014a.
- Porter, L.A. et al. *MNRAS*, 445:3092, 2014b.
- Press, W. and Schechter, P. *ApJ*, 187:425, 1974.
- Robaina, A. R. et al. *ApJ*, 704:324, 2009.
- Salpeter, E. *ApJ*, 121:161, 1955.

- Schweizer, F. *ApJ*, 252:455, 1982.
- Shankar, F. et al. *MNRAS*, 428:109, 2013.
- Shen, S. et al. *MNRAS*, 343:978, 2003.
- Smith, R.J. *MNRAS*, 443:L69, 2014.
- Somerville, R. and Kolatt, T. How to plant a merger tree. *MNRAS*, 305:1–14, 1999.
- Somerville, R. and Primack, J. *MNRAS*, 310:1087–1110, 1999.
- Somerville, R. et al. *MNRAS*, 316:479, 2000.
- Somerville, R. et al. *MNRAS*, 391:481–506, 2008.
- Somerville, R. et al. *MNRAS*, 423:1992–2015, 2012.
- Spiniello, C., Trager, S. C., Koopmans, L. V. E., and Conroy, C. *MNRAS*, 438:1438, 2014.
- Spiniello, C. et al. *ApJL*, 753:L32, 2012.
- Springel, V., White, S. D. M., Tormen, G., and Kauffmann, G. *MNRAS*, 328:726, 2001.
- Sutherland, R. and Dopita, M.A. *ApJS*, 88:253, 1993.
- Toomre, A. *ApJ*, 139:1217, 1964.
- Toomre, A. and Toomre, J. *ApJ*, 178:623, 1972.
- Trager, S.C. and Somerville, R.S. *MNRAS*, 395:608, 2009.
- Treu, T. et al. *ApJ*, 709:1195, 2010.
- Troland, T. and Heiles, C. *ApJ*, 301:339, 1986.
- Trujillo-Gomez, S., Klypin, A., Primack, J., and Romanowsky, A. J. *ApJ*, 16:742, 2011.
- van Dokkum, P. and Conroy, C. *Nature*, 468:940, 2010.
- Vazdekis, Casuso E. Peletier R. F.,A. and Beckman, J. E. *ApJS*, 106:307, 1996.
- Weinmann, S. M. et al. *MNRAS*, 426:2797, 2012.
- White, S. and Frenk, C. *ApJ*, 379:52, 1991.
- White, S. D. M and Rees, M. J. *MNRAS*, 379:341, 1978.
- White, Somerville R.S,C.E and Ferguson, H.C. *ApJ*, 799:201, 2015.
- Wilman, D.J. et al. *MNRAS*, 443:2986, 2013.
- Windhorst, R. W. et al. *ApJ*, 380:362, 1991.